Thesis for The Degree of Licentiate of Engineering

Design and Optimization of HF Transformers for High Power DC-DC Applications

Mohammadamin Bahmani

Division of Electric Power Engineering
Department of Energy and Environment
Chalmers University of Technology
Göteborg, Sweden, 2014

Design and Optimization of HF Transformers for High Power DC-DC Applications

Mohammadamin Bahmani

Division of Electric Power Engineering
Department of Energy and Environment
Chalmers University of Technology
Göteborg, Sweden

Printed by Chalmers Reproservice,
Göteborg, Sweden 2014.

To Aryan

Abstract

Increasing the operational frequency is the most common solution to achieve higher power densities, since the weight and volume of the magnetic part, the bulkiest element in power electronics converters, are then decreased. This solution is well established in low power high frequency applications, while in the recent decade, the possibility of utilizing high frequency at higher power and voltage levels has generated wide interest as well.

This work proposes a design and optimization methodology of a high power high frequency transformer accounting for the tuned leakage inductance of the transformer, as well as high isolation requirements, particularly in DC offshore application where a converter module should withstand the MVDC or HVDC link voltage. To achieve this goal, several models were proposed and developed in order to accurately characterize such a transformer. One of these models is a so called pseudo-empirical expression derived from a rigourous regression algorithm based on an extensive 2D finite element simulation scenario, resulting in an accurate analytical expression with an average unsigned deviation of 0.51% and the extreme deviations not higher than 9%. Moreover, using the energy method, an analytical expression to precisely calculate the leakage inductance of high power density magnetic components is proposed. In addition, using the proposed modification of the Steinmetz equation for core loss calculations, general expressions are derived and presented for a rectangular waveform with its associated duty cycle and rise time.

Applying the proposed design methodology, in which all the aforementioned models are implemented on a 1 MW case study transformer, indicates that such a transformer can achieve a power density of about 22 kW/L and the efficiencies as high as 99.74%. Moreover, with respect to the isolation requirements, desired leakage inductance and the magnetic material used, a critical operating frequency can be found above which the transformer does not benefit from volume reduction anymore.

Keywords

High Power High Frequency Transformer, Isolation Requirements, Leakage Inductance.

Acknowledgment

This project has been funded by the Swedish Energy Agency. A great thank goes to them for the financial support.

I would like to express my sincere gratitude to my supervisor and examiner Prof. Torbjörn Thiringer for his great support especially at the most desperate moments. His patience, guidance and emphasis on educating a researcher are extremely appreciated. Thank you! I would also like to thank my previous roommate and current supervisor Dr. Tarik Abdulahovic for his friendship and continuous support.

My acknowledgments go to the members of the reference group Dr. Philip Kjaer form Vestas, Dr. Anders Holm from Vattenfall, Dr. Aron Szucs, Dr. Frans Dijkhuizen and Dr. Luca Peretti from ABB. In addition, I would like to thank Assoc. Prof. Yuriy Serdyuk, Prof. Stanislaw Gubanski and Prof. Hector Zelaya for their contribution to the project.

Many thanks to all my dear colleagues in the division of Electric Power Engineering and all my Master thesis students for making such a nice environment to work in. Special thanks to Robert Karlsson for the lab support and to my roommates, Mattias and Mebtu for not only being colleagues, but also great friends!

Last, but certainly not least, heartfelt thanks go to my family for all their help and support which I am forever grateful for.

Amin Bahmani
Göteborg, March 2014

List of Publications

Journal articles

[I] M. A. Bahmani, T. Thiringer and H. Jimenez, "An accurate pseudo-empirical model of winding loss calculation for hf foil and round conductors in switch-mode magnetics,"
Accepted for publication in IEEE Transactions on Power Electronics, 2014.

[II] M. A. Bahmani, E. Agheb, T. Thiringer, H. K. Hoildalen and Y. Serdyuk, "Core loss behavior in high frequency high power transformersi: Effect of core topology," *AIP Journal of Renewable and Sustainable Energy,* , vol. 4, no. 3, p. 033112, 2012.

[III] E. Agheb, M. A. Bahmani, H. K. Hoildalen and T. Thiringer, "Core loss behavior in high frequency high power transformersii: Arbitrary excitation," *AIP Journal of Renewable and Sustainable Energy,* , vol. 4, no. 3, p. 033113, 2012.

Conference proceedings

[i] M. A. Bahmani, T. Thiringer, "A high accuracy regressive-derived winding loss calculation model for high frequency applications," *Power Electronics and Drive Systems (PEDS), 2013 IEEE 10th International Conference on*, pp.358,363, 22-25 April 2013.

[ii] M. Mobarrez, M. Fazlali, M. A. Bahmani, T. Thiringer, "Performance and loss evaluation of a hard and soft switched 2.4 MW, 4 kV to 6 kV isolated DC-DC converter for wind energy applications," *IECON 2012 - 38th Annual Conference on IEEE Industrial Electronics Society*, pp.5086,5091, 25-28 Oct. 2012.

[iii] M. A. Bahmani, E. Agheb, Y. Serdyuk and H. K. Hoildalen, "Comparison of core loss behaviour in high frequency high power transformers with different

core topologies," *20th International Conference on Soft Magnetic Materials (SMM)*, p. 69, Sep. 2011.

Contents

Chapter 1

Introduction

1.1 Background and Previous Work

Moving towards higher power density in power conversion units has been receiving wide attention over the past decade particularly in highly restricted applications such as remotely located off shore wind farms and traction [1–3]. Increasing the operational frequency is the most common solution to achieve higher power densities, since the weight and volume of the magnetic part, the bulkiest element in power electronics converters, are then decreased. This solution is well established in low power high frequency applications, while in the recent decade, the possibility of utilizing high frequency at higher power and voltage levels has generated wide interest as well. However, taking high power, high voltage and high frequency effects into account, there are several challenges to be addressed since the technology in this field is not mature enough yet. These challenges are basically related to the extra losses as a result of eddy current in the magnetic core, excess losses in the windings due to enhanced skin and proximity effects [4] and parasitic elements, i.e., leakage inductance and winding capacitances, causing excess switching losses in the power semiconductors which are usually the dominant power losses at higher frequencies [5]. These extra losses together with the reduced size of the transformer lead to higher loss densities requiring a proper thermal management scheme in order to dissipate the higher power losses from a smaller component. This would be even more challenging if, unlike line frequency power transformers, oil cooled design is not a preference.

One of the potential applications of the High frequency high power transformer (HFHPT) is high power isolated DC-DC converters for wind energy DC collection and transmission grids. This could lead to a great weight and size reduction, which is of a particular value for offshore wind installations as stated in [6], in which a 3MW, 500Hz transformer is shown to be more than three times lighter than the equivalent 50Hz one. Furthermore, possibility of using high frequency transformers

in traction application has been extensively studied in recent years [7]. The design of a 350 kW/8kHz transformer, as an alternative for the bulky 16.7 HZ transformer, is presented in [8], reporting a substantial weight and volume reduction on board of railway vehicles. These studies have primarily tended to focus on the benefit of utilising higher frequencies, rather than on the design methodology and optimization of such a transformer.

Most of the classical attempts for high frequency transformer design were focused on a parameter called area product whereby the power handling capability of the core is determined [9, 10]. However, it remains unclear whether this parameter is valid for high power high frequency applications or not. Petkov in [11] presented a more detailed design and optimization procedure of high power high frequency transformers. Some years later, Hurely [12] reported a similar approach accounting for non sinusoidal excitations. However, the effect of parasitics are essentially neglected in both approaches. In [13], two 400 kVA transformers based on silicon steel and nanocrystalline material for railway traction applications at 1 and 5 kHz, respectively were designed, while Ortiz in [14] reported an optimized high frequency transformer of 20kHz and 166kW based on round litz wires.

However, the optimization results are largely sensitive to design constraints, requirements and free parameters chosen for a specific target application. It would seem, therefore, that further investigations are needed in order to achieve high efficiency and high power density accounting for special thermal management schemes, different core materials, windings types and strategies, insulation mediums and other determinant factors. Moreover, although considerable research has been devoted to high frequency transformer design, rather less attention has been paid to the validity of the conventional theoretical and empirical methods to evaluate the power losses accounted for the specific current and voltage waveforms as well as power and frequency ranges. Under this scope, it is crucial to investigate the validity of conventional expressions of transformer losses and to modify and improve their accuracy in case of unacceptable deviations. This is of utmost importance, particularly at high power and high frequency applications where the component enhanced loss density makes it necessary for researchers and designers to more accurately evaluate these losses in order to properly implement a thermal management scheme. In addition, unlike the time-consuming FEM calculations, accurate analytical expressions can be easily implemented within optimization loops without compromising the accuracy.

1.2 Purpose of the Thesis and Contributions

The main objective of the work reported in this thesis is to propose a design and optimization methodology of a high power high frequency transformer accounting for the tuned leakage inductance of the transformer, heat conduction by means of a thermally conductive polymeric material as well as high isolation requirements,

particularly in remote DC offshore application, where a converter module should withstand the entire MVDC or HVDC link voltage.

To the best of the author's knowledge, the main contributions of the thesis are:

- Proposing a pseudo-empirical formula to accurately calculate the AC resistance factor of foil and round type conductors in switch-mode magnetics without the need to use finite element simulations. This formula can be used for both foil and round conductors in a wide range of frequencies and for the windings consisting of any number of layers with free number of turns per layer. The validity and usage of the expression is experimentally proved.

- Proposing a new analytical expression to accurately calculate the value of leakage inductance particularly when the converter operates at high frequencies. The expression takes into account the effects of high frequency fields inside the conductors as well as the geometrical parameters of the transformer windings. This expression is also validated using FEM simulations as well as measurements.

- Using the modified and derived theoretical expressions explained above, a design and optimization methodology accounting for the high isolation requirements of the off-shore based transformers as well as required leakage inductance of the dual active bridge (DAB) topology is proposed. This design methodology will later be used as a basis for further investigations regarding the different aspects of a high power density isolated DC-DC converter.

1.3 Thesis Outline

This thesis essentially consisted of two main parts. The first and main part comprising Chapters 2 to 4, is focused in general on investigation and development of precise transformer characterization tools in order to accurately evaluate different power losses of the studied transformer. Using those developed tools, a design and optimization methodology has been proposed in the second part, Chapter 5.

Chapter 2

High Frequency Winding Losses

2.1 Introduction

Moving towards higher power density in power conversion units has been receiving wide attention over the past decade particularly in highly restricted applications such as wind farm and traction [1–3]. Operating higher up in frequency is the most common solution to achieve higher power density, since the weight and volume of the magnetic part, the bulkiest element in power electronics converters, are then decreased. However, on the other hand it will lead to higher loss density due to enhanced core loss and more importantly enhanced winding loss which make it necessary for researchers and designers to more accurately evaluate these losses in order to properly implement a thermal management scheme [15, 16].

Bennet and Larson [17] were the first ones who solved and formulated the multilayer winding loss based on simplified 1-D Maxwell equations, however, the most popular analytical formula, widely used by designers to evaluate winding loss in transformers, has been derived by Dowell [18]. The physical validity of the original Dowell's equation has been questioned in several publications [19, 20] in which the main assumption by Dowell regarding the interlayered parallel magnetic field has been shown to be violated [21]. Utilizing 2-D finite element method, these works mostly focused on to improve Dowell's formula accuracy by defining new correction factors which present better understanding of the high frequency conductor losses [22, 23]. Although 2-D finite element method takes the 2-D nature of the magnetic field between winding layers and core into account, it requires a time consuming process to create a model and solve it for only one specific magnetic device .i.e. transformer, inductor and so on and on the other hand, the formulas derived by this method are usually limited to some part of the possible winding configurations [24].

Most of the classical attempts for winding loss calculation were focused on foil type conductors, widely used in high power magnetic components due to their rela-

tively larger copper cross-section needed for keeping the maximum current density within an acceptable range [9]; however, by defining some forming and porosity factors, they have been applied on solid round wires as well [25, 26]. Apart from those Dowel base expressions, Ferreira [27] proposed a formula derived from the exact solution of the magnetic field in the vicinity of a solid round conductor, However, Sullivan [28] described a relatively high inaccuracy for Ferreira's method and Dimitrakakis [24] examined its deviation from FEM simulation. Morover, several publications proposed different approaches resulting in an optimum diameter for which the skin and proximity effect are minimized [29, 30].

The main aim of this chapter is to propose a pseudo-empirical formula to precisely calculate the AC resistance factor of the foil and round type conductors in switchmode magnetics without the need to use finite element simulations. In order to obtain such a formula, an intensive 2-D FEM simulation set to cover a wide range of possible winding configurations has been performed and the obtained AC resistance factor summarized in a multi-variate Pseudo-empirical expression. Unlike previous attempts which either covered parts of the possible winding configurations or defining correction factors for previously available well-known analytical expressions [31], this formula can be used for both foil and round conductor in a wide range of frequencies and for the windings consisted of any number of layers with free number of turns per layer.

The first part of this chapter, provides an overview of the previous well-known analytical methods for calculation of AC resistance factor in foil and round conductors. Furthermore, a quantitative comparison between those models and FEM simulations has been performed in order to specify the magnitude of deviation and gives a clear picture of the validity range of each method. The next part, thoroughly explains the methodology used to derive the final Pseudo-empirical formula and provides a full range comparison between Dowell's expression and the new pseudo-empirical in terms of accuracy and domain of validity. At the end, the experimental results are presented. Several transformers with different winding configurations have been built to verify the accuracy of the new method over the domain of validity.

2.2 Validity Investigation

2.2.1 Dowell's Expression for Foil Conductors

The influence of skin and proximity effects on transformer AC resistance has been studied for many years, based on the expression proposed by Dowell [18]. This model was initially derived from solving the Maxwell equations under certain circumstances, shown in Fig. 2.1a, resulting in one dimensional diffusion equation. As can be seen in Fig. 2.1a, the main assumptions in Dowell's expression is that each winding portion consisting of several layers of foil conductors occupies the whole

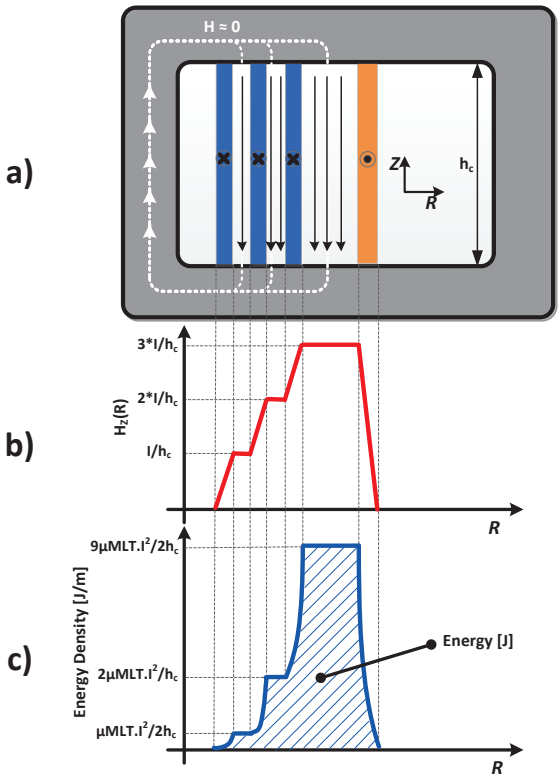

Figure 2.1: (a) Cross-sectional view of the winding configurations according to Dowell's assumptions. (b) Magnetic field distribution. (c) Energy distribution.

core window height. The permeability of the magnetic core is assumed to be infinity, therefore the magnetic field intensity within the core is negligible while it is closing its path along the foil conductors and intra-layer spaces inside the core window. As a result, the magnetic field vectors has only Z components and vary only in R direction, therefore, the diffusion equation can be written as a second order differential equation

$$\frac{\partial^2 H_Z(R)}{\partial R^2} = j\omega\sigma\mu H_Z(R) \tag{2.1}$$

where σ and μ are the conductivity and permeability of the foil conductors respectively.

Fig. 2.1b shows the distribution of the magnetic field inside the core window when the frequency is low enough to homogeneously distribute the current inside the foils. As can be seen in Fig. 2.1b, the magnetic field is zero outside the windings area and it is at its maximum in the area between the two windings; This conditions has been applied to (2.1) as boundary conditions to obtain the magnetic field distribution inside the conductors, however, in Fig. 2.1b, the frequency is assumed low enough

to have a homogenous distribution of current inside the foils. In the same fashion, the magnetic energy stored in the leakage inductance of the transformer has been shown in Fig. 2.1c.

Given the magnetic field distribution achieved from (2.1), Dowell calculated the current distribution and its associated power loss resulting in an easy to use formula which gives the AC resistance factor of transformer windings as

$$RF = \frac{R_{AC}}{R_{DC}} = M(\triangle) + \frac{m^2 - 1}{3} D(\triangle) \tag{2.2}$$

where the terms M, D and $\triangle$ are defined as

$$\begin{aligned} M(\triangle) &= \triangle \frac{\sinh 2\triangle + \sin 2\triangle}{\cosh 2\triangle - \cos 2\triangle} \\ &= \triangle \frac{e^{2\triangle} - e^{-2\triangle} + 2\sin 2\triangle}{e^{2\triangle} + e^{-2\triangle} - 2\cos 2\triangle} \end{aligned} \tag{2.3}$$

$$\begin{aligned} D(\triangle) &= 2\triangle \frac{\sinh \triangle - \sin \triangle}{\cosh \triangle + \cos \triangle} \\ &= 2\triangle \frac{e^{\triangle} - e^{-\triangle} - 2\sin \triangle}{e^{\triangle} + e^{-\triangle} + 2\cos \triangle} \end{aligned} \tag{2.4}$$

$$\triangle = \frac{d}{\delta} \tag{2.5}$$

where m is the number of layers for each winding portion, $\triangle$ is the penetration ratio which is the ratio between the foil thickness, d, and the skin depth, δ at any particular frequency.

The initial assumption of Dowell's expression regarding the height of the copper foil is not applicable in many practical cases where the height of the foil can not be the same as window height,e.g. tight rectangular conductors, short foils and so on. In order to take these cases into account, Dowell introduced the porosity factor, η, which is the ratio of the window height occupied by the foil conductors to the total window height [18].

One of the purposes of this chapter is to investigate the validity range of the well-known classical models. Although experimental measurements is the most accurate way to check the validly of the theoretical models, FEM simulations are the most popular way to do this investigation since it provides the possibility of sweeping different parameters in the model. All of the FEM simulations in this chapter are performed using the commercial electromagnetic software, Ansys Maxwell [32], in which both the skin and proximity effect are taken into account, however the precision of the computation is dependent to the mesh quality. For this reason, firstly, at least six layers of mesh are applied within the first skin depth from the sides

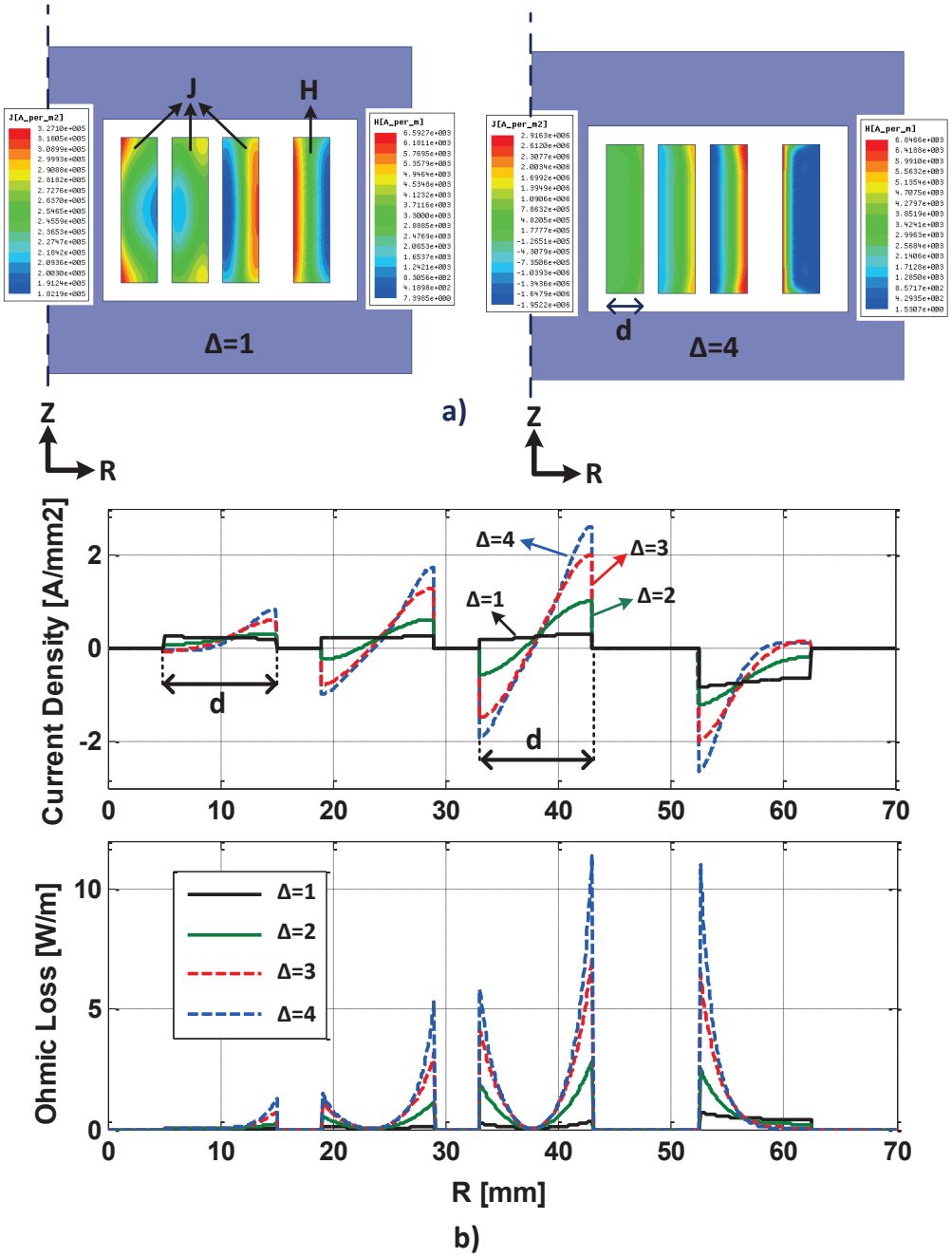

Figure 2.2: (a) Sample 2D axisymmetric FEM simulation at two different △. (b) Normalised current density and ohmic loss at core window space.

of all the conductors in the simulation's geometry and secondly, the mesh structure of each geometry structure is refined in several stages until the simulation error reduces to less than 0.5%. As a result, each simulation creates a substantial number of mesh elements resulting in a longer computational time [33], whereby, using three dimensional geometries requiring much more mesh elements seems to be inefficient, making iterative simulations unfeasible [34]. Consequently, all the simulations in this chapter have been performed under 2D symmetry pattern around Z axis where the windings should be wound around the middle limb of the transformer to retain the symmetrical shape of the magnetic field. Nevertheless, the real geometry of most of the transformers, except for the pot core transformer, consist of the winding portions that are not covered by the core, e.g. E core, C core and so on, whereas in 2D axisymetric simulations windings are thoroughly surrounded by the core. For this reason, the ohmic loss of several transformers were compared in both 2D axisymmetric and 3D simulations with extremely fine mesh, in order to have a comparable mesh densities between 2D and 3D, which showed a negligible difference between 2D and 3D simulations in terms of the magnetic field distribution and resulted ohmic loss. The worst case studied was for a very low value of η, 0.2, on which the 3D simulation showed 6% less ohmic loss than the one in the 2D case which is still an acceptable error justifying the use of 2D simulations over the time consuming 3D one.

Fig. 2.2a shows a sample 2D axisymmetric FEM simulations of the transformer windings at different values of $\triangle$ illustrating the computed current density distribution and magnetic field intensity in the primary and secondary windings respectively. The dimensions of the geometry were kept constant and different values of $\triangle$ were achieved by applying the frequencies corresponding to those values. In other words, the analysis is based on a dimensionless parameter, $\triangle$, taking into account the effects of both frequency and geometrical dimensions. The normalised current density and ohmic loss distribution on inter-layer space, obtained from the same FEM simulation at four different values of $\triangle$, are shown in Fig. 2.2b top and bottom respectively.

As can be seen in Fig. 2.2b, the current density increases by adding the number of layers, resulting in higher ohmic losses on the third layer of the primary windings than the ohmic losses in the first and second layer, because of this fact that in contrast to the first layer, which does not suffer from the magnetic field on its left hand side, the second layer and more significantly the third layer suffer from the presence of the magnetic field on their left hand side, causing an induced negative current on the left hand side of the conductor. Hence, the ohmic loss on the second and third layer are close to five and thirteen times, respectively, higher than the ohmic loss in the first layer of the primary windings. Moreover, the penetration ratio, $\triangle$, is another major determinant of ohmic loss pattern which significantly changes the distribution of current within a conductor. As illustrated in Fig. 2.2b, the AC resistance of the windings rapidly increases by increasing the penetration

ratio, i.e, by either increasing the frequency or increasing the foil thickness, leading to significantly higher ohmic losses. Despite the major redistribution of the current due to the skin and proximity effects, one can notice that the net value of the current in each layer is constant. For instance, as can be seen in Fig. 2.2b, although the positive current significantly increases by increasing $\triangle$, but there is an opposite negative current on the other side of the conductor which balances the net current in each layer.

In order to determine the limitations and validity range of Dowell expression used in many magnetic design approaches, the result of a series of numerical tests, examining the effect of variation in different geometrical aspects on AC resistance factor at different frequencies, are compared with the AC resistance factor obtained from Dowell equations. The dimensions of these numerical tests were kept constant and higher $\triangle$ achieved by increasing the frequency for each η and each number of layer. Fig. 2.3 shows that the Dowell's resistance factor deviation from FEM resistance factor, calculated as (2.6), versus η for 4 different number of layers up to 4 layers and 5 different penetration ratios up to 5. RF_{Dowell} can be calculated by (2.2), however in order to obtain RF_{FEM}, first, the value of ohmic loss P_ω over the winding area should be extracted from the solved simulation and then, by knowing the value of current through the conductors, AC resistance can be calculated for the interested frequencies and geometries. The porosity factors varies from 0.3 to 1, although it should be noted that porosity factors of less than 0.4 is very implausible in practice and including such low values is only for the sake of comparison.

$$RF_{Error}\,[\%] = 100 \times \frac{RF_{Dowell} - RF_{FEM}}{RF_{FEM}} \tag{2.6}$$

Some remarks can be highlighted in Fig. 2.3. First, it is worth mentioning that the variation in penetration ratio, $\triangle$, substantially affect the Dowell expression accuracy. As shown in Fig. 2.3 the accuracy of Dowell expression reduces by increasing $\triangle$, for any number of layer, m, and porosity factor, η, resulting in an unreliable transformer design aiming to work at higher $\triangle$. The second parameter which adversely affect Dowell expression accuracy is the porosity factor. As illustrated in Fig. 2.3, for any m and $\triangle$, for higher porosity factor ($\eta \geq 0.8$) the accuracy of Dowell expression is within $\pm 15\%$ which is a relatively acceptable deviation for an analytical tool. However, the equation does not retain its precision for lower values of η in which its accuracy is within $\pm 60\%$. This high deviation becomes more problematic when it is negative since it corresponds to the cases where Dowell expression underestimates the ohmic loss or AC resistance factor. Morover, this deviation becoming more prominent by increasing the number of winding layers as proximity effect becoming more influential on the current distribution inside the conductors.

This inaccuracy could stem from the rigourous assumptions Dowell made to simplify the derivation process. The major simplification which could contribute to the noted deviation is that the foil windings are assumed to occupy the total height of

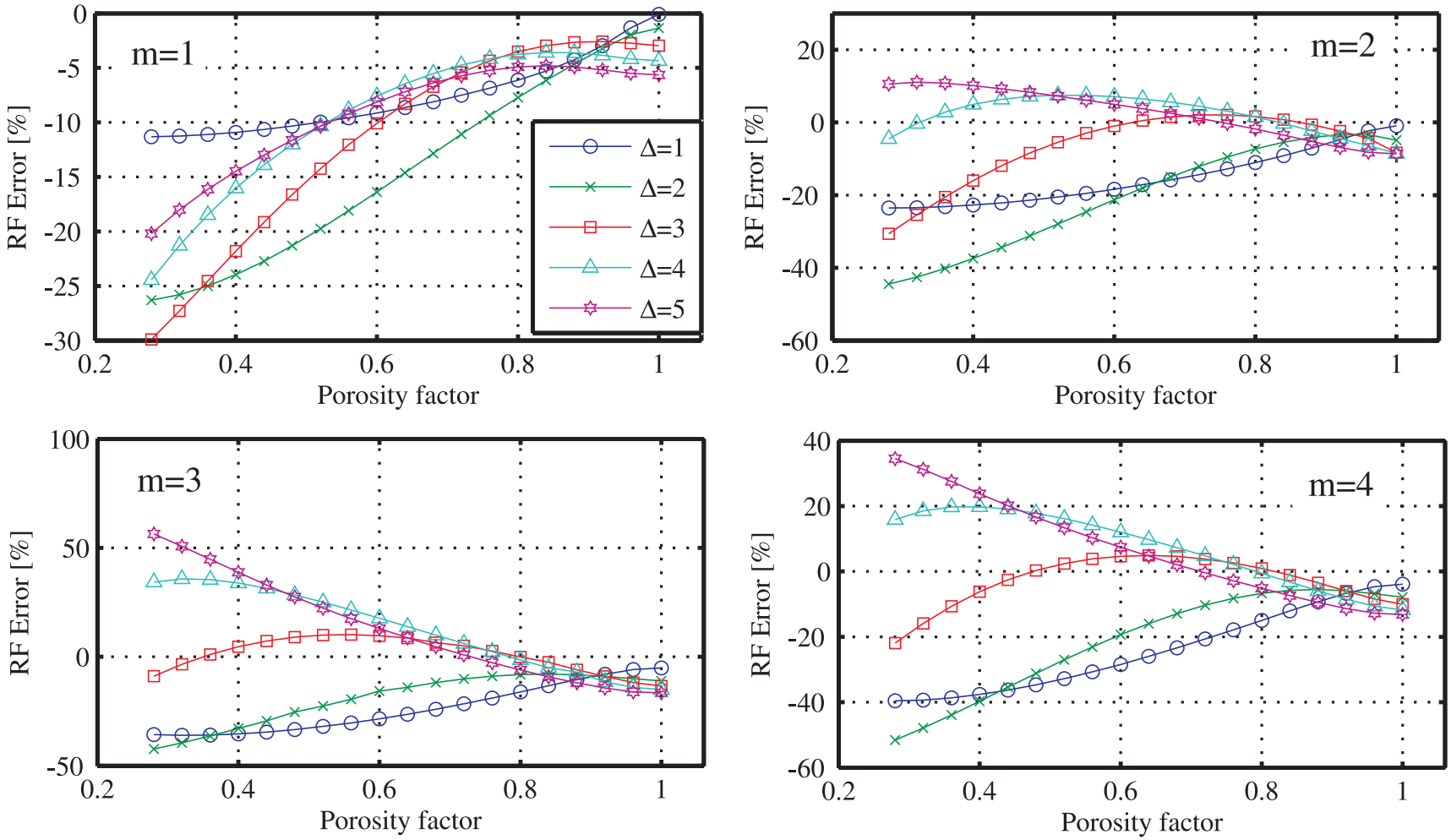

Figure 2.3: Dowell's Foil Resistance factor Deviation from FEM resistance factor versus η at 5 different values of $\triangle$ and 4 different number of winding layer, m.

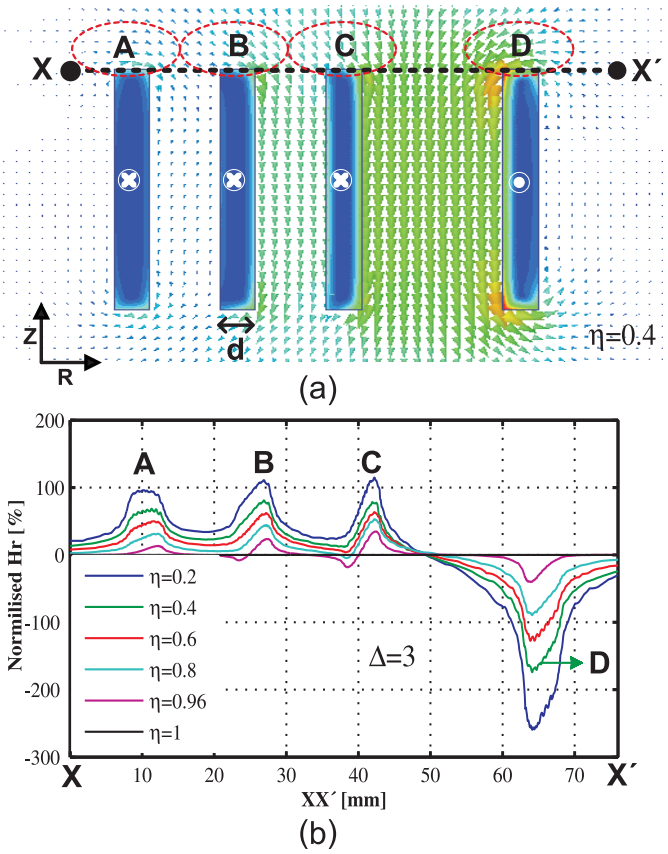

Figure 2.4: (a) 2D simulation of edge effect on magnetic field at $\eta = 0.4$. (b) Normalised radial magnetic filed intensity on $XX^{'}$ at 6 different values of η.

the transformer window, resulting in presence of only Z component of magnetic field within and between foil layers. However, this assumption is usually being violated in many practical designs due to the safety requirements [35], causing presence of the second component of magnetic field. Therefore, the 2D magnetic field intensifies by decreasing the length of the foil conductors (decreasing η), causing inaccuracy in Dowell's expression. Consequently, one can say that the 1D approach is generally applicable among designers as long as the foil conductors covers the majority of the transformers window height [36, 37].

2.2.2 Edge Effect Analysis

The aim of this section is to quantitatively investigate the cause of inaccuracy in the analytical expressions, i.e. Dowell, Ferreira and other analytical expressions derived based on simplifying initial assumptions. In order to perform edge effect analysis, the magnetic field distribution inside a transformer window, comprising

three layers of foil conductors as primary and one layer of foil as secondary, has been studied. Fig. 2.4(a) shows the magnetic field distribution inside a transformer window consisting of foil conductors with $\eta = 0.4$ and $\triangle = 3$. As can be seen at areas shown by the red ellipse, the magnetic field vectors are not only in Z direction but also their R component is considerable particularly at the end windings between the primary and secondary windings at which the magnetic field intensity is significant [38].

In order to more quantitatively examine the influence of winding height on the formation of the second component of the magnetic field, 6 simulations performed on the geometry shown in Fig. 2.4(a) with different conductor heights corresponding to the porosity factors of 0.2 to 1. Frequency and foil thickness are fixed to accomplish $\triangle = 3$. The magnetic fields in radial direction are then extracted on an imaginary line, $XX^{'}$, connecting the edge of the inner primary foil to the edge of the secondary foil conductors for different values of η. Moreover, these values are normalised to the maximum magnetic field between the primary and secondary windings, $max(H_Z)$, when the foil conductors occupy the whole window height at which the magnetic field exists only in Z direction.

The phenomenon, edge effect, is clearly demonstrated in Fig. 2.4(b) where the ratio of radial magnetic field intensity to the maximum value of magnetic field in Z direction on $XX^{'}$ is illustrated in percentage for 6 different values of η. The result reveals that the magnetic field distribution inside the transformer window is highly two dimensional at sides of the conductors highlighted in Fig. 2.4(a) and (b). Moreover, by reducing the height of the foil conductors, edge effects considerably increase, e.g. the normalised radial magnetic field at region D is -250%, -170% and -80% for the porosity factors of 0.2, 0.4 and 0.8, respectively whereas as shown in Fig. 2.4(b), the contribution of radial magnetic field at $\eta = 1$ is almost 0% which agrees with Dowell's initial assumption.

Comparing the results shown in Fig. 2.3 and Fig. 2.4(b), one can conclude that Dowell's general overestimation is associated with percentage of the second component of the magnetic field [39]. It is now more clear to justify the inaccurate results obtained by Dowell's equation when a transformer window is not fully occupied by the conductors. It should be noted that although in some cases, e.g. $\eta \approx 0.2$, the radial magnetic field intensity could be as high as 250% of its orthogonal component, the total deviation of 1D models from FEM is not more than 70% as previously shown in Fig. 2.3. This is because those highly two-dimensional magnetic field are limited to the specific areas inside the transformer window whereas the magnetic field direction is mostly in Z direction at other regions. It is worthwhile mentioning that edge effect does not always result in excess losses, but also could improve the total losses in the windings. This attribute is demonstrated in Fig. 2.3 where at high values of $\triangle$ (4 and 5) and $m > 1$, total copper losses seems to be improved by intensifying edge effect. However, it should be expressed that, specifying the

condition in which edge effect improves the winding losses, is strongly dependent to the geometrical characteristics of the transformer making the conclusion more complex [24].

2.2.3 Round Conductors

Solid round conductors, magnet wires, are widely used in transformers, motors and other magnetic components since they are commercially available in a wide range of diameters with a relatively low price [30,40]. Also, round wires require less practical efforts to be tightly wound around a core [9, 41]. In this part, two of the most commonly used analytical expression, among others, for calculating AC resistance factor in round wires, Dowell and Ferreira, are introduced. The accuracy of these methods are then examined by setting a large number of FEM simulations covering a wide range of parameter variations in order to determine their domain of validity.

Dowell [18] proposed a special factor in order to evaluate the AC resistance factor with a similar approach as in foil analysis. In this method, round wire cross section is related to the equivalent rectangular solid wire with the same cross sectional area and by taking the distance between wires into account, it relates every layer of round wire to its equivalent foil conductors. Therefore, the main structure of (2.2) is proposed to be viable for round wires by replacing $\triangle$ as

$$\Delta' = \frac{d_r}{2\delta}\sqrt{\pi.\eta} \tag{2.7}$$

where d_r is the diameter of the solid round wire and η is the degree of fulfillment of window height as described in foil section.

In addition, Ferreira [26] proposed another closed form formula derived based on the exact solutions of the magnetic field inside and outside a single solid round wire by considering the orthogonality between skin and proximity effects [**?**]. As Dowell approach, Ferreira took into account the multilayered arrangement of round wires in order to calculate the AC resistance factors for each winding portion, however, Ferreira's original method is generally referred as inaccurate since it did not account for the porosity factor [24]. Therefore, Bartoli [42] modified Ferreira's formula by defining porosity factors similar to the one in Dowell's expression, although this method is still referred to as Ferreira's expression given as

$$RF = \frac{\Delta}{2\sqrt{2}}\left(M_1(\Delta) - 2\pi\eta^2\left(\frac{4\left(m^2-1\right)}{3}+1\right)M_2(\Delta)\right) \tag{2.8}$$

$$\Delta = \frac{d_r}{\delta} \tag{2.9}$$

where m is the number of layers, η accounts for the percentage of copper covering the transformer window height and d_r is the diameter of the solid round wire. $\triangle$,

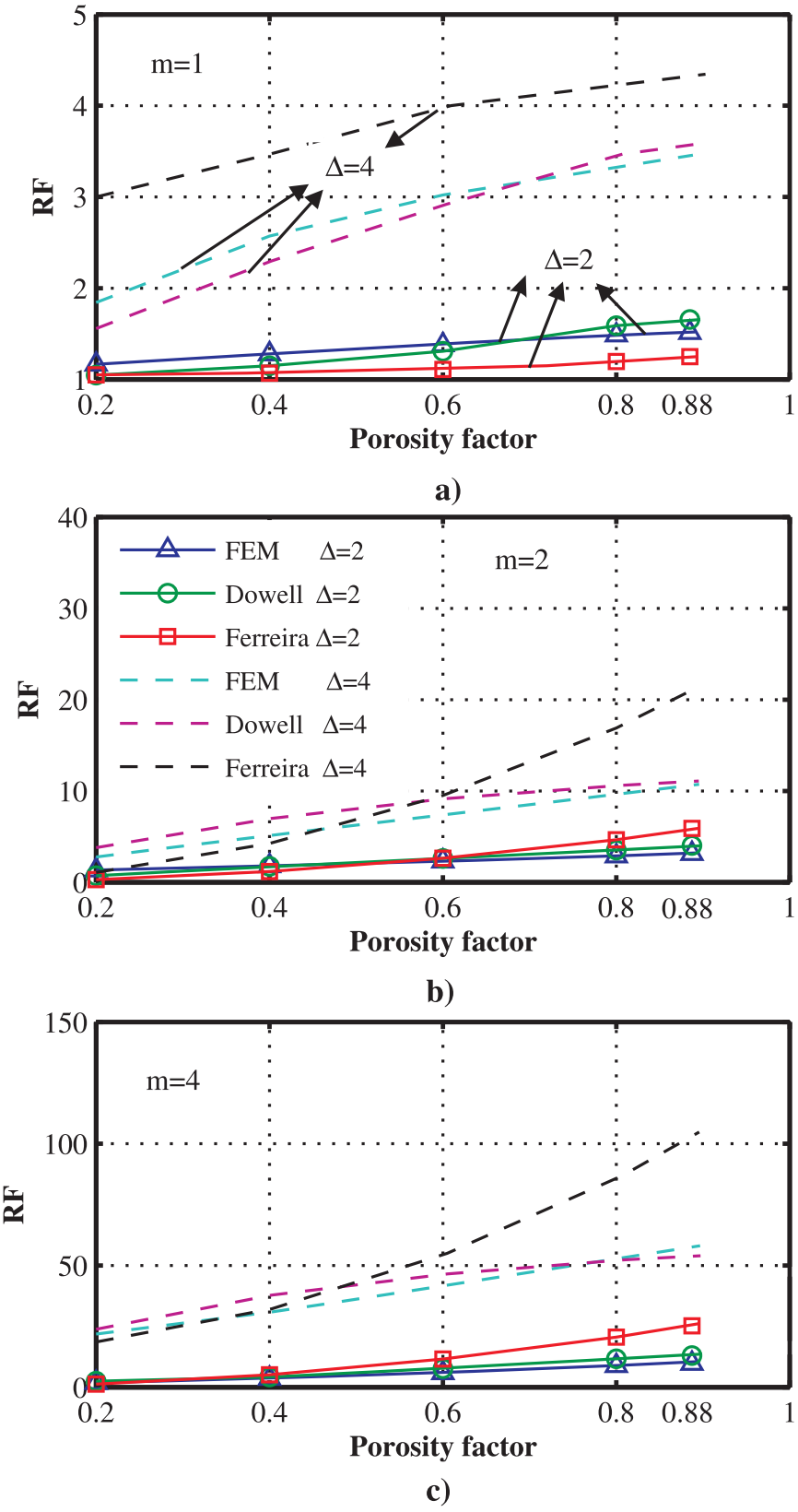

Figure 2.5: Comparison between resistance factors obtained from analytical models, Dowell and Ferreira, relative to the FEM results performed at different values of η, Δ and m.

$M_1(\Delta)$ and $M_2(\Delta)$ are defined as

$$M_1(\Delta) = \frac{ber(\frac{\Delta}{\sqrt{2}})bei'(\frac{\Delta}{\sqrt{2}}) - bei(\frac{\Delta}{\sqrt{2}})ber'(\frac{\Delta}{\sqrt{2}})}{(ber'(\frac{\Delta}{\sqrt{2}}))^2 + (bei'(\frac{\Delta}{\sqrt{2}}))^2} \tag{2.10}$$

$$M_2(\Delta) = \frac{ber_2(\frac{\Delta}{\sqrt{2}})ber'(\frac{\Delta}{\sqrt{2}}) + bei_2(\frac{\Delta}{\sqrt{2}})bei'(\frac{\Delta}{\sqrt{2}})}{(ber(\frac{\Delta}{\sqrt{2}}))^2 + (bei(\frac{\Delta}{\sqrt{2}}))^2} \tag{2.11}$$

The functions *ber* and *bei*, Kelvin functions, are the real and imaginary parts of Bessel functions of first kind, respectively.

In order to analyse the accuracy of the aforementioned methods, a set of parametric FEM simulations covering a wide range of parameter variations, i.e. $0.2 \leqslant \eta \leqslant 0.88$, $1 \leqslant m \leqslant 4$ and two values Δ, have been performed. The results were then compared with the resistance factors obtained from Dowell and Ferreira's expression and illustrated in Fig. 2.5.

As can be seen in Fig. 2.5, Ferreira's formula generally shows a high inaccuracy for almost the whole range of investigation. For instance, at $m = 4$, $\eta = 0.8$ and $\Delta = 4$, Ferreira estimates the resistance factor as high as 80 whereas FEM analysis shows about 50 which is a significant overestimation resulting in unrealistic and costly magnetic design. This inaccuracy could stem from the rigourous assumption Ferreira made regarding the orthogonality between skin and proximity effect which is not a valid assumption when a solid round wire, conducting high frequency currents, is surrounded by a large number of other conductors with a complex arrangement. This attribute can be seen in Fig. 2.5(b) and (c) where Ferreira's resistance factor becomes closer to the FEM result by decreasing η. In other words, by having a sparser winding arrangement, the behaviour of the magnetic field inside the conductors becomes closer to the initial assumption resulting in a relatively more orthogonal skin and proximity magnetic field [24].

Unlike Ferreira's model, Dowell shows an acceptable accuracy particularly at $\Delta = 2$ which is cited to be the optimum penetration ratio for a solid round conductors [29]. However, as shown in Fig. 2.5, at lower values of η, Dowell's expression loses its validity because of the edge effect forming 2D magnetic field inside transformer window. On the other hand, for $\eta \geq 0.6$ Dowell's expression leads to deviations of always less than 20%, nevertheless at lower Δ, around 2, this deviation improves up to approximately 10% which is substantially more accurate than Ferreira's method.

It is worthwhile mentioning that besides violating the initial assumptions, the aforementioned theoretical methods do not account for all the geometrical aspects of a real winding arrangement such as inter-layered distances, vertical and horizontal clearing distances of the winding portion to the core, causing relatively high inaccuracy at high frequency applications. These are the reasons why researchers and designers have been seeking for alternatives methods. One of the essentially reliable

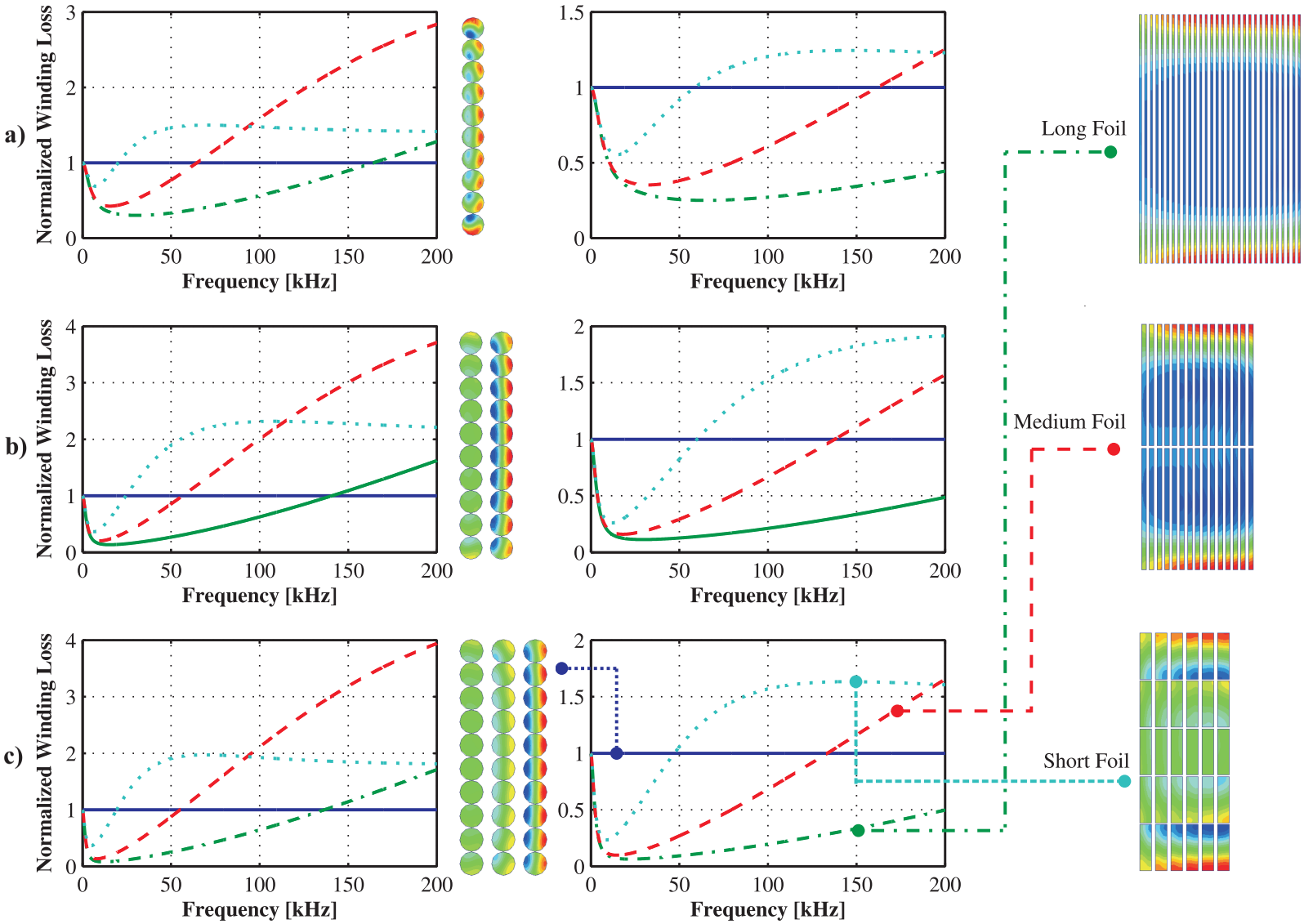

Figure 2.6: AC winding loss comparison between the round conductors and the corresponding foil conductor with different arrangements and the same currentdensity (a-left) $m = 1$, $\eta = 1$. (a-right) $m = 1$, $\eta = 0.7$. (b-left) $m = 2$, $\eta = 1$. (b-right) $m = 2$, $\eta = 0.7$. (c-left) $m = 3$, $\eta = 1$. (c-right) $m = 3$, $\eta = 0.7$.

methods is performing FEM simulation for every case study instead of using theoretical models, resulting in time consuming optimisation process in which thousands of scenarios may be needed to be examined. Consequently, several investigations have been performed [20, 31, 43] in order to develop the well-known closed form expression by introducing several correction factors obtained from numerous finite element simulations. However, their applicability is usually limited since the conditions in which the FEM analysis carried out is not sufficiently general, e.g. considering only single layer configuration or neglecting the determinant parameters on winding loss. Under this scope, a pseudo-empirical formula, accounting for the influence of all the determinant geometrical aspects on the magnetic field, with adequate degree of freedom, has been proposed and validated in this chapter. Integrating the accuracy of FEM simulations with an easy to use pseudo-empirical formula accounting for almost all practical winding arrangement, this method covers the area in which previous closed form analytical models, either the classical models or the FEM based modified models, substantially deviates from the actual conductor losses.

As mentioned before, the round conductors are widely used in switch-mode magnetics due to the availability of different types as well as ease of use while foil conductors require more practical efforts to be wound around a core particularly when complex winding strategy needs to be implemented. However more investigations are needed to determine the suitability of one conductor type in different application. For instance, having a higher winding filling factor is one of the important design requirements in high power density applications where the weight and volume of the magnetic components should be decreased and on the other hand different losses need to be reduced.

Fig. 2.6 present a FEM-based comparison of the obtained AC winding losses between the round and foil conductors in different steps and on the basis of the same current density inside round and its respective foil conductors. The overall results indicate that there is always a crossover frequency where the AC winding losses of the foil conductors exceeds the AC winding losses of its corresponding round conductors with the same current density and porosity factor. For instance, Fig. 2.6(c-right) illustrates the winding loss of a winding portion comprising of three layers of round wires, 10 turns in each layer, and the porosity factor of 0.7 (solid blue line). The dash lines represent value of the AC winding losses of the long foil with the highest number of layers, 30, the medium foils with 15 layers, 2 turns each, and the short foils with 6 layers, 5 turns each, respectively normalized by the AC winding losses of the respective 3 layers of round wire (shown in the right side of the Fig. 2.6). The current density in all of the configurations is constant and set to 2.5 A/mm^2 and the porosity factor is 0.7. It can clearly be seen that until a certain frequency the AC winding loss of the foil conductor is less than the one for the corresponding round conductors. This crossover frequency increases by having the longer foils which obviously have thinner thicknesses compared to

the shorter foils. This attribute, along with the higher filling factor of the foil conductors, makes this kind of conductor an interesting option for high power density applications. However, one should consider that having the highest number of layers and the thinnest foils could not always be a realistic solution since this structure would suffer from the high value of the winding capacitance particularly at high voltage applications. Therefore, there is always a compromise between the number of layers, size of the transformer, maximum allowed winding loss with respect to the transformer application. The discussed crossover frequency is shifted towards lower frequency at higher values of the porosity factor, therefore there is still a frequency range where foil conductor has preference over its corresponding round conductors. This attribute can be seen in Fig. 2.6(c-left) witch is similar to the right one but with the porosity factor of 1. Similar results is obtained for 2 and 1 layer of round conductors as illustrated in Fig. 2.6(a and b).

Being limited to just one type of conductor, foil or round, one can say, if possible, by decreasing the number of layers and increasing the transformer window height, the AC resistance factor and accordingly the AC winding loss reduces because of the less compact winding arrangement reducing the proximity effect. This is what already observed during the validity investigations of the well-known analytical models. However, due to mechanical and practical issues this option is usually limited.

2.3 Pseudo-Empirical Model Establishment

The main purpose of this chapter is to propose an easy-to-use closed form formula to accurately calculate the AC resistance factor at given geometrical dimensions as well as at different frequencies. The proposed strategy to obtain such a pseudo-empirical expression is illustrated in Fig. 2.7, summarized as follows.

1. The determinant geometrical parameters required to form a unique transformer window is introduced and their influence on winding loss is investigated.

2. The effective geometrical variables are then merged to form a set of generic dimensionless variables.

3. A proper range of variation, forming most of the feasible transformer window configuration, is defined for each generic parameters to be used as the input variables for FEM simulations.

4. After extracting the matrices of AC resistance factors, corresponding to the generic variables, from the numerous FEM simulations, the mathematical regression is performed in order to determine the coefficients needed to fit the

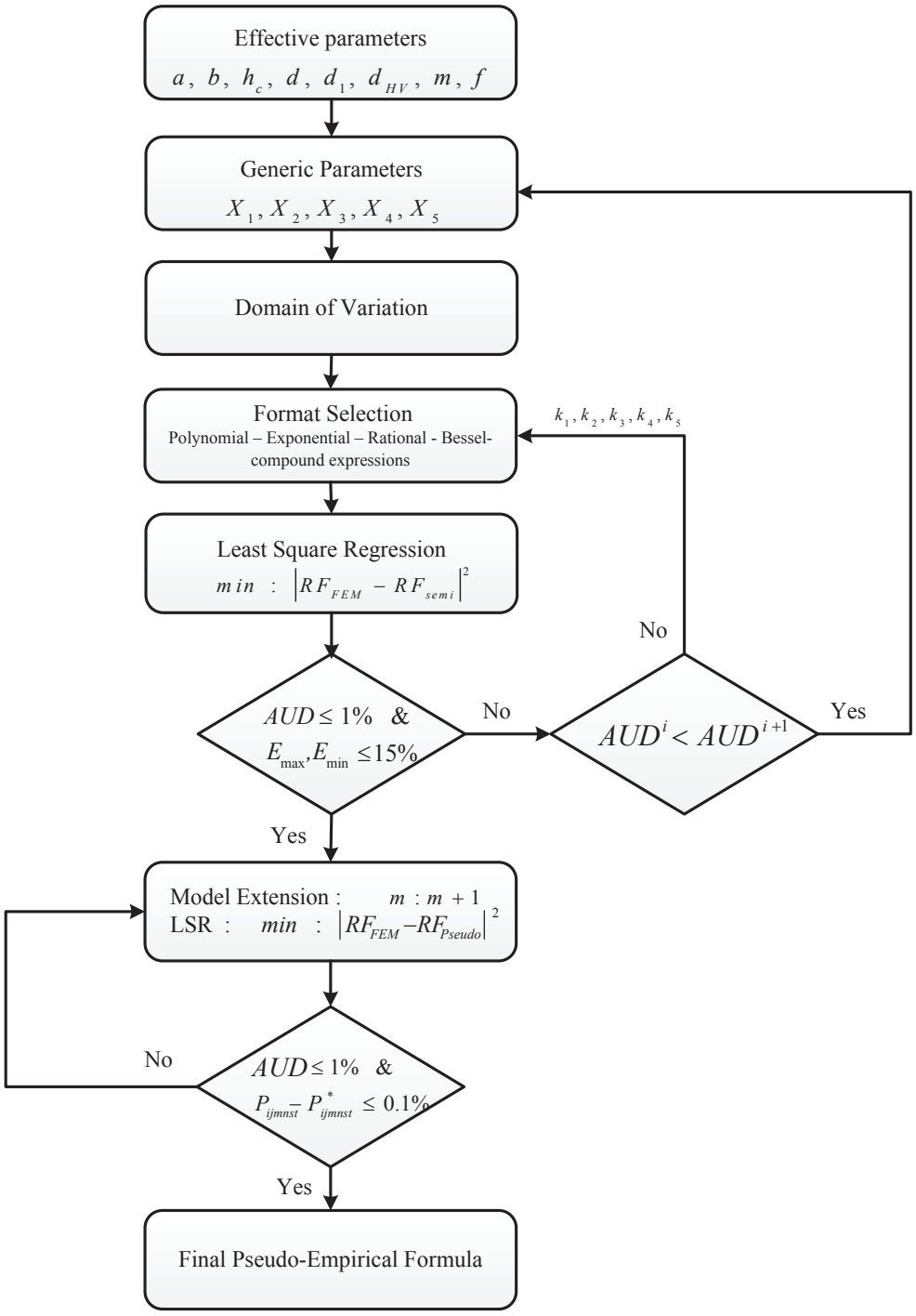

Figure 2.7: Approach to establish the pseudo-empirical model.

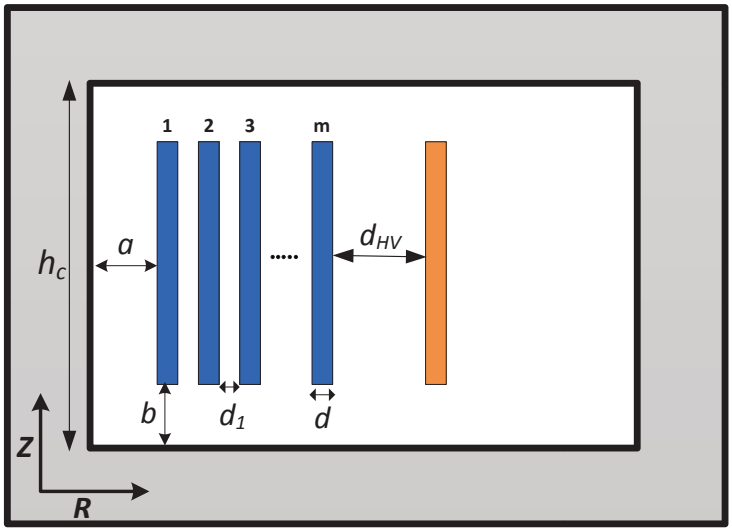

Figure 2.8: Definition of the variables.

prospective formats of the final expression with respect to the desired precision.

5. Once the selected structure of the expression fulfilled all the requirements, a new regression process triggers by expanding the variation range of one of the generic parameters in order to reinforce the validity of the final expression.

Each step is now described in detail.

2.3.1 Determinant Variable Definition

The first step to obtain such a formula is to determine all the parameters, either geometrical or electrical, which can influence the magnetic field distribution and accordingly the AC resistance factor. In addition, the sensitivity of the resistance factor to those parameters is examined in order to decrease the number of influencing factors since the complexity of the regression process and the number of the coefficients for the final formula substantially depends on the number of the input parameters.

In this part, different geometrical and electrical variables affecting the resistance factor are examined in order to take the most influencing ones in to account. Fig. 2.8 shows the schematic of a transformer window comprising the magnetic core with the relatively high permeability of 20000 and the copper foil winding. This high value of the permeability belongs to the extremely low core-loss magnetic materials called nano-crystalline, however other magnetic materials does not have such high values.

Table 2.1: Sensitivity analysis of the geometrical parameters.

m	$\frac{\partial RF}{\partial a}$	$\frac{\partial RF}{\partial b}$	$\frac{\partial RF}{\partial d_1}$	$\frac{\partial RF}{\partial d_{HV}}$	$\frac{\partial RF}{\partial d}$
1	-0.00012	-0.00145	-	0.000011	0.542
2	-0.001	-0.0179	0.0081	-0.000025	2.097
3	-0.0025	-0.0512	0.0337	-0.000025	4.911
4	-0.0071	-0.1021	0.0723	-0.000025	8.861

Hence, prior to deriving the Pseudo-Empirical model, it is necessary to monitor the effect of different values of the relative permeability on the AC resistance factor. For this purpose the powder core magnetic materials which usually has the lowest relative permeability of around 60 is simulated. It was seen that the obtained value of the AC resistance factor is only 0.3% less than the one with the permeability of 20000. This is because of the fact that the main reason of considering high permeability in winding loss study is to make sure that the magnetic field intensity inside the magnetic core is close to zero. This can be fulfilled even with the magnetic cores with low permeabilities of around 60 to 100.

The whole geometry can be uniquely described by 7 parameters defined in Fig. 2.8, in which h_c is the window height, m is the number of foil layers in primary side, d is the foil thickness, d_1 is the insulation thickness between the primary foils, d_{HV} is the clearance between the primary and secondary windings, a and b are the horizontal and vertical creepage distance respectively.

In order to determine how these parameters affect the AC resistance factor, a sensitivity analysis has been carried out by sweeping the geometrical variables using FEM simulations. The studied parameter is assigned 20 different values while other parameters are kept constant. Afterwards, the average value of the partial derivative of the AC resistance factor with respect to the varying parameter has been explored to determine the most and the least sensitive parameters on the AC resistance factor.

Table. 2.1 shows the average value of $\frac{\partial RF}{\partial x}$ over the range of variation of the variable x at 4 different number of turns of primary windings where x can be replaced by each of the geometrical parameters defined in Fig. 2.8. As can be seen in Table. 2.1, the foil thickness is the most effective variable on RF, whereby the AC resistance factor substantially increases by increasing foil thickness, e.g. for $m = 3$ at 2 kHz, the incremental rate of RF for a 1 millimeter increase in d is 4.911. On the other hand, the distance between the primary and secondary windings, d_{HV}, shows to have the least influence (at least 2 order of magnitudes) on the resistance factor of the primary windings portion, causing it to be excluded from pseudo-empirical derivation process, thus avoiding the number of required FEM simulations to be multiplied in the next section. It should be mentioned that all the FEM simulations

Table 2.2: Generic parameters with corresponding range of variation.

	Definition	Min	Step size	Max	Number of steps
X_1 :	$\frac{d}{\delta}$	0.5	0.5	6	12
X_2 :	$\frac{h_c-2b}{hc}$	0.2	0.2	1	5
X_3 :	$\frac{a}{hc}$	0.02	0.04	0.18	5
X_4 :	m	1	1	9	9
X_5 :	$\frac{d_1}{hc}$	0.01	0.01	0.05	5

in this part, have been performed at 2 kHz and $h_c = 100$ mm, therefore the values presented in Table 2.1 can change at other frequencies and window heights, however, this will not alter the effectiveness sequence of the studied parameters.

2.3.2 Generic Parameters and the Domain of Validity

After determining the influencing variables, in order to have a generalized model, it is necessary to compound the selected variables to create dimensionless variables like the penetration ratio variable introduced by Dowell [18] as the ratio between the thickness of the conductor to its skin depth at each particular frequency. A proper range of variation is then defined for each of the selected variables, resulting in thousands of 2-D finite element simulations which covers a wide range of transformers in terms of its dimensions, operating point and application.

The number of layers, m, is dimensionless by itself, hence it needs no modification to be one of the generic parameters. The frequency of the applied current is another non-geometrical variable, affecting the winding loss, which is classically addressed by its corresponding skin depth [18]. In this fashion, the skin depth (frequency), together with the foil thickness, can form the second dimensionless variable to be used later in the regression process. Similarly, the other geometrical variables, d_1, a and b, are normalised to the window height, h_c, resulting in total 5 distinct generic parameters. The definition of the generic variables, X_1 to X_5 and the corresponding range of variations are given in Table. 2.2.

As shown in Table. 2.2, the parameter X_1 is assigned to sweep from 0.5 to 6 (12 values) which is achieved by altering the foil thickness while the frequency and consequently the skin depth, δ is fixed. Likewise, X_2, X_3 and X_5 adopted 5 different values by varying b, a and d_1, respectively, in which the transformer window height, h_c was assumed to be fixed. Covering these range of variations requires 1500 distinct 2-D FEM simulations for each number of turns at the primary side, resulting in 12300 FEM simulations in total, since the number of layers at the primary side, m, increased up to 9 layers. However, the first 5 layers is considered for the primary

regression process (6300 simulations), and another 4 layers gradually supplied to the derivation process at the secondary regression process (model extension), resulting in an extra 6000 simulations.

Not being limited to a specific dimension of a transformer or certain range of frequency is the most important advantage of introducing the generic parameters. Besides, the assigned range of variation for each parameter, covers not only most of the available transformer window arrangements used in different practical applications [9, 41], but also extreme conditions such as $X_1 \geqslant 3$ or $X_2 \leqslant 0.5$ which are basically more than sufficient.

2.3.3 Multi-Variable Regression Strategy

The proposed primary regression process comprises four steps as follows.

2.3.3.1 Structure Selection

The most important step is to identify the main format of the formula since the nature of the resistance factor is strongly nonlinear and unpredictable, particularly when the edge effect is taken into account, for this reason, it is hardly possible to propose one specific format for the final expression. For these reasons, four different structures have been considered as the candidate formats as follows.

- Polynomial structure comprising five independent variable with degree of 2 to maximum 6 as

$$\sum_{i=0}^{5}\sum_{j\geq i}^{5}\sum_{m\geq j}^{5}\sum_{n\geq m}^{5}\sum_{s\geq n}^{5}\sum_{t\geq s}^{5} P_{ijmnst}.X_i.X_j.X_m.X_n.X_s.X_t \tag{2.12}$$

  However, the structure shown in (2.12) is for the maximum degree of 6, the parameter $1 \leqslant k_1 \leqslant 6$, specifying the maximum degree of the polynomial expression, will later be used in the primary regression process to achieve the least regression error without unnecessary increasing the number of the coefficients.

- Exponential structure comprising $(X_1.X_2)$ as exponent and the second order polynomial with maximum degree of 6 for the coefficients as

$$\sum_{m=1}^{k_2}\sum_{i=0}^{5}\sum_{j\geq i}^{5} P_{ijm}.X_i.X_j.e^{-(X_1.X_2)^m} \tag{2.13}$$

  where the free variable k_2 is the maximum degree of the exponent while the maximum degree of the coefficient is 2.

- Bessel expression consisting of $(X_1.X_2)$ arguments and polynomial coefficients as

$$\sum_{m=1}^{k_3}\sum_{n=1}^{k_4}\sum_{i=0}^{5}\sum_{j\geq i}^{5} P_{ijmn}.X_i.X_j.[J_1((X_1.X_2)^m) + J_2((X_1.X_2)^n)] \tag{2.14}$$

  where J_1 and J_2 are the first and second order of the bessel function of the first kind, respectively. Also k_3 and k_4 are the maximum degree of the bessel's arguments varying at the primary regression process to fulfill the accuracy requirements.

- Rational terms which was not initially considered in our regression process, however a limited format of rational terms as (2.15) was finally utilised to adjust the accuracy of the pseudo-empirical expression.

$$\sum_{i=1}^{k_5} P_i \frac{X_4^2}{(X_1.X_2)^i} \tag{2.15}$$

  where k_5 is the maximum allowed degree of the denominator's exponent.

It should be noted that the variables k_1 to k_5 will later be used in the regression strategy section to tune the final pseudo-empirical expression with respect to the precision requirements and X_0 is assumed to be 0 in all of the structure candidates.

2.3.3.2 Database Collection

Determining five independent generic parameters shown in Table. 2.2, one can depict 6300 distinct winding arrangement of the geometry shown in Fig. 2.8 for $1 \leqslant X_4 \leqslant 5$ required for the primary regression process. The AC resistance factor of the primary windings, RF, have then been extracted by performing 6300 2D FEM simulations, resulting in a huge database comprising of 6300 elements, each consisting of 5 independent inputs, X_1 to X_5, and the corresponding RF as the output. It should be noted that the core is considered to be with no air gap and with a very high permeability, around 20000.

2.3.3.3 Primary Regression Process

After obtaining the resistance factors, corresponding to each set of generic variables, from the FEM simulations, the aforementioned alternatives structures need to be fitted in the database of 6300 resistance factors to get the final expression as a function of X_1 to X_5. The least square regression is selected as the regression method, applied on different structures while the free parameters k_1 to k_5 takes

Table 2.3: AUD, maximum overestimation and underestimation.

	Polynoimial	Bessel	Compound	Separated Comp
$AUD:$	2.89%	73.24%	0.65%	0.51%
$MaxOver:$	25%	353%	16.8%	9.06%
$MaxUnder:$	-29%	-214.3%	-20.6%	-6.15%

different values to fulfill the precision requirements. The approach, whereby the free parameters can be determined are explained in several steps as follows.

First, the regression accuracy requirements should be defined. As can be seen in Fig. 2.7, the average unsigned deviation (AUD) of the calculated RF from the simulated one is defined to be less than 1 %. This criteria is considered as the main precision indicator of the pseudo-empirical formula, however to prevent extreme sectional error, it is necessary to restrict the maximum allowed deviation of simulated points, hence, maximum 15 % deviation is defined as the second regression criteria applied on all studied arrangements of the generic variables.

Defining the regression accuracy criteria, the least square regression has been exclusively applied on each structure when k_1 to k_5 varied from 1 to 6. It was found that none of the aforementioned structures can meet the regression requirements even with the maximum defined k. For instance, for the polynomial structure given in (2.12) at the maximum allowed degree ($k_1 = 6$), AUD was 2.89 % and the maximum underestimation and overestimation were -29% and 25%, respectively, which exceeds the regression criteria, nevertheless it showed the highest accuracy among the studied structures. On the other hand, the bessel structure seems to be the worst proposed structure, between studied ones, showing the highest AUD, maximum underestimation and overestimation of 73.24%, -214.3% and %353, respectively, hence it is excluded from further regression process comprising combined structures.

Since each of the proposed structures has failed to fulfill the regression requirements, a compound format comprising two or three of the mentioned structures is taken into account with the priority for the polynomial structure which demonstrated the highest accuracy among others. It should be noted that the generic variable X_5 which indicates the normalized value of the insulation distance between the primary foils is assumed to be 0 for $X_4 = 1$ where there is only one layer of conductors. Considering the compound structure, the accuracy of the pseudo-empirical expression significantly improved. For example, by compounding all the structure, polynomial, exponential and rational, with the highest allowed degree of coefficients and exponents ($k_1, k_2, k_5 = 6$), AUD dropped to 0.65% which is far below the defined criteria, however the maximum overestimation and underestimations were 16.8% and -20.6% which are slightly higher than the defined requirements. It was noticed that most of the extreme deviations belongs to the set of data in which

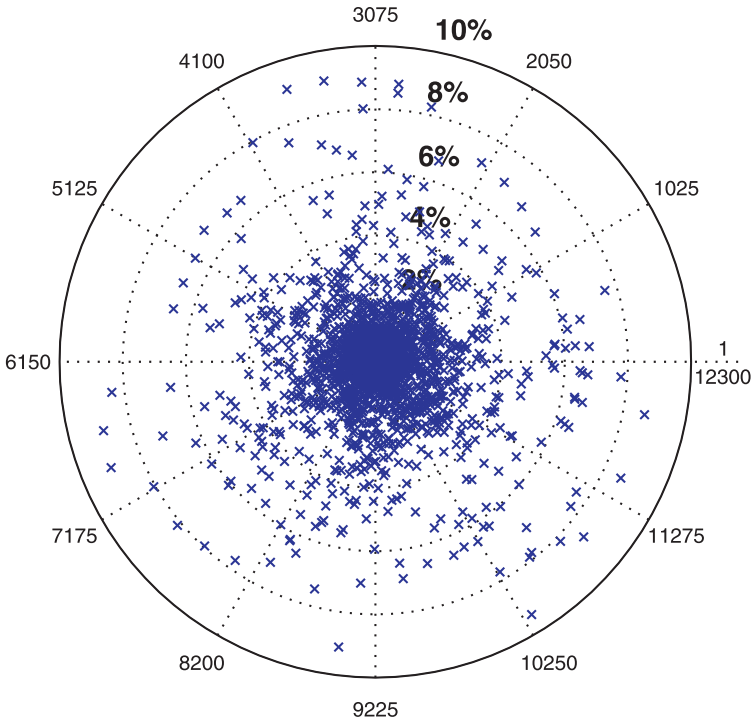

Figure 2.9: Accuracy overview of the pseudo-empirical expression.

$X_4 = 1$, therefore, it is decided to separately derive an expression for the case in which $X_4 = 1$, and to form a conditional pseudo-empirical expression. Accordingly the final pseudo-empirical expression for the multi-layer windings($X_4 > 1$) is

$$\begin{aligned} RF &= f(X_1, X_2, X_3, X_4, X_5) \\ &= \sum_{i=0}^{5} \sum_{j \geq i}^{5} \sum_{m \geq j}^{5} \sum_{n \geq m}^{5} \sum_{s \geq n}^{5} \sum_{t \geq s}^{5} P_{ijmnst}.X_i.X_j.X_m.X_n.X_s.X_t \\ &+ \sum_{m=1}^{3} \sum_{i=0}^{5} \sum_{j \geq i}^{5} P_{ijm}.X_i.X_j.e^{-(X_1.X_2)^m} + \sum_{i=1}^{5} P_i \frac{X_4^2}{(X_1.X_2)^i} \end{aligned} \tag{2.16}$$

whereas for the single-layer configuration ($X_4 = 1$), the AC resistance factor can be calculated from

$$\begin{aligned} RF &= f(X_1, X_2, X_3, X_4) \\ &= \sum_{i=0}^{3} \sum_{j \geq i}^{3} \sum_{m \geq j}^{3} \sum_{n \geq m}^{3} \sum_{s \geq n}^{3} P_{ijmns}.X_i.X_j.X_m.X_n.X_s \end{aligned} \tag{2.17}$$

where the AC resistance factors defined as a polynomial with the maximum degree of 5 for winding portions comprising only one layer of conductors; and a combination of polynomial, exponential and rational structures with $k_1 = 6$, $k_2 = 3$ and $k_5 = 5$, respectively, were derived for winding portions consisting of more than one layer. As a result, not only the maximum deviations dropped to -6.15% and 9.06% for underestimation and overestimation, respectively, but also AUD slightingly improved (0.51%) which are far below the regression requirements.

2.3.3.4 Secondary Regression Process (Model Extension)

In this section the secondary regression has been performed on (5.38) in order to investigate the validity of the expression for winding portions consisting of higher number of layers. Therefore, as shown in Fig. 2.7, the accuracy of the proposed structure has been examined in a closed loop when the number of layers, X_4 is increasing until the obtained expression fulfills the new criteria. These criteria were defined as

$$\frac{\sum_{i=1}^{300+1500(X_4^{max}-1)} \left(RF^i_{Pseudo} - RF^i_{FEM}\right)}{300 + 1500(X_4^{max} - 1)} \times 100 \leqslant 1\% \tag{2.18}$$

$$\frac{\left|P^*_{ijmnst} - P_{ijmnst}\right|}{P_{ijmnst}} \times 100 \leqslant 0.1\% \tag{2.19}$$

where (2.18) is the definition of AUD, RF^i_{Pseudo} is the resistance factor calculated by (5.38). The second criterion, shown in (2.19), is a rigourous demand of having changes of below 0.1% for any coefficients in (5.38) compared to the corresponding coefficient obtained from the previous regression with lower number of layers. This approach resulted in adding the number of layers in four steps up to $X_4 = 9$, requiring another 6000 FEM simulations to be solved. On the basis of these strict criteria, resulting in slight changes in the coefficients (P_{ijmnst}), it can be deduced that within the validity domain demonstrated in Table. 2.2, the pseudo-empirical formula derived in (5.38) is generally valid for any number of layers with a negligible impact on its accuracy.

Fig. 2.9 illustrates an overview of the residual deviation of the resistance factors, calculated by (5.38), compared to the corresponding resistance factors obtained from the FEM analysis as

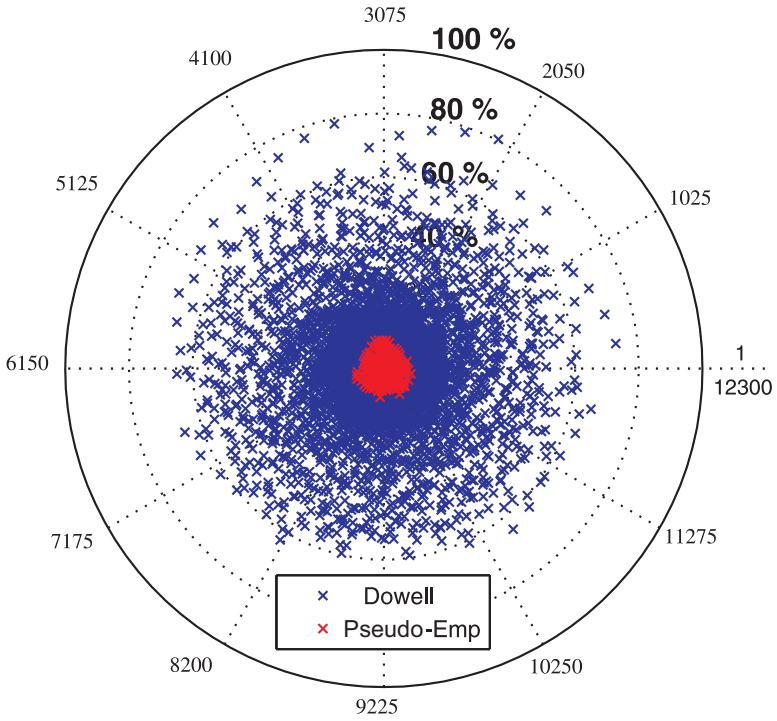

Figure 2.10: A comparative accuracy overview between the pseudo-empirical (red) and Dowell's (blue) model.

$$UD^i\% = \frac{RF^i_{Pseudo} - RF^i_{FEM}}{RF^i_{FEM}} \times 100 \tag{2.20}$$

In(2.20), UD^i accounts for the percentage of the unsigned difference between the resistance factors obtained from (5.38) and the corresponding RF extracted from FEM simulations for i th case-study where i, shown on the circumference of Fig. 2.9, varies between 1 to 12300. Hence, each blue cross located in Fig. 2.9 represents a distinct winding transformer arrangement examined in the regression process, whereby, the further each point is located from the center, the higher deviation from FEM result it suffers. The accuracy overview shown in Fig. 2.9 indicates that more than approximately 99% of the studied cases are located within the area in which UD is less than 1%.

Fig. 2.10 illustrates a comparative overview between Dowell (blue) and the pseudo-empirical formula's (red) accuracy in the whole range of validity determined in table. 2.2(each points corresponds to one unique simulation). The overall results indicate a substantial improvement of pseudo-empirical over Dowell's model, for example in some cases Dowell underestimate the RF up to 80% whereas the

maximum deviation of pseudo-empirical's expression is only 9.06% for the extreme cases. The AUD as the most informative comparison indicator between two expression, demonstrates the value of 0.51% for pseudo-empirical whereas the AUD of Dowell's expression shows a fairly high value of 24.31% over the studied points. In addition, Dowell's extreme deviation is in the range of 80% causing a substantially unreliable magnetic design. This attribute can clearly be seen in Fig. 2.10 while the pseudo-empirical expression's extreme deviations (red crosses) are confined within 9%. Apart from the extreme cases (low values of X_2, high values of X_1 and so on) in which the pseudo-empirical formula deviation is fairly negligible compared to Dowell's expression. In normal cases where Dowell is commonly considered accurate, the pseudo empirical formula shows even more accurate results than what Dowell does. To be more specific, the pseudo-empirical UD is generally less than 0.2% for the normal cases while UD of up to 10% is normally considered accurate for Dowell's expression.

Fig. 2.11 demonstrates a more specific presentation of the resistance factors obtained from (5.38), (2.2) and the FEM simulation in order to examine the applicability of each method. The AC resistance factors have been calculated versus the generic parameter, X_2, at four different combinations of X_2 and X_4 as shown in Fig. 2.11. The dimensions of the investigated transformers is significantly larger than the dimensions of the 12300 transformers used in the regression process in order to examine the validity of the initial claim regarding the generality of the pseudo-empirical expression based on the dimensionless generic parameters. As clearly can be seen in all of the graphs in Fig. 2.11, the pseudo-empirical expression almost coincides with the FEM results, confirming the general applicability of the pseudo-empirical model within the domain of validity determined in Table 2.2, whereas Dowell demonstrates a relatively large difference from FEM. This attribute can be clearly seen in Fig. 2.11(a) and (b) in which Dowell's expression significantly underestimates the actual resistance factor, e.g. with the exception of Fig. 2.11(d), in which Dowell's RF enhanced with a higher rate (because (2.2) is proportional to the square of the m), the results obtained by (2.2) are generally inaccurate at $X_2 \leq 0.6$.

2.3.4 Accuracy Investigation for Round Conductors

Despite the fact that this study was primarily concerned with deriving an analytical tool to accurately evaluate the AC resistance factor in foil conductors, it is possible to extend the applicability of the pseudo-empirical expression into solid round conductors as well by modifying some of the generic parameters used in foil analysis as

$$X_2 = \frac{N.d_r}{h_c} \tag{2.21}$$

$$X_1 = \frac{d_r\sqrt{\pi}}{2\delta}.\sqrt{X_2} \tag{2.22}$$

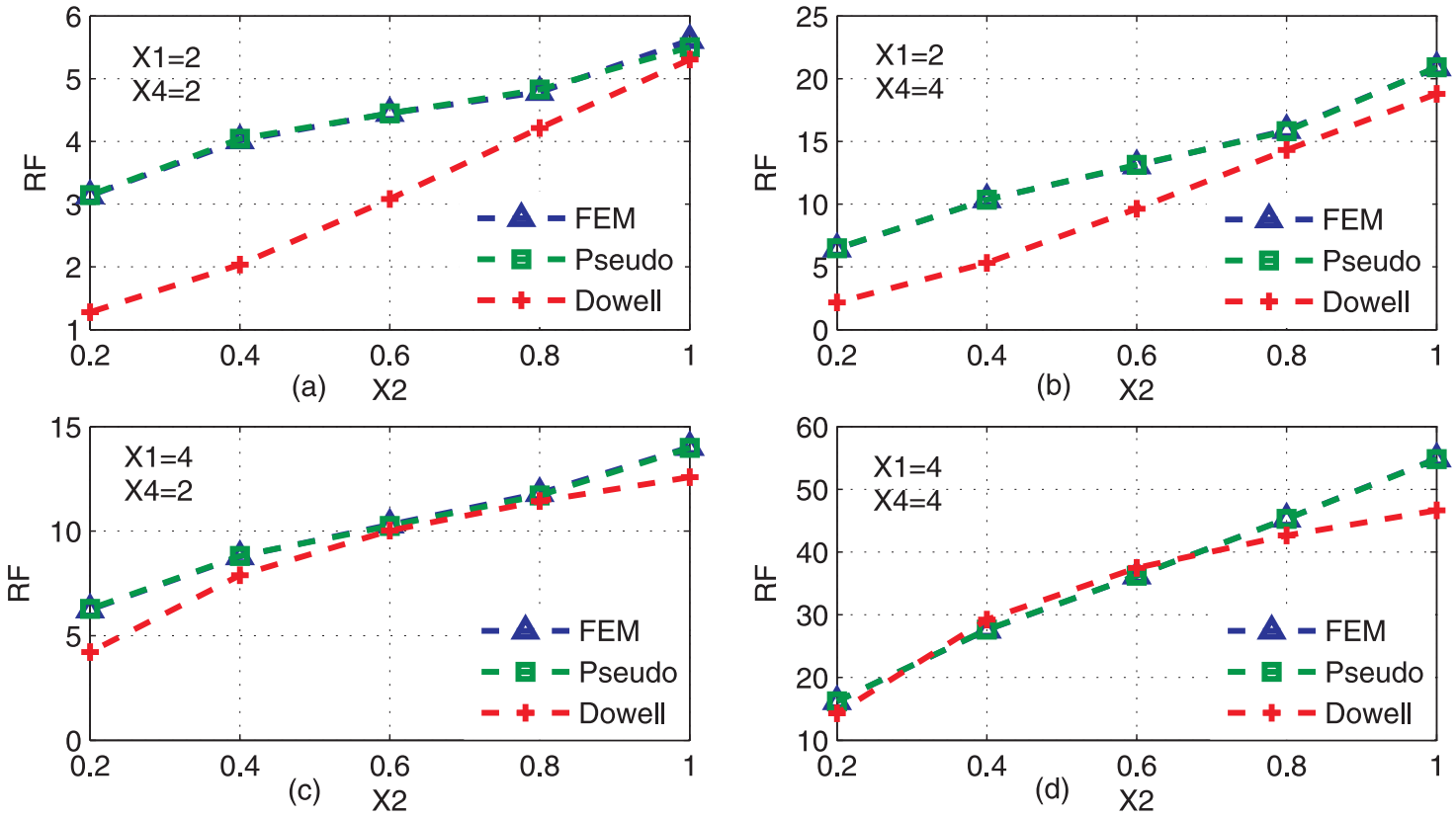

Figure 2.11: Comparison between obtained AC resistance factor, RF, versus X_2 by FEM simulations, pseudo-empirical formula and Dowell's expression. (a) $X_1 = 2$, $X_4 = 2$. (b) $X_1 = 2$, $X_4 = 4$. (c) $X_1 = 4$, $X_4 = 2$. (d) $X_1 = 4$, $X_4 = 4$.

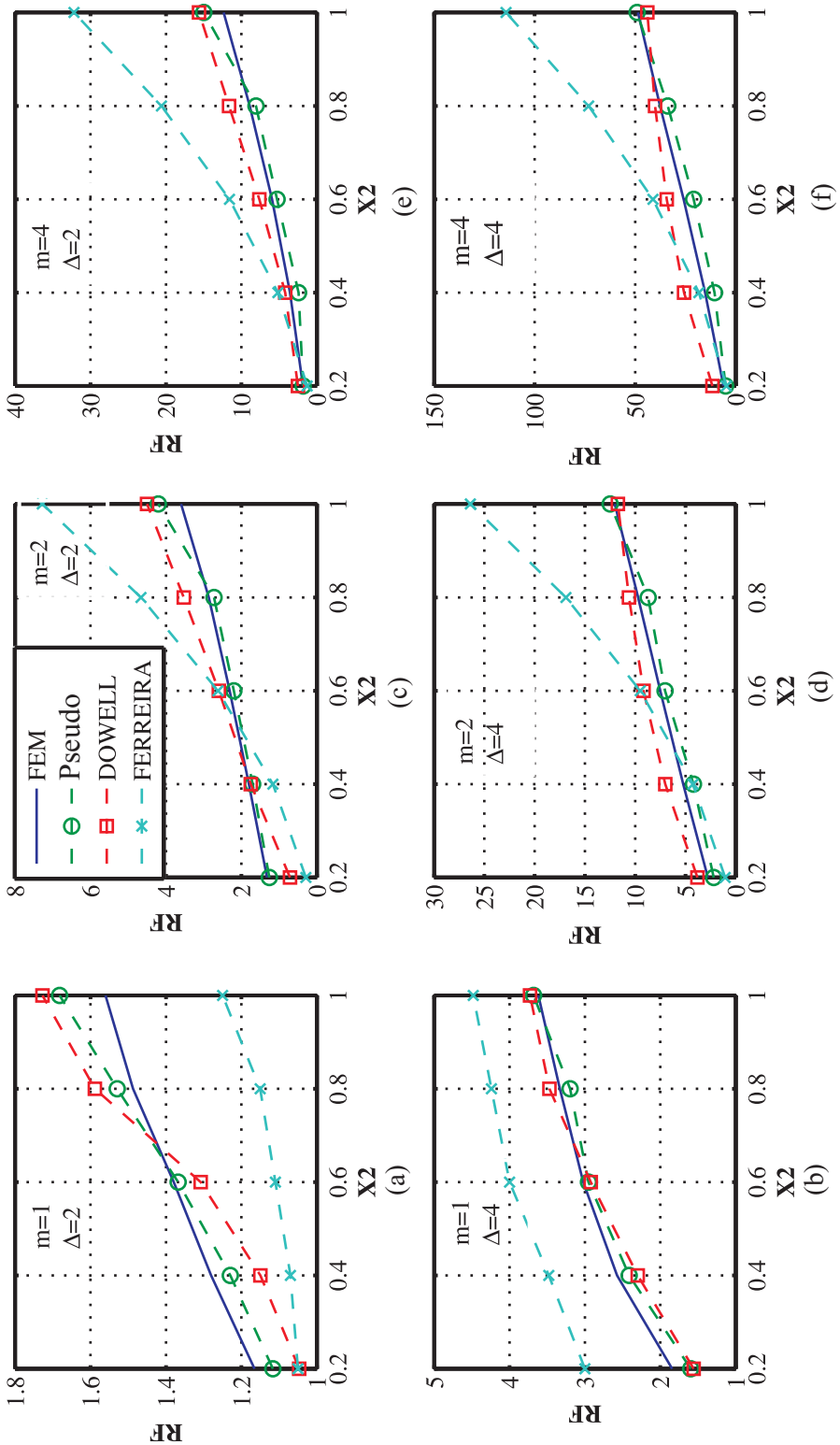

Figure 2.12: Comparison between obtained AC resistance factor, RF, versus X_2 by FEM simulations, pseudo-empirical formula, Dowell and Ferreira's expression. (a) $m = 1$, $\Delta = 2$. (b) $m = 1$, $\Delta = 4$. (c) $m = 2$, $\Delta = 2$. (d) $m = 2$, $\Delta = 4$. (e) $m = 4$, $\Delta = 2$. (f) $m = 4$, $\Delta = 4$.

where d_r is the diameter of the solid round conductor and N is the number of turns per layer. The other generic parameters (X_3 to X_5), as well as the domain of validity of all the generic parameters is the same as for foil conductors. To investigate the validity of the proposed pseudo-empirical expression for round wires, a comparative analysis between obtained resistance factors from FEM simulations, pseudo-empirical, Dowell and Ferreira's expression have been conducted versus the generic parameter X_2, varying from 0.2 to 1, at 6 distinct combination of m and Δ indicated in Fig. 2.12.

As can be seen in Fig. 2.12(a) to (f), using the modified pseudo-empirical formula, almost in the whole X_2 range considered, the AC resistance factors were calculated with a negligible difference towards the FEM results indicating the high accuracy of the proposed method even for round conductors. In contrast, Ferreira's formula generally shows a high inaccuracy for almost the whole range of X_2 and all studied combination of m and Δ particularly for $X_2 > 0.7$ (as in most of the transformers). Furthermore, the results indicate an acceptable accuracy for Dowell's expression in particular for $\Delta \leqslant 2$ and $X_2 > 0.6$ which are the case for most of the practical transformers. According to the graphs illustrated in Fig. 2.12, Dowell's expression leads to deviations of always less than 20% whereas the pseudo-empirical formula exhibit a deviation of always less than 10% within the studied range.

2.3.5 Accuracy Investigation for Interleaved Winding

Interleaving is one of the strategies to reduce the magnetic field within the transformer window and accordingly reducing the leakage inductance of the transformer, as well as AC winding loss. Fig. 2.13(a) to (d) demonstrates different interleaving arrangements of a transformer consisting of four layers of primary and four layers of secondary with six turns of round wires in each layer. The current density inside the primary windings as well as the magnetic flux intensity vectors between the windings have been shown in top parts of Fig. 2.13(a) to (d) while the low frequency magnetic field distribution inside the transformer window illustrated right beneath of the corresponding interleaved arrangement. As can be seen in Fig. 2.13(b) by sandwiching the secondary between the primary windings the peak value of the magnetic field has been reduced to half of the one in Fig. 2.13(a). In Fig. 2.13(c) an uniform interleaved arrangement with four winding sections has been shown resulting in similar magnetic field pattern as in Fig. 2.13(b) but with uniform direction while the magnetic field vectors in Fig. 2.13(b)have opposite directions inside the window. The last considered interleaved arrangement is depicted in Fig. 2.13(d) where the windings are divided to five sections while one forth of the primary windings are located at both sides. This structure results in four times less magnetic field peak value compared to the one in Fig. 2.13(a).

The obtained AC resistance factor of each arrangement by FEM simulations is

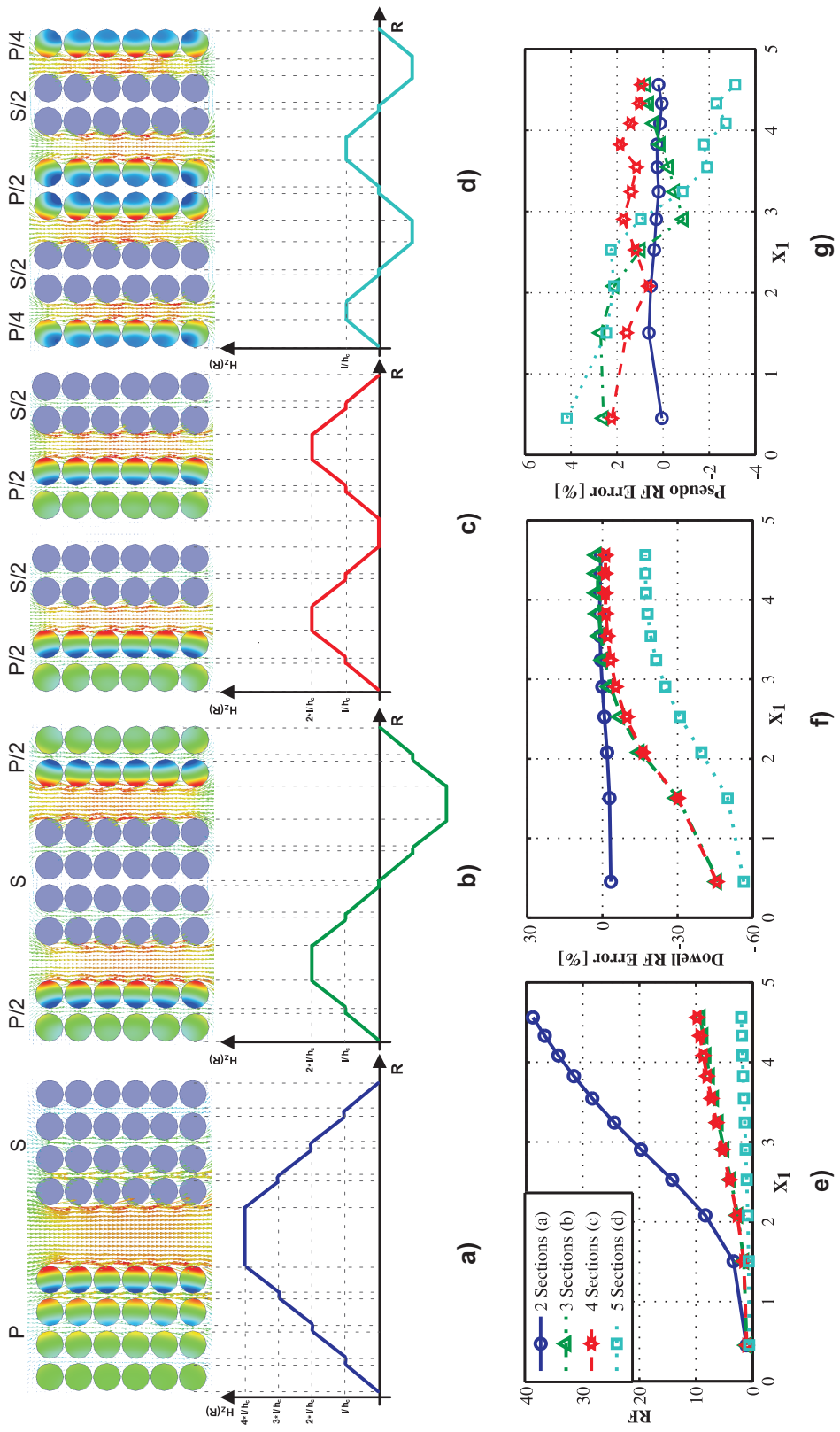

Figure 2.13: Current density and magnetic field intensity of the interleaved winding arrangements with (a) 2 sections, (b) 3 sections, (c) 4 sections, (d) 5 sections. (e) Comparison of the RF between different interleaved structures, (f) Accuracy of the Dowell's expression, (g) Accuracy of the Pseudo-Empirical's expression.

illustrated in Fig. 2.13(e) over a wide range of frequencies (X_1), indicating a substantial reduction of the RF value in the interleaved arrangements, Fig. 2.13(b) to (d), compared to the one without interleaving,Fig. 2.13(a). It is interesting to point out that the RF values of the arrangement (b) and (c) are almost the same (about 4 times less than the one without interleaving), although the one in Fig. 2.13(c) consists of more sections which is more complex to be wound. In principle, the arrangement in Fig. 2.13(b) has more advantages over others since the RF value and accordingly its AC winding loss is substantially reduced while the secondary windings are not separated. In particular, this feature is more important when the secondary windings has higher voltages resulting in excess inter-winding capacitances if the high voltage windings is separated.

Fig. 2.13(f) and (g) show the Dowell and Pseudo RF error calculated by (2.6) and (2.23), respectively, over a wide range of frequency (X_1).

$$RF_{Error}\,[\%] = 100 \times \frac{RF_{Pseudo} - RF_{FEM}}{RF_{FEM}} \tag{2.23}$$

As can be seen in Fig. 2.13(f), Dowell expression is only accurate for the non-interleaved case and it shows up to 50% underestimation for the interleaved cases while the deviation of the Pseudo-Empirical's formula is within 4%.

2.4 Experimental Validation

In order to verify the accuracy of the proposed pseudo-empirical equation, three transformers, comprising ETD59 ferrite cores, two layers of foil conductors as the primary windings and one layer of soild round wire as the secondary winding, with distinct porosity factors have been manufactured. The thickness of the primary foil conductors is 0.5 mm with different heights for each transformers to achieve the porosity factor or X_2 of 0.92, 0.8 and one extreme case with $X_2 = 0.4$, while the secondary windings of all the three transformers have been consisted of 37 turns of magnet wire with 1 mm diameter in 1 layer. Other dimensional parameters which have been kept identical in all the transformers are $h_c = 45$ mm, $a = 1.75$ mm, $b = 1.8$, $d_1 = 1$ mm and $d_{HV} = 2$ mm while the parameter b differs at each transformer as follows: $b = 1.8$, 4.5 and 13.5 mm corresponding to $X_2 = 0.92$, 0.8 and 0.4, respectively.

Using the network analyser, Bode 100, the impedance of the transformers have been measured from the primary side while the secondary was shorted over a wide range of frequency from 10 kHz to 300 kHz to ensure that the generic parameter X_1 to be swept from about 0.75 to as high as 4.3 which is sufficiently high. The measurement setup and the manufactured transformers are shown in Fig. 2.14.

Fig. 2.15 demonstrates a comparison between the measured resistance and the calculated value by Dowell and pseudo's expression versus frequency at three differ-

ent values for X_2. The noisy measurement data can be attributed to the extremely low resistance of the manufactured transformers which is in the range of some milliohms. The overall results indicate that the pseudo's expression is in good agreement with the experimental results, confirming the accuracy of the proposed method over a wide range where Dowell's expression significantly underestimates the AC resistance value. This attribute is clearly demonstrated in Fig. 2.15 particularly at lower values of X_2 where the second component of the magnetic field within the transformer window is intensified or at higher values of X_1 where the skin depth is substantially low.

2.5 Conclusions

The objective of this chapter was primarily to introduce a novel analytical expression to precisely calculate the AC resistance factor of high power-density magnetic components in which precise loss evaluation is the key for designing and implementing a proper thermal management scheme. Hence, a so called pseudo-empirical expression has been derived from a rigourous regression algorithm based on an extensive 2D finite element simulation scenario, resulting in an accurate analytical expression with an average unsigned deviation of 0.51% and the extreme deviations of not higher than 9%. This high accuracy together with its wide range of applicability, taking into account any number of layers, a wide range of penetration ratio, porosity factors, and position of the windings in the transformer window, make the pseudo-empirical expression a useful tool for designers and researchers to easily implement it within any optimization loops with no accuracy compromise.

Moreover, using 2D FEM analysis, a critical review taking the two dimensional edge effect into account has been carried out on the previous well-known models in the AC winding loss calculation in order to determine their corresponding domain of validity in which those models provide an acceptable accuracy, resulting in a set of useful guidelines while using the aforementioned analytical models.

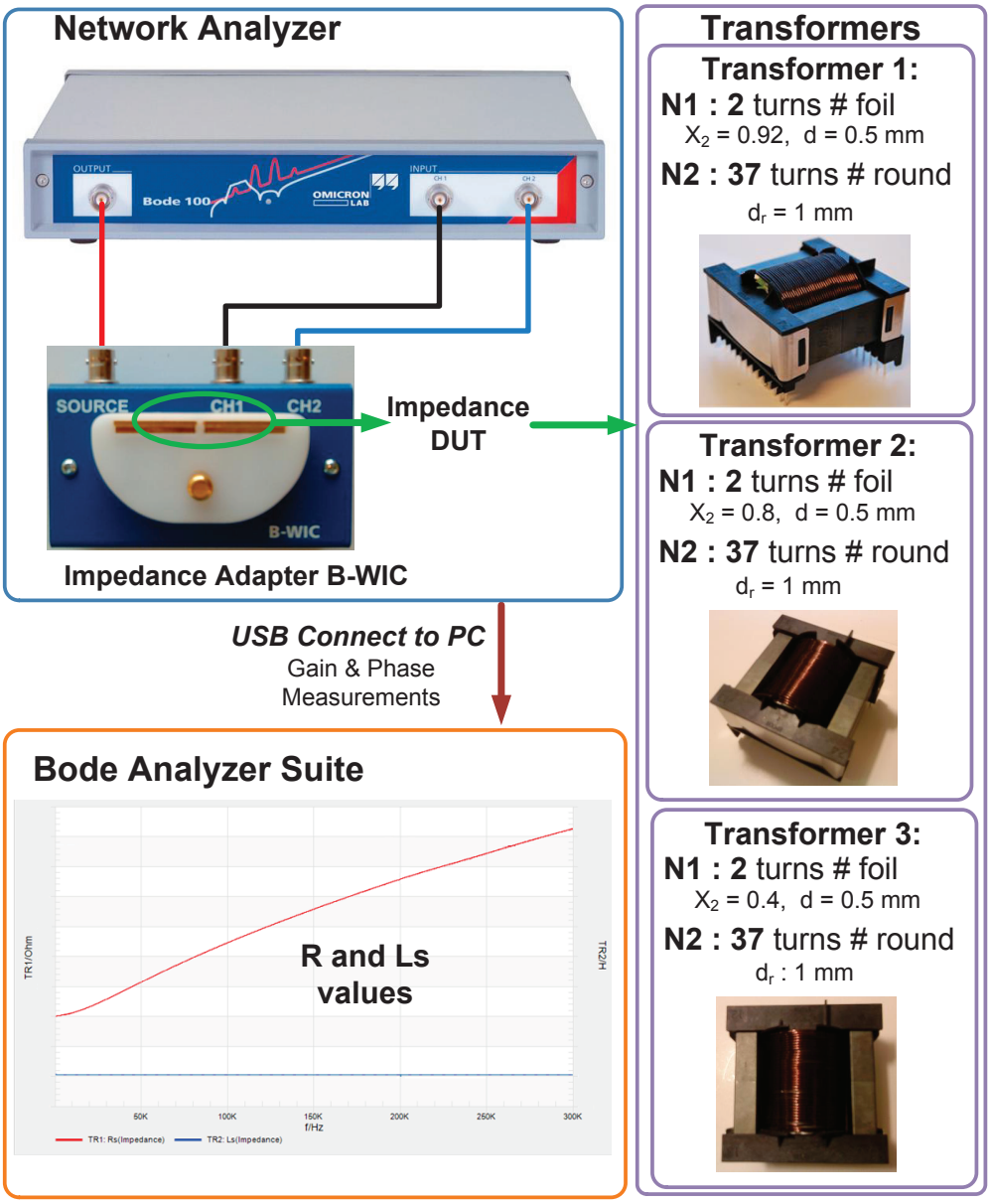

Figure 2.14: Measurement setup and the manufactured transformers.

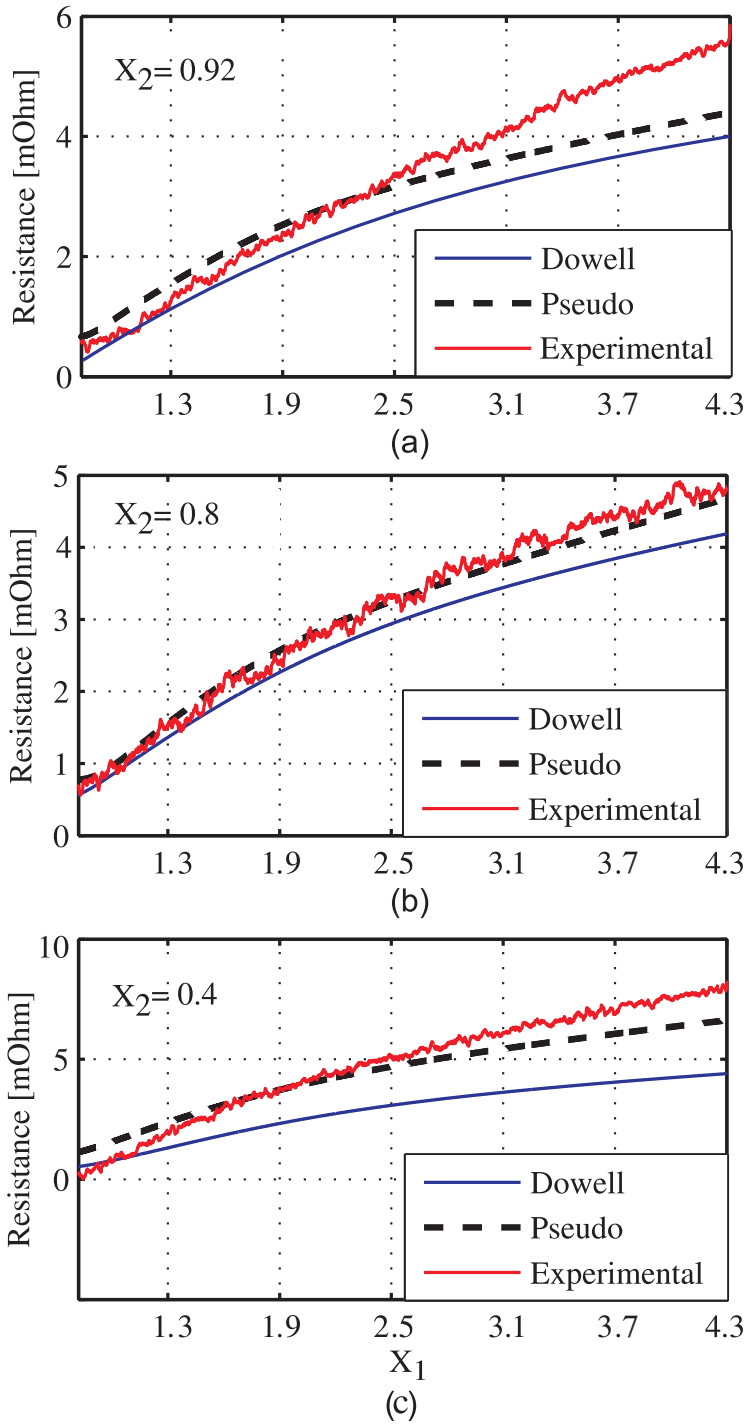

Figure 2.15: Comparison between the measured resistance and the calculated value by Dowell and Pseudo's expression versus frequency.

Chapter 3

Leakage Inductance

3.1 Introduction

Recently, there has been growing interest in utilising dual active bridge (DAB) converters in high power applications. The equivalent circuit of a DAB converter is shown in Fig. 3.1 in which two square voltage waveforms on two sides of the transformer has been shifted by controlling the input and output bridges, applying full voltage on the inductance, L_σ, which is used to shape the current as a power transfer element [44]. In order to achieve zero voltage switching (ZVS), the phase shift between the bridges, φ , should be higher than a certain value resulting in the minimum value of the series inductance as presented in (5.49). This inductance is often integrated in the high frequency transformer, Fig. 3.1, in order to reduce the number of components, hence achieving higher power densities.

$$L_\sigma = \frac{V_{DC_1} V_{DC_2} \varphi \cdot (\pi - \varphi)}{2 P_{out} \pi^2 f_s n} \tag{3.1}$$

Apart from the DAB converter, the stored energy in the leakage inductance causes an excess switching loss due to the turn off voltage spikes in dc-dc converters. On the other hand in some applications such as resonant converters the value of the leakage inductance should be tuned in order to incorporate the leakage inductance as one of the resonant elements to retain the resonant conditions. Hence, accurate evaluation of leakage inductance in the design process is of great importance for magnetic designers, more specifically in high power density applications where high calculation deviations can not be easily tolerated.

The purpose of this chapter is to propose a new analytical model to calculate a fairly precise value of leakage inductance particularly when the converter operates at high frequencies. The model takes into account the effects of high frequency fields inside the conductors with all the geometrical parameters of the transformer windings when determining the leakage inductance. Being validated by FEM simulations

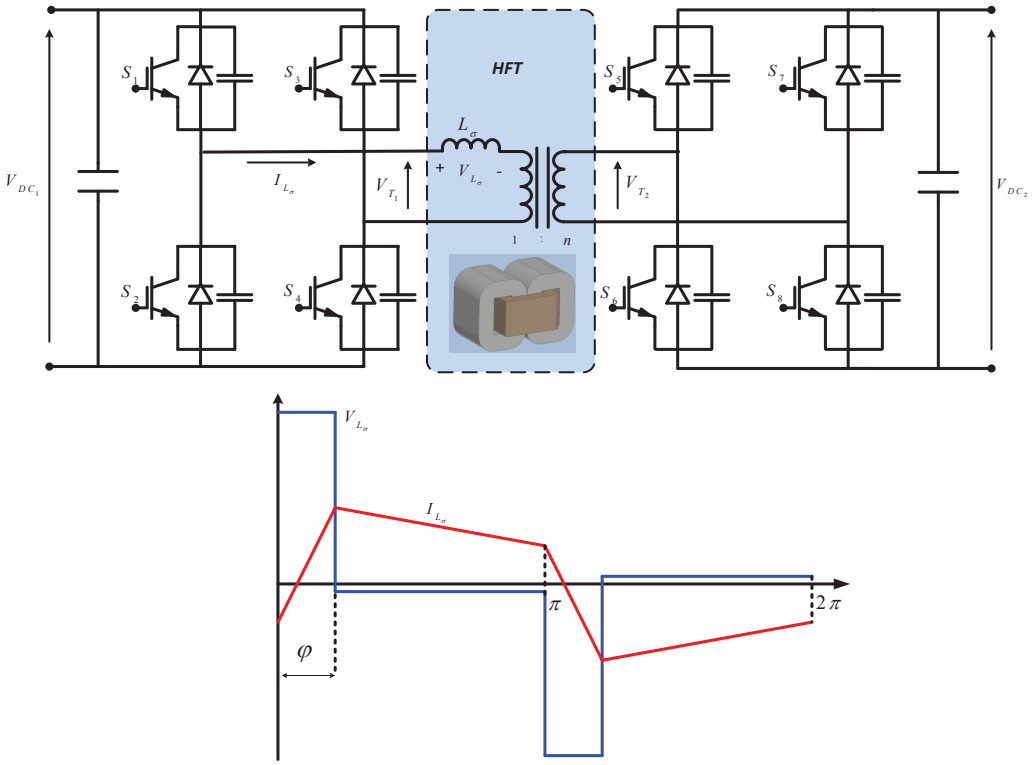

Figure 3.1: Equivalent circuit of a dual active bridge converter along with the leakage inductance integrated in to the high frequency transformer, as well as the voltage and current of the leakage inductance.

and measurements on different winding configurations, this model provides a very good accuracy with wide-range applicability which could be of interest for designers to avoid time consuming FEM simulation without compromising with the accuracy.

The first part of this chapter explains the methodology used to derive the final frequency-dependent formula. The next part provides a wide range comparison between classical methods and the new frequency-dependent expression in terms of accuracy and domain of validity. Then, the experimental results are presented and finally, Section V provides the conclusions.

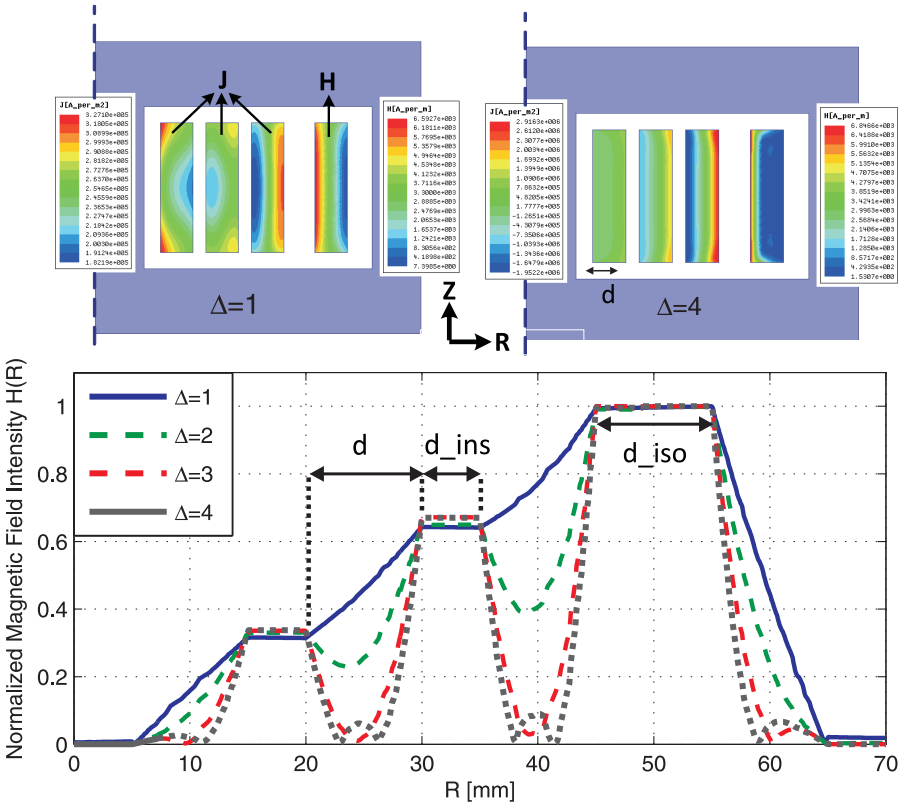

Figure 3.2: The magnetic field distribution profile within the transformer window at different frequencies.

3.2 Expression Derivation

Fig. 3.2 shows a sample 2D axisymmetric FEM simulation of the transformer windings at different values of penetration ratio, $\triangle$ as defined in (3.11), illustrating the computed current density distribution and magnetic field intensity in the primary and secondary windings respectively. The dimensions of the geometry were kept constant and different values of $\triangle$ were achieved by applying the frequencies corresponding to those values. In other words, the analysis is based on a dimensionless parameter, $\triangle$, taking into account the effects of both frequency and geometrical dimensions. The normalised magnetic field intensity distribution on inter and intra-layer spaces, obtained from the same FEM simulation at four different values of $\triangle$, are shown in Fig. 3.2 bottom.

$$\begin{aligned} W_{leakage} &= \frac{1}{2}\mu \int H^2 dv \\ &= \frac{1}{4} L_{\sigma(pri)} I_1^2 \\ &= W_{pri} + W_{ins(1)} + W_{isolation} + W_{sec} + W_{ins(2)} \end{aligned} \tag{3.2}$$

As can be seen in Fig. 3.2, the magnetic field intensity inside the copper windings drastically decrease by increasing the frequency or its corresponding $\triangle$, resulting in lower value of leakage inductances since the leakage inductance is strongly correlated to the magnetic field intensity, as in (3.2), within the transformer window. This causes higher ohmic losses on the third layer of the primary windings than the ohmic losses in the first and second layer, because of this fact that in contrast to the first layer, which does not suffer from the magnetic field on its left hand side, the second layer and more significantly the third layer suffer from the presence of the magnetic field on their left hand side. This magnetic field drop at higher frequency is often neglected in most of the classical formulas for leakage inductance calculations which might result to inaccuracy in new high power density applications.

Fig. 3.3 shows the schematic of a transformer window comprising the magnetic core with a relatively high permeability of 20000, copper foil primary windings consisting of m_1 layers and N_{l1} turns per layer, secondary round magnet wires consisting of m_2 layers and N_{l2} turns per layer and all the corresponding distances, i.e, isolation distance, insulating distance, winding heights and thicknesses and so on.

As shown in (3.2), the energy stored in the magnetic field of a transformer when the secondary windings is shorted is equal to the energy stored in the leakage inductance referred to the primary side of the transformer. Therefore, one can separately derive the stored energy within isolation distance, primary and secondary inter-layer insulations and primary and secondary copper areas, respectively. First, the energy stored within isolation and insulation distances are calculated since the magnetic field intensity within these regions are constant, hence using (3.2) and considering a one dimensional magnetic field, one can conclude:

$$\begin{aligned} W_{isolation} &= \frac{1}{4}\mu MLT_{isolation} h_w \int_0^{d_{iso}} \left(\frac{N_{l1} m_1 I_1}{h_w}\right)^2 .dx \\ &= \frac{1}{4}\mu MLT_{isolation} \frac{N_{l1}^2 m_1^2 I_1^2}{h_w} d_{iso} \end{aligned} \tag{3.3}$$

$$\begin{aligned} W_{ins1} &= \frac{1}{4}\mu MLT_{pri} h_w \left[\sum_{n=0}^{m_1-1} \frac{N_{l1}^2 n^2 I_1^2}{h_w^2} d_{ins1}\right] \\ &= \frac{1}{4}\mu MLT_{pri} \frac{N_{l1}^2}{h_w} {I_1}^2 d_{ins1} \frac{m_1(m_1-1)(2m_1-1)}{6} \end{aligned} \tag{3.4}$$

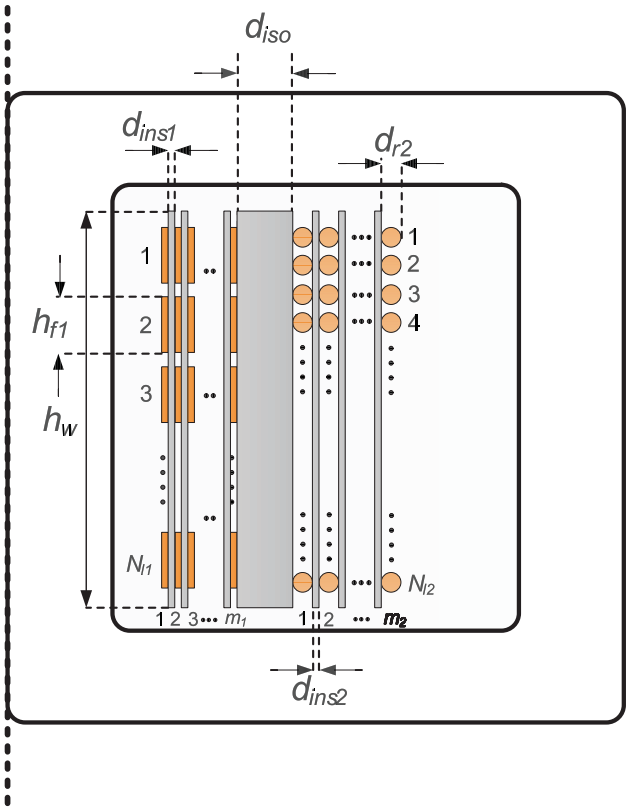

Figure 3.3: Cross-sectional view of the winding configurations according to Dowell's assumptions.

$$\begin{aligned} W_{ins2} &= \frac{1}{4}\mu MLT_{sec} h_w \left[\sum_{n=0}^{m_2-1} \frac{N_{l2}^2 n^2 I_2^2}{h_w^2} d_{ins2} \right] \\ &= \frac{1}{4}\mu MLT_{sec} \frac{N_{l1}^2}{h_w} {I_1}^2 d_{ins2} \frac{m_1^2(m_2-1)(2m_2-1)}{6m_2} \end{aligned} \tag{3.5}$$

where MLT_{pri}, MLT_{sec} and MLT_{iso} are the mean length turns of the primary portion, secondary portion and isolation distance, respectively. h_w is the winding height, I_1 and I_2 are the peak current values of primary and secondary portions, respectively.

However, obtaining a closed formula for the stored energy inside the copper windings is not as straightforward as what were obtained in (3.3) to (3.5) since the magnetic field pattern is not constant or linear at higher frequencies as already shown in Fig. 3.2. In fact, the magnetic field has a hyperbolic pattern according to Dowell's derivation [18]. Substituting this hyperbolic pattern in (3.2), one can derive:

$$W_{pri} = \frac{1}{4}\mu MLT_{pri} h_w \sum_{n=1}^{m_1} \left(\int_0^{d_{pri}} H_x^2 dx \right)$$
$$= \frac{1}{4}\mu MLT_{pri} h_w \sum_{n=1}^{m_1} \left(\int_0^{d_{pri}} \left[\frac{H_{ex} sinh(\alpha x) - H_{in} sinh(\alpha x - \alpha.d_{pri})}{sinh(\alpha.d_{pri})} \right]^2 dx \right) \quad (3.6)$$

$$W_{sec} = \frac{1}{4}\mu MLT_{sec} h_w \sum_{n=1}^{m_2} \left(\int_0^{d_{sec}} H_x^2 dx \right)$$
$$= \frac{1}{4}\mu MLT_{sec} h_w \sum_{n=1}^{m_2} \left(\int_0^{d_{sec}} \left[\frac{H_{ex} sinh(\alpha x) - H_{in} sinh(\alpha x - \alpha.d_{sec})}{sinh(\alpha.d_{sec})} \right]^2 dx \right) \quad (3.7)$$

where H_{in} and H_{ex} are the magnetic field intensity at the left and right hand side of each winding layer and can be calculated as (3.8). Also, α is defined as $\frac{1+j}{\delta}$ where δ is the skin depth at any particular frequency and d_{pri} and d_{sec} are the thickness of the primary and secondary conductors, respectively,

$$H_{in} = \frac{(n-1)N_{l1}I_1}{h_w} \qquad H_{ex} = \frac{nN_{l1}I_1}{h_w} \quad (3.8)$$

Substitution of (3.8) into (3.6) and (3.7) and rearranging for the stored energy gives

$$W_{pri} = \frac{1}{4}\mu MLT_{pri} \frac{N_{L1}^2}{h_w} m_1 I_1^2$$
$$\left[\frac{sin(\frac{2\Delta_1}{\alpha\delta}) 4\alpha\delta^2(m_1^2 - 1) + 4d_{pri}(2m_1^2 + 1) - \alpha\delta^2 sin(\frac{4\Delta_1}{\alpha\delta})(2m_1^2 + 1) + 8d_{pri}(1 - m_1^2) cos(\frac{2\Delta_1}{\alpha\delta})}{24 sin^2(\frac{2\Delta_1}{\alpha\delta}))} \right] \quad (3.9)$$

$$W_{sec} = \frac{1}{4}\mu MLT_{sec} \frac{N_{L1}^2}{h_w} \frac{m_1^2}{m_2} I_1^2$$
$$\left[\frac{sin(\frac{2\Delta_2}{\alpha\delta}) 4\alpha\delta^2(m_2^2 - 1) + 4d_{sec}(2m_2^2 + 1) - \alpha\delta^2 sin(\frac{4\Delta_2}{\alpha\delta})(2m_2^2 + 1) + 8d_{sec} \cdot (1 - m_2^2) cos(\frac{2\Delta_2}{\alpha\delta})}{24 sin^2(\frac{2\Delta_2}{\alpha\delta}))} \right] \quad (3.10)$$

where Δ_1 and Δ_2 are the penetration ratio of the primary and secondary winding as (3.11)

$$\Delta_1 = \frac{d_{pri}}{\delta} \qquad \Delta_2 = \frac{d_{sec}}{\delta} \quad (3.11)$$

Finally, substitution of (3.3), (3.4), (3.5), (3.9) and (3.10) into (3.2) and rearranging for $L_{\sigma(pri)}$ gives the final frequency-dependent expression as

$$
\begin{aligned}
L_{\sigma(pri)} = \mu \frac{N_{L1}^2}{h_w} m_1 \Bigg[& MLT_{iso} m_1 d_{iso} \\
& + MLT_{pri} \frac{(m_1 - 1).(2m_1 - 1)}{6} d_{ins1} \\
& + MLT_{sec} \frac{m_1.(m_2 - 1).(2m_2 - 1)}{6m_2} d_{ins2} \\
& + MLT_{pri} \frac{sin(\frac{2\Delta_1}{\alpha\delta}) 4\alpha\delta^2 (m_1^2 - 1) + 4d_{pri}(2m_1^2 + 1)}{24 sin^2(\frac{2\Delta_1}{\alpha\delta}))} \\
& + MLT_{pri} \frac{-\alpha\delta^2 sin(\frac{4\Delta_1}{\alpha\delta})(2m_1^2 + 1) + 8d_{pri}(1 - m_1^2) cos(\frac{2\Delta_1}{\alpha\delta})}{24 sin^2(\frac{2\Delta_1}{\alpha\delta}))} \\
& + MLT_{sec} \frac{m_1}{m_2} \frac{sin(\frac{2\Delta_2}{\alpha\delta}) 4\alpha\delta^2 (m_2^2 - 1) + 4d_{sec}(2m_2^2 + 1)}{24 sin^2(\frac{2\Delta_2}{\alpha\delta}))} \\
& + MLT_{sec} \frac{m_1}{m_2} \frac{-\alpha\delta^2 sin(\frac{4\Delta_2}{\alpha\delta})(2m_2^2 + 1) + 8d_{sec}(1 - m_2^2) cos(\frac{2\Delta_2}{\alpha\delta})}{24 sin^2(\frac{2\Delta_2}{\alpha\delta}))} \Bigg]
\end{aligned}
\tag{3.12}
$$

It should be noted that the final expression has been derived based on foil winding configuration, however, it would be applicable for round conductors by modifying Δ of the windings portion with round wire as

$$
\Delta = \frac{d_r \sqrt{2}}{2\delta} \sqrt{\frac{N_l d_r \sqrt{\pi}}{2h_w}} \tag{3.13}
$$

3.3 Accuracy Investigation

In order to investigate the accuracy of the aforementioned expression, parametric FEM simulations covering a wide range of frequency, up to 200 kHz, have been performed. The obtained leakage inductances were then compared with the leakage inductances calculated by the classical expressions [9, 41]. The investigated winding arrangement, illustrated in Fig. 3.4(a), consists of 20 foil conductors in each winding portion, 5 layers and 4 turns per layer, with the foil thickness of 1.2 mm. All the geometrical dimensions are kept constant while the operating frequency is swept from 50 Hz to 200 kHz.

$$
L_{\sigma(classic)} = \mu MLT_{pri}.\frac{m_1^2.N_{l1}^2}{h_w} \left(d_{iso} + \frac{m_1.d_{pri} + (m_1 - 1)d_{ins1} + m_2.d_{sec} + (m_2 - 1)d_{ins2}}{3} \right) \tag{3.14}
$$

As can be seen in Fig. 3.4(b), the classical expression, (3.14), generally shows a high inaccuracy for almost the whole range of investigation, particularly at higher

(a)

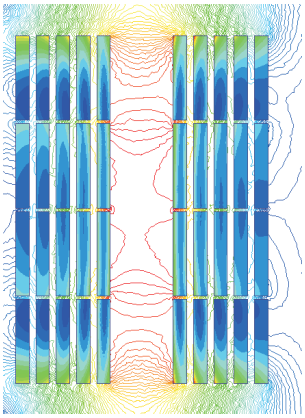

(b)

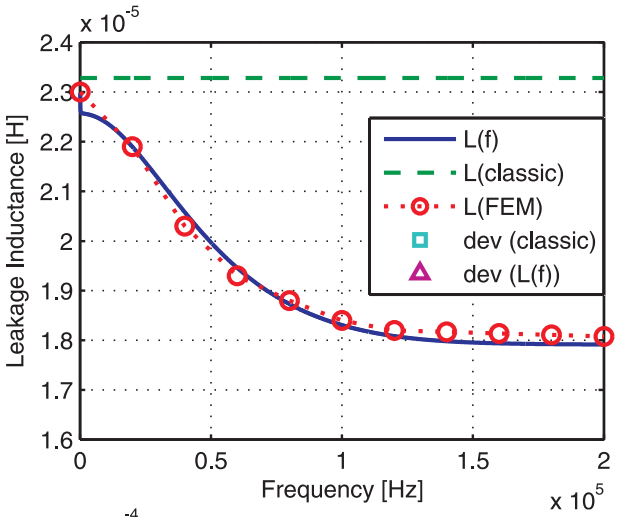

(c)

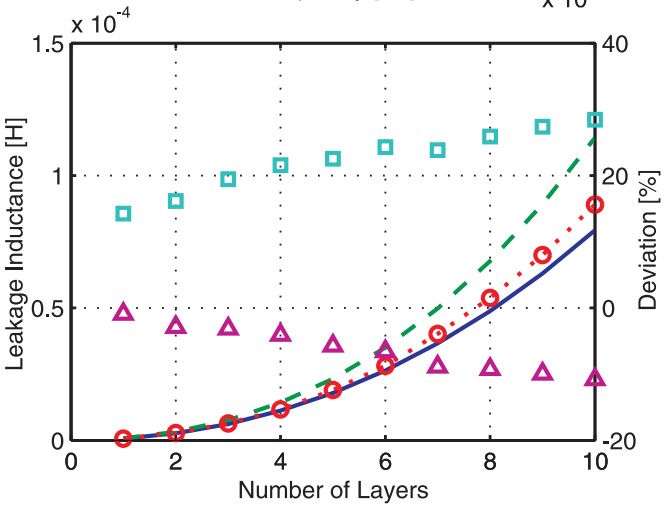

Figure 3.4: (a) A sample FEM simulation result. (b) Calculated Leakage inductance by the studied methods versus frequency. (c) Calculated Leakage inductance by the studied methods versus the number of layers in each windings portion while the frequency is constant.

frequencies. For instance, at 200 kHz, the classical expression estimates the leakage inductance as high as 0.23 μH whereas FEM simulation and the derived frequency-dependent expression shows 0.182 μH and 0.18 μH respectively. This significant overestimation can result in an unrealistic and costly magnetic design. This inaccuracy could stem from the rigourous assumption made regarding the linear pattern of the magnetic field within copper conductors which is not a valid assumption when a conductor, conducting high frequency currents, is surrounded by a large number of other conductors with a complex arrangement. In fact, by increasing the frequency, the magnetic field inside the copper conductors falls quicker towards zero, consequently the leakage inductance decreases as can be seen in Fig. 3.4(b) where results are determined by FEM and the frequency-dependent formula. Exceeding a certain frequency, depending on geometrical characteristics of the windings, there would be almost no magnetic field within a conductor and thus no further decrease in the obtained leakage inductance. This attribute can be seen in Fig. 3.4(b) when the frequency exceeds 120 kHz.

Fig. 3.4(c) shows the obtained values of leakage inductance at different number of primary and secondary winding layers whereas the frequency is kept constant at 150 kHz. Moreover the deviation of the classical and frequency-dependent expressions from the results obtained by FEM have been calculated by

$$L_{\sigma(deviation)}[\%] = 100 \times \frac{L_{\sigma(calculated)} - L_{\sigma(FEM)}}{L_{\sigma(FEM)}} \tag{3.15}$$

As can be seen in Fig. 3.4(b) and (c), using the frequency-dependent formula, almost in the whole range of frequency and at different number of winding layers, the leakage inductance were calculated with a negligible difference from the FEM results indicating the high accuracy of the proposed expression. In contrast, the classical formula generally shows a high inaccuracy for almost the whole range of frequency and different number of layers. According to the deviation curves illustrated in Fig. 3.4(c), classical expression leads to deviations of a 30% overestimation (with 10 layers of windings) whereas the frequency-dependent formula exhibit a deviation of always less than 10% underestimation, nevertheless at lower number of layers it is around 4% ,within the studied range which is substantially more accurate than the classical expression. In addition, d_{ins2} and d_{iso} are about 1 and 2 mm, respectively.

3.4 Exprimental Validation

In order to verify the accuracy of the proposed frequency dependent expression, a transformer comprising ETD59 Ferrite cores, two layers of foil conductors as the primary windings and one layer of solid round wire consisting of 37 turns as the secondary windings, has been manufactured. The thickness and diameter of the foil and round conductors are, respectively, 0.5 and 1 mm while the porosity factor, X_2

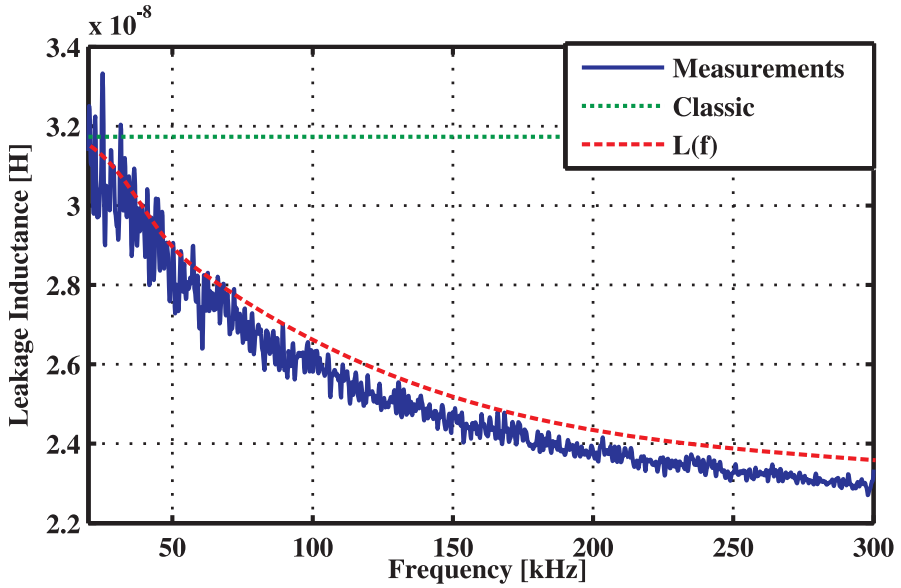

Figure 3.5: Comparison between the measured leakage inductance and the calculated values by the frequency dependent and classical expressions.

is about 0.92. Using the network analyser, Bode 100, the impedance of the transfor has been measuredfrom the primary side while the secondary is shorted.

Fig. 3.5 demonstrates a comparison between the measured leakage inductance and the values calculated by the frequency dependent and classical expressions. The overall results indicate a good agreement between the frequency dependent expression and the measurements, whereas the classical expression is constant within the whole frequency range, demonstrating about 30% overestimation of the leakage inductance.

3.5 Conclusions

The objective of this chapter was to introduce a novel analytical expression to precisely calculate the leakage inductance of high power density magnetic components in which precise loss and parasitic evaluation is the key to design of the transformer, as well as to keep the switching losses within acceptable ranges. Hence, using the energy method, a frequency-dependent expression has been derived resulting in an accurate analytical expression. This high accuracy together with its wide range of applicability, taking into account any number of layers, a wide range of penetration ratio and frequencies, and position of the windings in the transformer window with its respective dimensions, make the frequency-dependent expression a useful tool for designers and researchers to easily implement it within any optimization loops with

almost no accuracy compromise.

Chapter 4

Magnetic Core

4.1 Introduction

Estimation of the total loss is difficult in todays converters since the magnetic materials face non-sinusoidal excitations [45, 46]. In offshore wind farm, weight and size are critical parameters which have significant effect on the cost and complexity of the installation, foundation and tower. Consequently, higher frequencies are sought to be used in order to decrease the weight and size of the transformer [47]. The voltage and current waveforms in these transformers are non-sinusoidal [48]. Hence, the influence of these non-sinusoidal waveforms on the total loss should be investigated. This non-sinusoidal nature can be handled in winding loss calculation by applying the Fourier transform and superposition [49]. However, core loss evaluation, in contrast, is more difficult because of the nonlinear nature of the magnetic materials. Based on the abovementioned facts, the optimum design of a medium (high) frequency high power transformers requires an accurate investigation of magnetic losses especially for non-sinusoidal waveforms.

The other important issue in medium frequency high power transformers is the magnetic material selection. The favourable magnetic materials for magnetic components in a higher range of frequency and power are the ones with lowest core losses, higher saturation flux densities and higher continuous operating temperature [50]. All these characteristics have to be understood and taken into account in order to have a suitable selection. Among all categories of magnetic materials which are suitable for high frequency applications, ferromagnetic materials are favoured to be used in higher power density applications, due to their higher saturation flux densities than ferrites [51–53]. Particularly, amorphous and nanocrystalline materials are categorized as low loss and high saturation level ferromagnetic material [54, 55].

The aim of this chapter is to investigate the core losses in high power density transformers when subjected to non-sinusoidal waveforms, in order to evaluate the dependency of the magnetic loss on the shape of the waveform. Firstly, general

Table 4.1: Magnetic Material Characteristics

Magnetic Material Type	Material	Manuf.	B_{sat}	Specific Losses @ 0.1 T, 100 kHz	Continous Operating Temperature
Sil.Steel	10JNHF600	JFE [56]	1.87 T	0.24 kW/kg	150°C
Sil.Steel	10NEX900	JFE	1.6 T	0.19 kW/kg	150°C
Amorphous	2605SA1	Metglas [57]	1.56 T	0.2 kW/kg	150°C
Ferrite	3C85 [58]	Ferroxcube	0.45 T	0.009 kW/kg	140°C
Ferrite	3C93	Ferroxcube	0.52 T	0.009 kW/kg	140°C
Powder	Xflux 60	Magnetics [59]	1.6 T	0.26 kW/kg	200°C
Powder	KoolMu 125	Magnetics	1.05 T	0.14 kW/kg	200°C
Nano.Crys	Vitroperm500F	VAC [60]	1.2 T	0.01 kW/kg	120°C
Nano.Crys	Finement	Hitachi [61]	1.23 T	0.011 kW/kg	120°C

characteristics of different soft magnetic material are investigated. Then, three main methods of core loss evaluations are explained and finally the modified empirical expressions for switch-mode magnetics are derived and investigated over a wide range of duty cycles and rise times.

4.2 Magnetic Material Selection

One of the most important step in designing high power density transformers is most probably selecting the appropriate magnetic material. To have the best selection, the magnetic material characteristics should be studied. In reality, since there is no ideal magnetic material for high frequencies providing low losses, high saturation flux density, high permeability and low magnetostriction, one should make some compromises based on the particular application.

Magnetic materials are classified based on their magnetic properties and also applications. A soft magnetic material is a material which can be easily magnetized and demagnetized. In contrast, hard magnetic materials require essential external magnetic field for their magnetization and demagnetization. Soft magnetic materials are usually used for making transformers cores, which concentrate and shape the magnetic flux. In high frequency high power applications, there are four main parameters that should be taken into consideration

- Specific core loss or core loss density
- Saturation flux density, B_{sat}

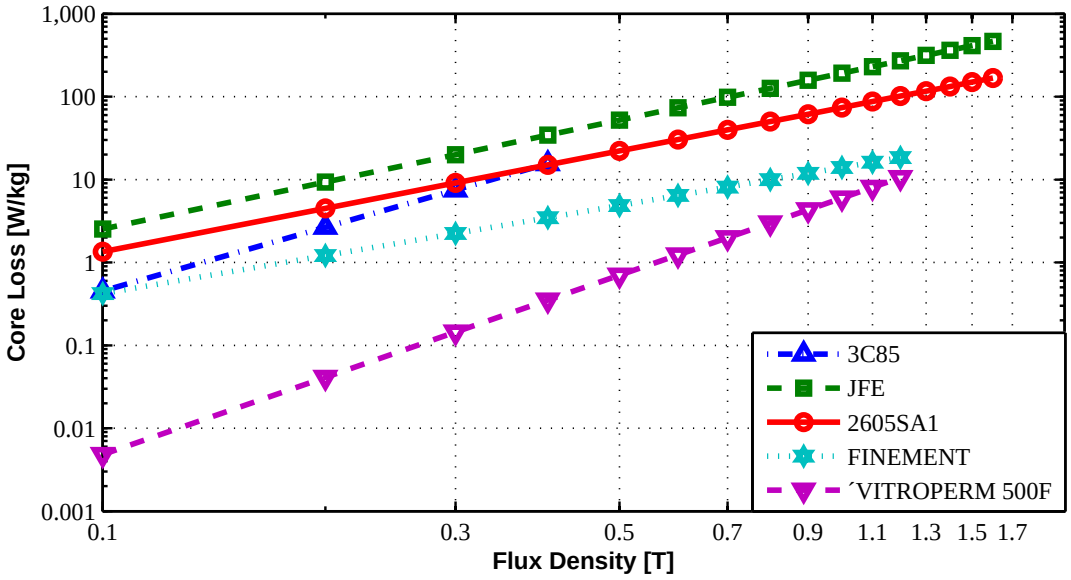

Figure 4.1: Specific core loss comparison of different soft magnetic material versus magnetic flux density at 5 kHz.

- Relative permeability, μ_r
- Temperature characteristics

Based on these parameters, different kinds of magnetic materials may fulfill high frequency requirements. The performance improvement in these materials has been achieved by changing in ingredients, controlling process quality and so on.

A detailed description of the characteristics of magnetic materials which are used in medium to high frequency applications is presented in Table. 4.1. Considering saturation flux density, one can classify these materials starting with the silicon steel family having the highest B_{sat}, and followed by XFlux, amorphous material, nanocrystalline, KoolMu and ferrite. Powdered iron cores have relatively high specific core losses, as well as low relative permeabilities making this type of magnetic materials not to be the first choice for the high power high frequency applications.

A transformer core operates at high temperatures and therefore thermal stability of the materials is of great concern. Theoretically, the Curie temperature is the limitation of maximum operating temperature, but practically, it is the thermal capability limits of lamination and coating that determines the maximum temperature. On the other hand, the thermal conductivity of the material determines the cooling of the core. The highest thermal conductivity is typical for powder cores and the lowest value is for ferrite. The thermal conductivity of the laminated cores is anisotropic and it is much higher in rolling direction rather than across the

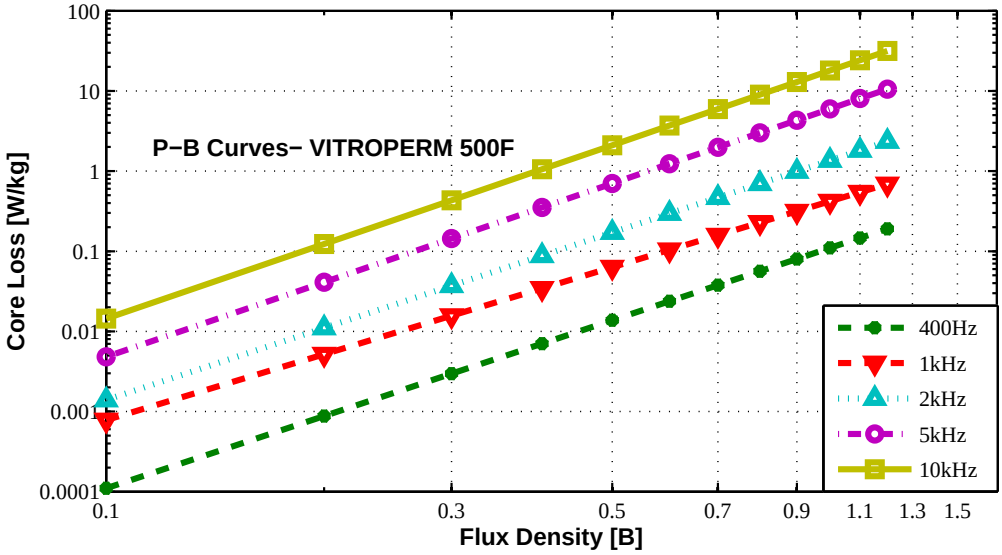

Figure 4.2: Specific core loss of Vitroperm 500F at different frequencies.

lamination. This should be considered in heat transfer modeling and the design methodology.

Fig. 4.1 shows the specific core losses of different magnetic materials versus magnetic flux density at 5 kHz. As it is seen nanocrystalline materials (Vitroperm 500F and Finement) have the lowest specific loss together with relatively high saturation level, B_{sat}. Among all soft magnetic materials, nanocrystalline and Ferrite have higher priority for high frequency high power applications, however using ferrite material, one should compromise with the larger core cross sections, due to lower saturation level, resulting in larger and heavier components which is not desirable in high power density applications.

Fig. 4.2 shows the P-B characteristics of Vitroperm 500F at different frequencies from datasheet provided by VAC.

4.3 Core Loss Calculation Methods

Each magnetic material has an especial working temperature limit which should not be exceeded. Hence, the permitted loss for a particular design will be limited. Consequently, modeling and understanding of losses inside the winding and the core is of great importance and are the basic knowledge to have an optimal design of the transformers especially in high frequency applications [45]. In principle, there are three methods to calculate the core losses of magnetic materials, i.e, loss separation methods, empirical methods and time domain approach which are discussed in this

chapter.

4.3.1 Loss Separation Methods

Within this approach, the total losses are divided into three categories: static hysteresis loss, P_h, dynamic eddy current loss, P_e, and excess loss or anomalous loss, P_{ex}.

4.3.1.1 Eddy current Losses

When a conductive material is exposed to a time-varying magnetic field, some current loops (eddy currents) are induced. To formulate these currents, a thin lamination is considered while exposed to a one directional magnetic field [62]. The time averaged value of the eddy current losses can be calculated by

$$P_e = \frac{\sigma.d^2}{12T}\int_0^T \left(\frac{\partial B(t)}{\partial t}\right) dt \tag{4.1}$$

where σ is the conductivity of the core material, d is the thickness of each lamination and T is the excitation voltage period. In case of sinusoidal excitation, (4.1) gives

$$P_e = \frac{\sigma d^2}{12T}\int_0^T \omega^2 B_m^2 sin^2(\omega t)dt = \frac{\sigma d^2}{24}\omega^2 B_m^2 \tag{4.2}$$

4.3.1.2 Hysteresis Losses

Dependence of magnetic induction on the field is usually non-linear for magnetic materials (ferromagnetics) and it takes a form of so-called hysteresis loop. The hysteresis loss occurs due to movement and rotation of microscopic magnetic domains and it also depends on grain size and material composition. At very low frequencies, eddy current loss is negligible and hence, the total measured loss is equal to hysteresis loss or so called static hysteresis loss [62]. There are several theoretical methods to calculate this type of losses in magnetic materials, among those the Jiles Atherton and Preisach [63, 64] are the most common ones, however these methods are not within the scope of this thesis since they require extensive experiments and parameter fitting procedures in order to have an acceptable parameter identification.

4.3.1.3 Excess Losses or Anomalous

In practice, there is a difference between the measured total magnetic loss and sum of static hysteresis and classical eddy current losses, especially in higher frequencies. This difference is considered as excess or anomalous losses. This loss is a result of domain wall movement during the magnetization which induces microscopic eddy

current loss [62]. In 1983 and 1984, Bertotti [65,66] proposed a statistical loss theory based on the description of the magnetization. In this theory, a number of active correlation regions are considered which are distributed randomly in the material. These active regions are specified by the microstructure of the material such as grain size reflected in the time averaged expression of the excess loss as

$$P_{ex} = \sqrt{\sigma.G.A.V_0}\frac{1}{T}\int_0^T \left|\frac{dB(t)}{dt}\right|^{1.5} dt \tag{4.3}$$

where G is the magnetic object friction coefficient, V_0 is the parameter describing the microstructure of the material and A is the core cross section. Obtaining these coefficients can be difficult due to the lack of enough information from manufacturer.

4.3.1.4 Total Core Losses

The total magnetic field intensity inside a material can be defined as

$$H_{total} = H_{st-hyst} + H_{eddy} + H_{excess} \tag{4.4}$$

which means that the total field is the combination of three components: static hysteresis, eddy current and the field due to excess losses. The first component is static and it is independent of frequency, but the other two components are frequency dependant and broaden the B-H curve when measuring the total core losses. The total power loss density per loop of the magnetic material is

$$P_{total} = \frac{1}{T}\int_0^T \left(H_{st-hyst}\frac{dB(t)}{dt} + \frac{\sigma.d^2}{12}\left(\frac{dB(t)}{dt}\right)^2 + \sqrt{\sigma.G.A.V_0}\left|\frac{dB(t)}{dt}\right|^{1.5}\right) dt \tag{4.5}$$

It should be mentioned that the static hysteresis loss is dominant at low frequencies, while the excess loss is the highest in the mid-range of frequencies. For higher frequencies, the classical eddy current loss is dominant [67].

4.3.2 Time Domain Model

The core loss density is obtained by using the loss separation method in the frequency domain according to

$$\begin{aligned} P_v &= P_e + P_h + P_{ex} \\ &= k_e \cdot f^2 \cdot B_m^2 + k_h \cdot f \cdot B_m^\beta + k_{ex} \cdot f^{1.5} \cdot B_m^{1.5} \end{aligned} \tag{4.6}$$

Here, P_v is the core loss per unit volume, P_e is eddy current loss, P_h is hysteresis loss, P_{ex} is excess loss, β is the power factor (usually equal to 2), f is the operating

frequency, B_m is the maximum value of the magnetic flux density, k_e, k_h and k_{ex} are the loss coefficients which are to be extracted from the provided P-B curves, as seen in Fig. 4.1 and Fig. 4.2 , of the studied magnetic material and other characteristics of the core material [68].

As mentioned before, the time averaged value of the eddy current loss can be calculated using the expression

$$P_e = \frac{\sigma.d^2}{12T}\int_0^T \left(\frac{\partial B(t)}{\partial t}\right) dt \tag{4.7}$$

The coefficient k_e is determined by equating P_e in (4.6) and (4.7) under sinusoidal excitation since (4.6) is only valid for sinusoidal waveforms. Therefore the instantaneous value for the eddy current loss can be evaluated through

$$P_e(t) = \frac{1}{2\pi^2}k_e\left(\frac{dB(t)}{dt}\right)^2 \qquad , \qquad k_e = \frac{\sigma\pi^2 d^2}{6} \tag{4.8}$$

As mentioned before, The time averaged value of the excess loss is obtained as

$$P_{ex} = \sqrt{\sigma.G.A.V_0}\frac{1}{T}\int_0^T \left|\frac{dB(t)}{dt}\right|^{1.5} dt \tag{4.9}$$

Since a complete material characterization is not usually available from manufacturers, k_{ex} in (4.6) cannot be directly extracted. One can notice, by comparing (4.9) with the corresponding term in (4.6), that the magnitude of the coefficient, k_{ex}, is dependent on G and V_0. Therefore, a curve fitting is necessary to determine the value of k_{ex} [47] . Assuming pure sinusoidal excitation and equating one can write

$$k_{ex} = \sqrt{2\pi\sigma.G.A.V_0}\frac{2\pi}{T}\int_0^T |sin(2\pi ft)|^{1.5}\, dt \tag{4.10}$$

hence, the instantaneous value of excess loss can be calculated by

$$P_{ex}(t) = \frac{1}{8.76}k_{ex}\left|\frac{dB(t)}{dt}\right|^{1.5} \tag{4.11}$$

The time averaged hysteresis loss density can be calculated as

$$P_h = \frac{1}{T}\int_0^T H(t)\frac{dB(t)}{dt}dt \tag{4.12}$$

In order to calculate hysteresis losses in the time domain, the equivalent elliptical loop (EEL), which was originally introduced in [68] and implemented in the finite element software Maxwell, method is used. The magnetic hysteresis loss is described

as a function of the irreversible component of the magnetic field H_{irr} and the ellipse parameters are represented as

$$B = B_m sin(\theta) \quad , \quad H_{irr} = H_m cos(\theta) \tag{4.13}$$

where $\theta = 2\pi ft$ and H_m is the peak value of the magnetic field intensity. The area of the resulted ellipse is equal to the hysteresis loss. substituting (4.13) into (4.12) , the time averaged value of P_h can be written as

$$P_h = \frac{1}{T}\int_0^T H_m B_m 2\pi f cos^2(\theta) dt = \pi f H_m B_m \tag{4.14}$$

equating (4.14) and P_h in (4.6) and rearranging for k_h gives

$$k_h = \frac{\pi H_m}{B_m^{\beta-1}} \tag{4.15}$$

substituing H_m from (4.15) into (4.13), one can derive

$$H_{irr} = \frac{k_h}{\pi} B_m^{\beta-1} cos(\theta) \tag{4.16}$$

hence

$$P_h = \frac{k_h}{C_\beta}\frac{1}{T}\int_0^T |B_m cos(2\pi ft)|^{\beta-1} \frac{dB(t)}{dt} dt \tag{4.17}$$

where

$$C_\beta = 4\int_0^{\frac{\pi}{2}} cos^\beta(\theta) d\theta \tag{4.18}$$

The time averaged loss P_h is derived using the irreversible component of magnetic field intensity . Therefore, the instantaneous hysteresis loss can be written as

$$P_h(t) = \frac{k_h}{C_\beta} |B_m cos(2\pi ft)|^{\beta-1} \frac{dB(t)}{dt} \tag{4.19}$$

Thus, the three components of the instantaneous magnetic loss in 3D cases for soft magnetic materials are as follows

$$
\begin{aligned}
P_v(t) &= P_e(t) + P_h(t) + P_{ex}(t) \\
&= \frac{k_e}{2\pi^2}\left(\left(\frac{dB_x(t)}{dt}\right)^2 + \left(\frac{dB_y(t)}{dt}\right)^2 + \left(\frac{dB_z(t)}{dt}\right)^2\right) \\
&+ \frac{k_h}{C_\beta}\cdot|B_m\cdot cos(2\pi ft)|^{\beta-1}\left(\left|\frac{dB_x(t)}{dt}\right| + \left|\frac{dB_y(t)}{dt}\right| + \left|\frac{dB_z(t)}{dt}\right|\right) \\
&+ \frac{k_{ex}}{8.76}\left(\left(\frac{dB_x(t)}{dt}\right)^{1.5} + \left(\frac{dB_y(t)}{dt}\right)^{1.5} + \left(\frac{dB_z(t)}{dt}\right)^{1.5}\right)
\end{aligned}
\tag{4.20}
$$

Here, $P_h(t)$, $P_e(t)$ and $P_{ex}(t)$ are the instantaneous values for the hysteresis, eddy current and excess loss, respectively [69].

It should be noted that the time dependent method are used for all of the FEM derived core loss calculations in this thesis. The loss coefficients, k_h and k_{ex}, are identified applying the least square method on the difference between the loss density obtained from measurements provided by manufacturer, (Fig. 4.2), and the loss density calculated by (4.6) as

$$
Error(k_h, k_{ex}) = \sum_{i=1}^{n}\left(P_{vi} - \left(k_e f^2 B_m^2 + k_h f B_{mi}^{\beta} + k_{ex} f^{1.5} B_{mi}^{1.5}\right)\right)^2 \tag{4.21}
$$

where B_{mi} and P_{vi} are the values corresponding to i^{th} point on P-B curve at any given frequency.

4.3.3 Empirical Methods

Loss separation method method gives the capability of estimating the core loss for arbitrary waveforms. Nevertheless, only eddy current loss can be calculated and the factors and coefficients in the other two components should be obtained through extensive experiments and parameter fitting procedures. Due to this drawback, this model seems to be insufficient and impractical for the designers who prefer to use easy methods and lower amount of data resources of materials. In 1892, Steinmetz presented an equation to estimate the magnetic loss inside the materials which was only dependant on the peak value of the magnetic induction [70].

4.3.3.1 OSE

Currently, a more general and verified version of the Steinmetz equation is used by the designers of magnetic devices known as the original Steinmetz equation (OSE) which basically resulted from the curve fitting of several experiments under sinusoidal excitations at different frequencies and peak magnetic inductions as follows

$$P_c = k f^{\alpha} B_m^{\beta} \tag{4.22}$$

where f is the fundamental frequency of the excitation and B_m is the peak magnetic induction. Furthermore, k, α and β are determined by material characteristics and can be easily obtained using manufacturer datasheets without requiring any detailed knowledge of the materials. This expression has a very good accuracy for sinusoidal excitations. However, due to the increasing use of power electronic conversion systems, there is an urgent need to find a method with acceptable accuracy for non-sinusoidal flux waveforms. To overcome this problem, the Fourier transform was applied in [71], which could be used for any arbitrary waveform to decompose it in a series of sinusoidal waves. Then, (4.22) was applied to each sinusoidal component and using the superimposed effect of harmonics, the total loss could be obtained. However, this summation has a considerable difference with the measured values, since there is no orthogonality between different harmonics due to the nonlinear nature of magnetic materials.

4.3.3.2 MSE

The empirical Steinmetz equations have been the most practical and useful tool for the evaluation of magnetization losses in recent years. Therefore, several modifications have been implemented to extend them for non-sinusoidal waveforms. The first improvement was done based on the physical understanding of hysteresis dynamics and correlating the magnetic loss with the rate of the change of magnetic flux density. Based on this idea, an equivalent frequency, f_{eq}, was introduced [72] which is depending on $\frac{dB}{dt}$.

$$f_{eq} = \frac{2}{\Delta B^2 \pi^2} \int_0^T \left(\frac{dB(t)}{dt} \right)^2 dt \tag{4.23}$$

where T is the period of the flux waveform and ΔB is the peak to peak flux amplitude. Considering this equivalent frequency, the magnetic loss density is determined by the modified Steinmetz equation (MSE) as

$$P_c = \left(k f_{eq}^{\alpha - 1} B_m^{\beta} \right) f \tag{4.24}$$

where f is the excitation fundamental frequency.

4.3.3.3 GSE

To correct the mismatch between the MSE and OSE for sinusoidal waveforms, another modification was proposed [73]. This idea is based on the physical assumption that the loss inside the material is not only depending on the rate of changes in magnetic induction, but also related to the instantaneous value of flux density. Taking

into account this assumption, generalized Steinmetz equation (GSE) was presented as

$$P_c = \frac{1}{T}\int_0^T kk_i \left|\frac{dB(t)}{dt}\right|^{\alpha} |B(t)|^{\beta-\alpha}\, dt \tag{4.25}$$

where

$$k_i = \frac{1}{(2\pi)^{\alpha-1}\int_0^{2\pi} |cos(\theta)|^{\alpha} |sin(\theta)|^{\beta-\alpha}\, d\theta} \tag{4.26}$$

4.3.3.4 IGSE

The other commonly used expression for core loss calculations is known as the improved generalized Steinmetz equation (IGSE) [74] .

$$P_c = \frac{1}{T}\int_0^T kk_i \left|\frac{dB(t)}{dt}\right|^{\alpha} \Delta B^{\beta-\alpha} dt \tag{4.27}$$

where

$$k_i = \frac{1}{(2\pi)^{\alpha-1}\int_0^{2\pi} |cos(\theta)|^{\alpha}\, 2^{\beta-\alpha} d\theta} \tag{4.28}$$

In this method, the instantaneous value of B is replaced by the peak to peak value ΔB and the waveform could be split into one major and several minor loops and the derived expression would be applied to each loop separately. In [75], a similar approach was introduced and named natural Steinmetz equation resulted in a same expression as IGSE.

4.3.3.5 WCSE

The latest modification on Steinmetz equation was done by Shen which is known as Waveform-coefficient Steinmetz Equation (WcSE) [76]. He presented a coefficient for (4.22), to establish a relationship between any arbitrary waveform with the sinusoidal one with the same peak flux density. This flux waveform coefficient (FWC) can be obtained by calculating the area of the flux waveform and divide it by the corresponding value of the sinusoidal flux.

$$FWC = \frac{\int_0^{\frac{T}{4}} \phi_{arb}(t)}{\int_0^{\frac{T}{4}} \phi_{sin}(t)} \tag{4.29}$$

where $\phi_{arb}(t)$ and $\phi_{sin}(t)$ are the instantaneous value of magnetic flux inside the core associated with arbitrary and sinusoidal excitations, respectively. This correction factor is directly multiplied by the core loss expression of OSE, (4.22) as follows

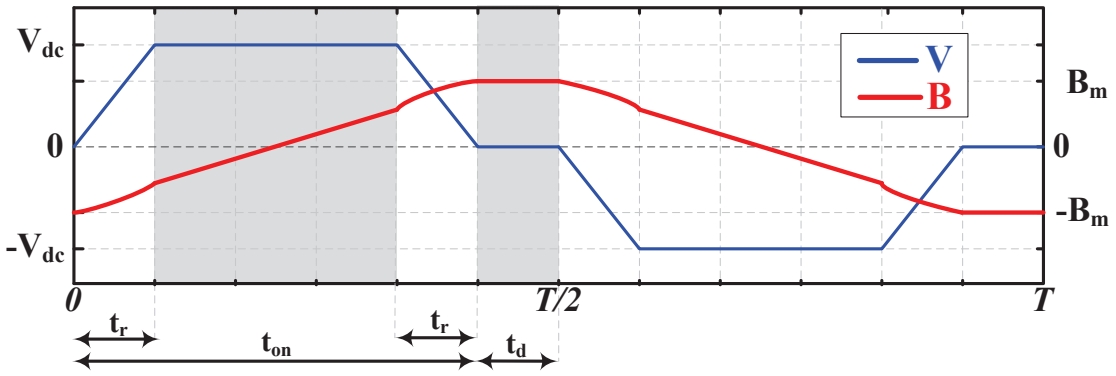

Figure 4.3: The excitation voltage and the corresponding instantaneous value of magnetic flux density .

$$P_c = FWC.kf^{\alpha}B_m^{\beta} \tag{4.30}$$

4.4 Modified Empirical Expressions for Non-Sinusoidal Waveforms

In this part, the aforementioned empirical loss calculation methods are modified to be applicable for rectangular waveforms considering the respective duty cycles and rise times which is the typical waveforms in switch+mode magnetics. In order to have an appropriate comparison and study of core loss by varying the waveform characteristics, the maximum value of the applied voltage is considered as a constant value. However, the peak induction will be fixed. Consequently, by changing the shape of the voltage waveform, for instance the rise time or duty cycle, the effective cross section of the core is varied to have a constant value of B_m. The required core cross section for the mentioned waveforms can be obtained as

$$A_c = \frac{V_{rms}}{k_f k_c N B_m f} \tag{4.31}$$

where V_{rms} is the rms value of the voltage depicted in Fig. 4.3 , k_c is the filling factor of the core, N is the number of primary or secondary turns depending on the corresponding voltage and f is the fundamental frequency. The coefficient k_f is defined as

$$k_f = \frac{2\sqrt{2D - \frac{8}{3}R}}{D - R} \tag{4.32}$$

Where D is the duty cycle and R is the relative rise time in the rectangular waveform with respective rise and fall time defined as

$$D = \frac{t_{on}}{T} \leqslant \frac{1}{2} \quad , \quad R = \frac{t_r}{T} \leqslant \frac{1}{4} \tag{4.33}$$

The waveforms of the instantaneous voltage and the corresponding flux density for one period are depicted in Fig. 4.3 where the time periods t_{on} and t_r are illustrated. The flux density waveform can be easily obtained by integration of the voltage and dividing it by the number of respective winding turns and cross section of the core. As can be seen, whenever the voltage is constant, the induction has a linear behavior, but in rise and fall times when voltage is changing, the induction has a second order pattern.

4.4.0.6 Modified MSE

Using the previously presented empirical equation of loss method for MSE and also using (4.31) and (4.32) for the cross sections, an easy to use expression for magnetic core loss is derived as

$$P_{c-MSE} = \left[\frac{2\left(2D - \frac{8}{3}R\right)}{\pi^2 \left(D - R\right)^2}\right]^{\alpha-1} k f^{\alpha} B_m^{\beta} \tag{4.34}$$

4.4.0.7 Modified IGSE

Similarly, the calculated expression for IGSE method, suitable for loss evaluation of the waveform presented in Fig. 4.3, is derived as

$$P_{c-IGSE} = \left(2D - \frac{4\alpha}{\alpha+1}R\right) \frac{2^{\beta}}{(D-R)^{\alpha}} k k_i f^{\alpha} B_m^{\beta} \tag{4.35}$$

4.4.0.8 Modified WCSE

The modified WCSE expression is derived as

$$P_{c-WCSE} = \frac{4\pi}{D-R}\left[\frac{(D-2R)^2}{8} + \frac{R^2}{3} + \frac{(1-2D)(D-R)}{8}\right] k f^{\alpha} B_m^{\beta} \tag{4.36}$$

Based on the assumptions and procedure of the methods, correction coefficients were added to the main OSE equation, to extend and adapt it to the studied non-sinusoidal waveform. These coefficients are only dependent on two main factors, R and D which were previously defined in (4.33). The important issue to mention from the equations presented above are that the magnetic loss density depends not

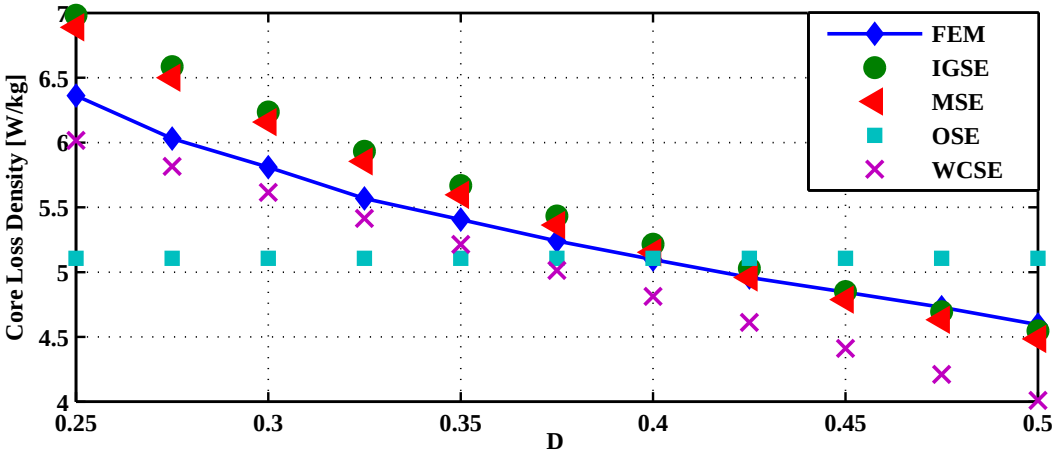

Figure 4.4: Accuracy investigation of the modified Steinmetz equations with different values of D and $R = 0$.

only on the frequency and peak magnetic induction, but also on D and R of the waveform depicted in Fig. 4.3.

It should be noted that, due to the presence of a second order term with a non-integer exponent $(\beta - \alpha)$ within integration process, it is not possible to achieve any closed form expression for GSE accounting for core losses in non-sinusoidal waveform shown in Fig. 4.3.

4.4.1 Validity Investigation for Different Duty Cycles, D

In this part, different waveforms with different values of D, with $R = 0$, have been applied on a case study transformer which is a 1 MVA, 1/10 kV transformer designed for 5 kHz with 6 turns of the primary windings and the peak value of the magnetic flux density is set to 0.9T. The core material used for all simulations in this comparison is VITROPERM500F as its core loss characteristics presented in Fig. 4.2.

To study the effect of the duty cycle, D has been changed from 0.25 to its maximum, 0.5. The obtained results are depicted in Fig. 4.4. In order to have a fixed maximum flux density in all simulations, the dimension of the transformer at each simulation should be changed according to (4.31) which simply means that by increasing the duty cycle, the cross section of the core will increase.

The results presented in Fig. 4.4 can be interpreted from two points of view. Firstly, reducing the duty cycle leads to higher magnitude of losses inside the core. Secondly, for high duty cycles, the OSE which only considers the sinusoidal waveforms has a good accuracy and its deviation from the result obtained by FEM is less than 10 percent. However, there are considerable deviations at lower values of

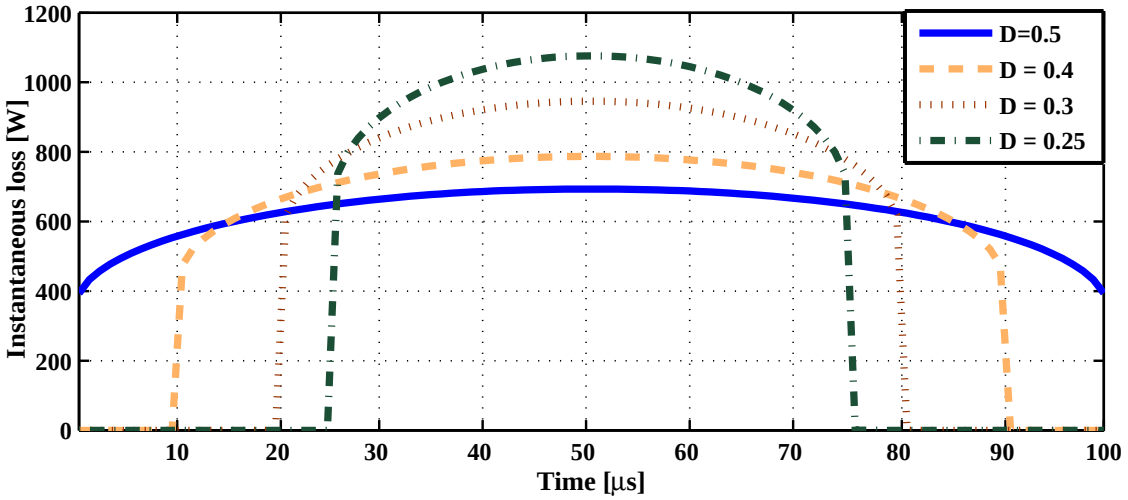

Figure 4.5: Instantaneous core loss waveform in a half period with different values of D and $R = 0$.

D between the core loss densities obtained by OSE and FEM simulations. The most acceptable accuracy is around D = 0.4 where almost all the methods provide similar results. In general the modified IGSE and MSE methods has a higher accuracy compared to OSE and WCSE. Therefore they will be later utilised in the high power density transform design.

Fig. 4.5 shows the computed instantaneous core loss of four different duty cycles for half a period using a FEM software at 5 kHz. By decreasing the duty cycle, the maximum value of instantaneous loss will increase since the rate of change of B, $\frac{dB(t)}{dt}$, increases. This is the most important term in the transient loss calculation methods. The other interesting point regarding Fig. 4.5 is that the peak value of instantaneous core loss occurs at $t = \frac{T}{4}$ which is due to the term $|B_m \cdot cos(2\pi ft)|$ in (4.20). Moreover, for lower duty cycles, the peak value of the core loss is higher.

4.4.2 Validity Investigation for Different Rise Times, R

In addition to the duty cycle, the rise and fall time, R, of the excitation voltage has a significant effect on the magnetic core loss. The comparison between the calculated average core loss density obtained by different modified Steinmetz equations, as well as FEM simulations has been shown in Fig. 4.6. It should be mentioned that, as in the previous section, all the calculations and simulations for different values of R were performed in the condition of similar V_{dc} and B_m.

As can be seen in Fig. 4.6 the magnetic loss increases at higher R values except for the OSE. The longer the rise time, the higher the loss inside the core will be.

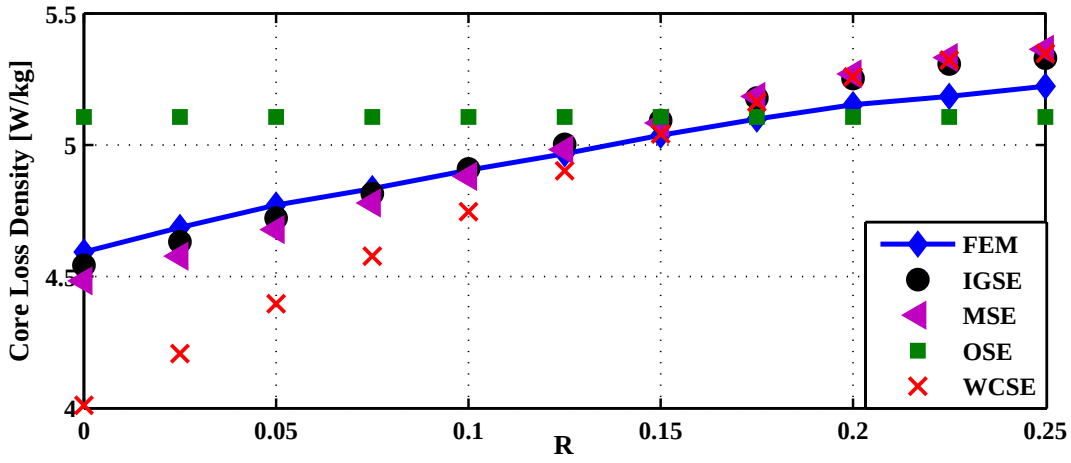

Figure 4.6: Accuracy investigation of the modified Steinmetz equations with different R values and $D = 0.5$.

Changing R from zero to 0.25 which means from rectangular to triangular, results in almost a 35 percent increase in the core loss. For values of R close to 0.25 , i.e. t_r close to $\frac{T}{4}$, the voltage waveform approaches the triangular shape. In this case, the voltage increases linearly which generates a parabolic flux density waveform. In order to compare the resulting loss densities properly, B_m should be kept constant. The quadratic polynomial flux density results in a higher magnitude of the magnetic loss.

Moreover, as can be seen in Fig. 4.6, the modified IGSE and MSE have an acceptable accuracy at almost all values of R particularly when R is very small which is the case of most power electronics wavwforms. By decreasing the rise time, the OSE and its modification, WcSE, deviates more from the results obtained by FEM simulations whereas the other group including IGSE and MSE has negligible deviations from FEM.

The instantaneous core loss at four different values of R in one period are illustrated Fig. 4.7. As can be seen, during the transition time, the core loss has a polynomial behavior. Besides, the highest loss occurs at R equal to 0.25.

4.5 Conclusions

The transformers used in power electronic converters are frequently subjected to non-sinusoidal voltages. As a consequence of the increasing use of these waveforms, the effects of arbitrary waveshapes on the efficiency of the transformers should be investigated. The magnetic losses due to sinusoidal excitation can be easily calculated using the datasheet provided by manufacturers. In non-sinusoidal and harmonic

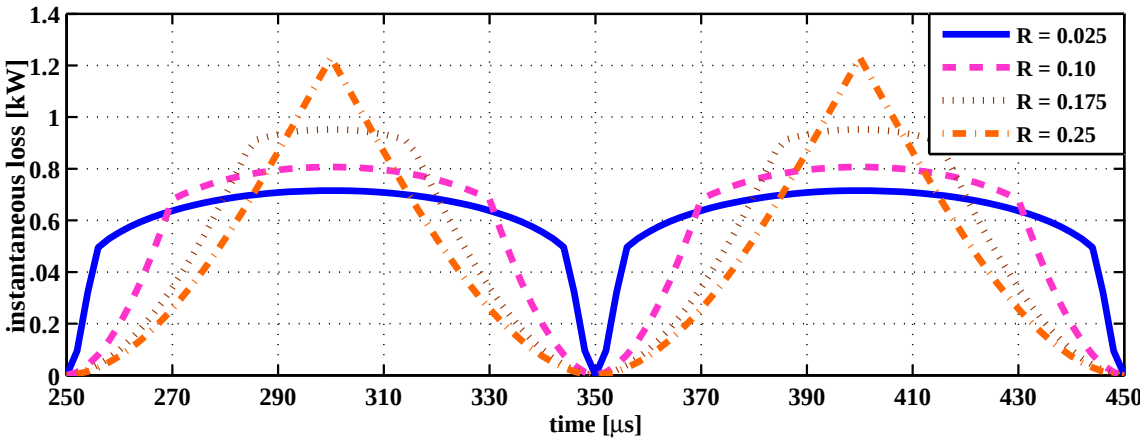

Figure 4.7: Instantaneous core loss waveform with different values of R and $D = 0.5$.

cases, due to the nonlinear behavior of magnetic materials, more complex methods are necessary. The main aim of this chapter was to study the effect of the commonly used power electronic waveforms on the core losses. Accordingly, using the proposed modification of the Steinmetz equation in literatures, such as MSE, IGSE and WcSE, some general expressions were derived and presented for rectangular waveform with its associated duty cycle and rise time. In each of these expressions, a correction factor is introduced to relate the Steinmetz expression to these waveforms.

Chapter 5

Design Methodology and Optimization

5.1 Introduction

The plan of this chapter is as follow. First, one of the most attractive power electronic topologies for high power applications,the dual active bridge, is briefly introduced. Then, system specifications of a case study utilizing the DAB topology are introduced. Using the theoretical expressions derived in the previous chapters, a design methodology addressing the high isolation requirements of the off-shore based transformers as well as required leakage inductance of the DAB topology is introduced. Incorporating this design methodology, an optimization process with a wide range of parameter variations is performed to get the highest power density while the efficiency, isolation, thermal and leakage inductance requirements are all met.

5.2 DAB Converter

Recently, there has been growing interest in utilising dual Active bridge (DAB) converters in high power applications. The equivalent circuit of a DAB converter is shown in Fig. 5.1 in which two square wave voltage waveforms on two sides of the transformer has been shifted by controlling the input and output bridges, applying full voltage over the inductance, L_σ, which is used to shape the current as a power transfer element [44].

The steady state transformer voltage and current waveforms of a DAB converter with simple phase shift modulation is shown in Fig. 5.2 (a). There are six distinct states of IGBTs and diodes conduction as shown in Fig. 5.2 (b) and (c). It is worth to point out out that in order to have soft switching at turn on, the antiparallel diode of each switch should start conducting prior to the turn on moment. This

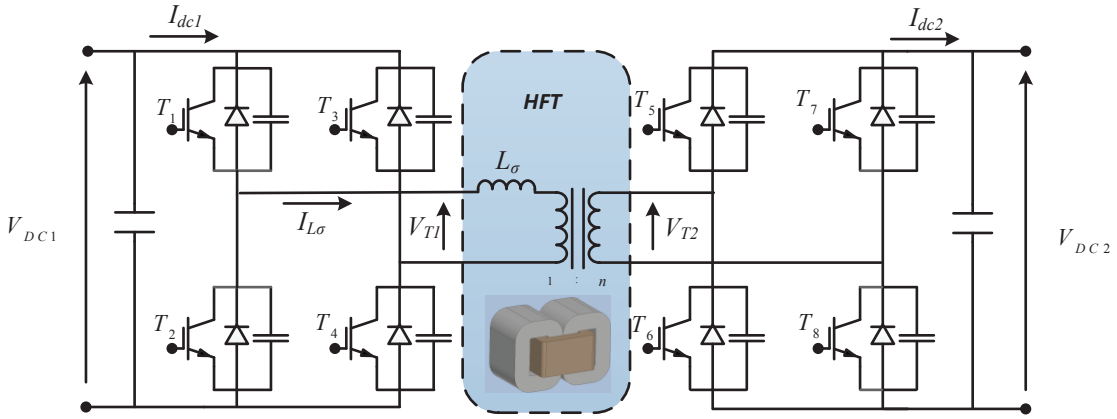

Figure 5.1: Dual Active Bridge circuit.

attribute is clearly demonstrated in Fig. 5.2 (b) and (c) when the voltage over each switch is zero prior to turn on, whereas the turn off process is not necessarily soft. In order to achieve zero voltage switching (ZVS) at turn on, the phase shift between the bridges, φ, should be higher than a certain value resulting in a minimum value of the series inductance as presented in (5.1). This inductance is preferably integrated as the leakage inductance of the high frequency transformer, Fig. 5.1, in order to reduce the number of components, hence achieving higher power densities.

$$L_\sigma = \frac{V_{DC_1} V_{DC_2} \varphi_{min} (\pi - \varphi_{min})}{2 P_{out} \pi^2 f_s n} \tag{5.1}$$

where φ_{min} can be calculated by

$$\begin{aligned} \varphi &> \frac{\pi\,(d-1)}{2d} \quad for \quad d > 1 \\ \varphi &> \frac{\pi\,(1-d)}{2} \quad for \quad d < 1 \end{aligned} \tag{5.2}$$

and d is defined as

$$d = \frac{V_{DC2}}{n V_{DC1}} \tag{5.3}$$

These waveforms will be later, in this chapter, used as the excitation within the design and optimization process. The RMS value of the transformer current can be calculated by

$$I_{T1}\,(rms) = \frac{n V_{DC1} + V_{DC2}}{n L_\sigma} \sqrt{\frac{4 t_1^2 t_\varphi + T_s t_1^2 - 4 t_\varphi^2 t_1 - T_s t_1 t_\varphi + T_s t_\varphi^2}{3 T_s}} \tag{5.4}$$

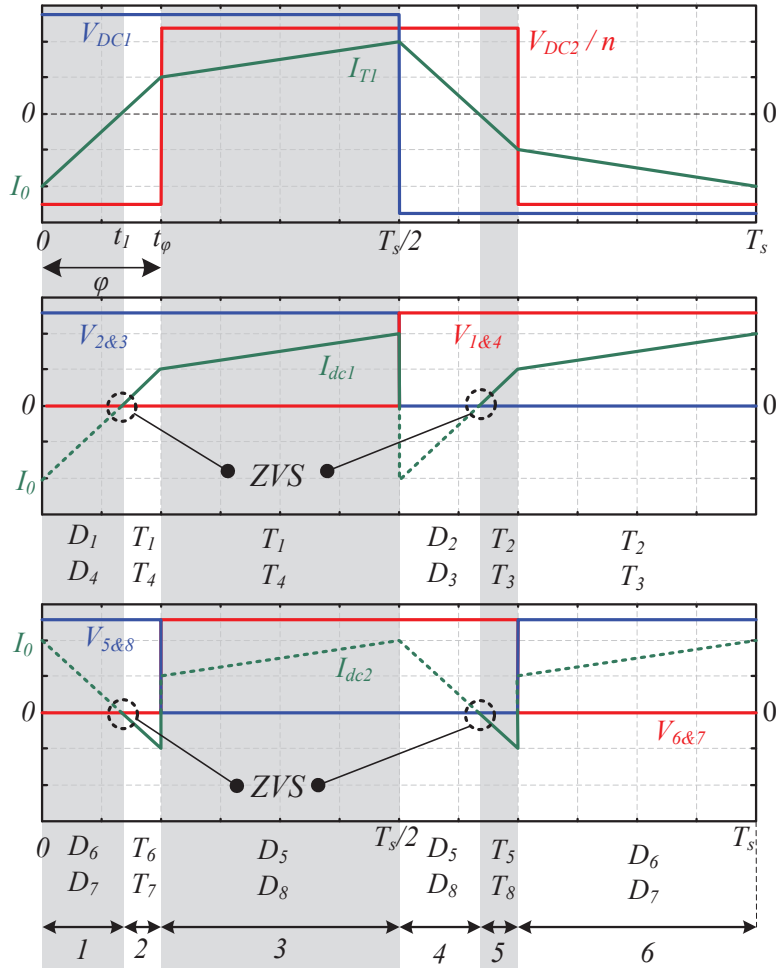

Figure 5.2: Steady state voltage and current waveforms of a DAB converter with simple phase shift modulation.

where t_1 and t_φ can be respectively calculated by

$$t_1 = \frac{\pi + 2\varphi d - \pi d}{4\pi f\,(1+d)} \tag{5.5}$$

$$t_\varphi = \frac{\varphi}{2\pi f} \tag{5.6}$$

Using (5.1), the apparent power of the transformer can be calculated from

$$S_T = \frac{1}{2}\left(V_{T1(rms)} I_{T1(rms)} + V_{T2(rms)} I_{T2(rms)}\right) = \frac{1}{2} V_{DC1} I_{T1(rms)} (1+d) \tag{5.7}$$

5.3 Optimization Procedure

In contrast to most of the proposed design methodologies for high frequency transformers emphasizing on core selection based on a parameter called area product, A_p, [9, 10] the design methodology proposed in this chapter stands for the incorporated leakage inductance of the transformer and its corresponding phase shift within the DAB topology. Moreover, the isolation requirements introduced by the medium voltage DC link is considered as one of the design inputs making this design suitable for high power medium frequency off-shore dc-dc converters.

Unlike the conventional design of magnetic components where the core will be initially selected from a manufacturer lookup table, the core dimensions are not a limiting factor in this optimizations [11, 77]. It is assumed that specific core dimensions for specific high power density applications can be tailored by core manufacturers.

Fig. 5.3 shows the proposed optimization flowchart used for designing a medium frequency high power transformer. First, the converter level requirements, i.e, output power, voltage levels, operating frequency, transformer turn ratio, required leakage inductance and isolation requirements are selected. Then, fixed parameters including suitable core material selection, inter layer and inter core distances and the insulation material are chosen. Having the dielectric characteristics, the minimum required isolation distance and clearance distances are calculated.

After selecting the core material and construction, dielectric material and the required fixed distances, several free parameters comprised of geometrical and electrical parameters are chosen and will be swept within a wide range in order to find the minimum transfer volume meeting the efficiency and heat dissipation demands. Once a set of free parameters are established, one can determine all the geometrical dimensions of the transformer addressing the required distances to achieve the desirable leakage inductance, winding and core dimensions and other geometrical parameters shown in Fig. 5.3 and Fig. 5.4.

The next stage is loss evaluations performed by utilising the modified empirical methods and FEM derived analytical methods explained in previous chapters. On the other hand the maximum heat dissipation capability of the transformer corresponding to each combination of free parameters are calculated in order to reject those combinations of free paraeters which resulted in unacceptable power losses. Finally, the optimal set of free parameters resulting in the highest efficiency while meeting the loss dissipation and isolation requirements are presented. These steps are described in detail as follows.

5.3.1 System Requirements and the Case Study

A 5 MW, 3/30 kV turbine base isolated DC-DC converter has been considered as a case study in this chapter. Similar to the configuration presented in Fig. 5.5,

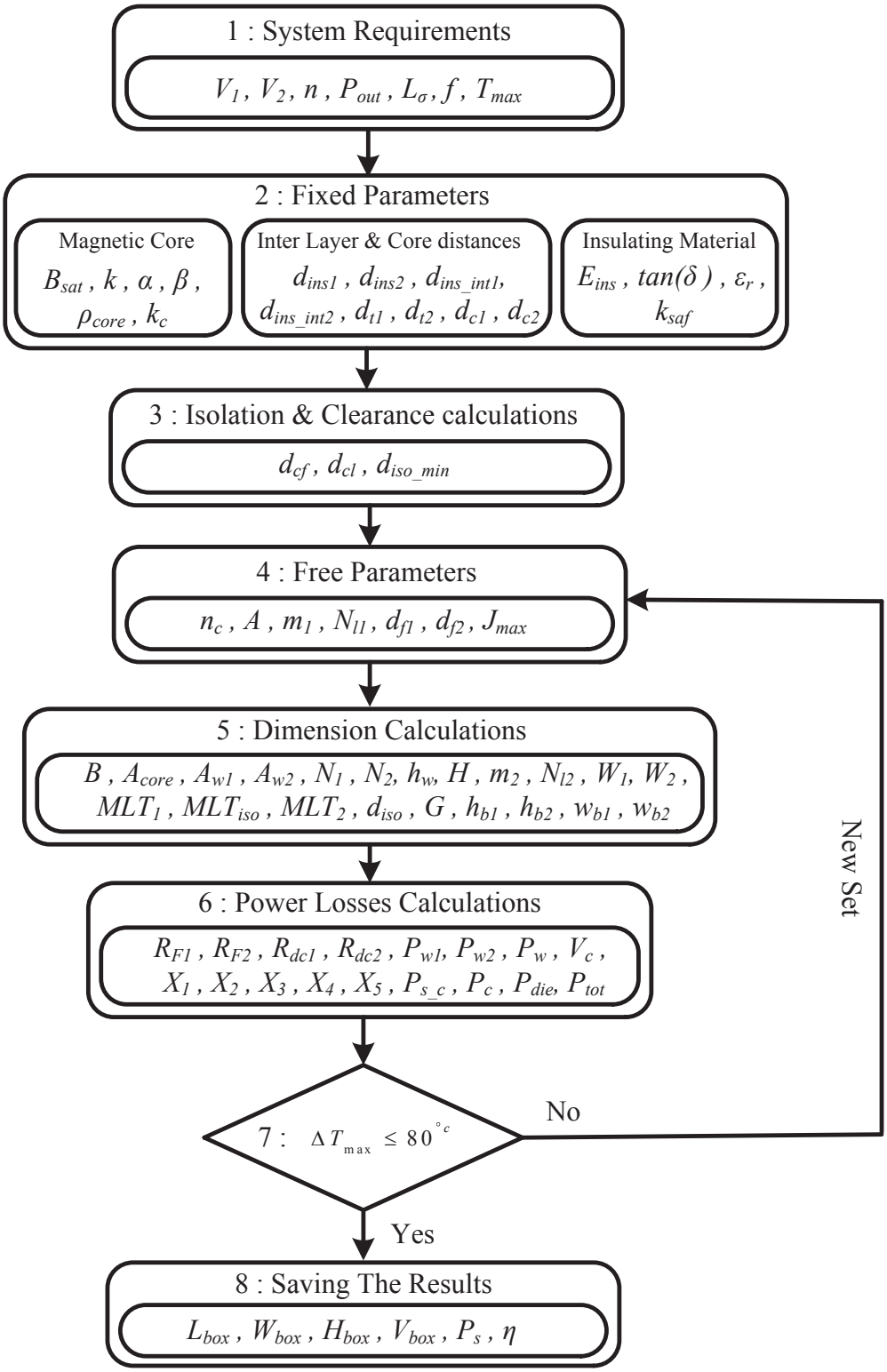

Figure 5.3: Design Algorithm.

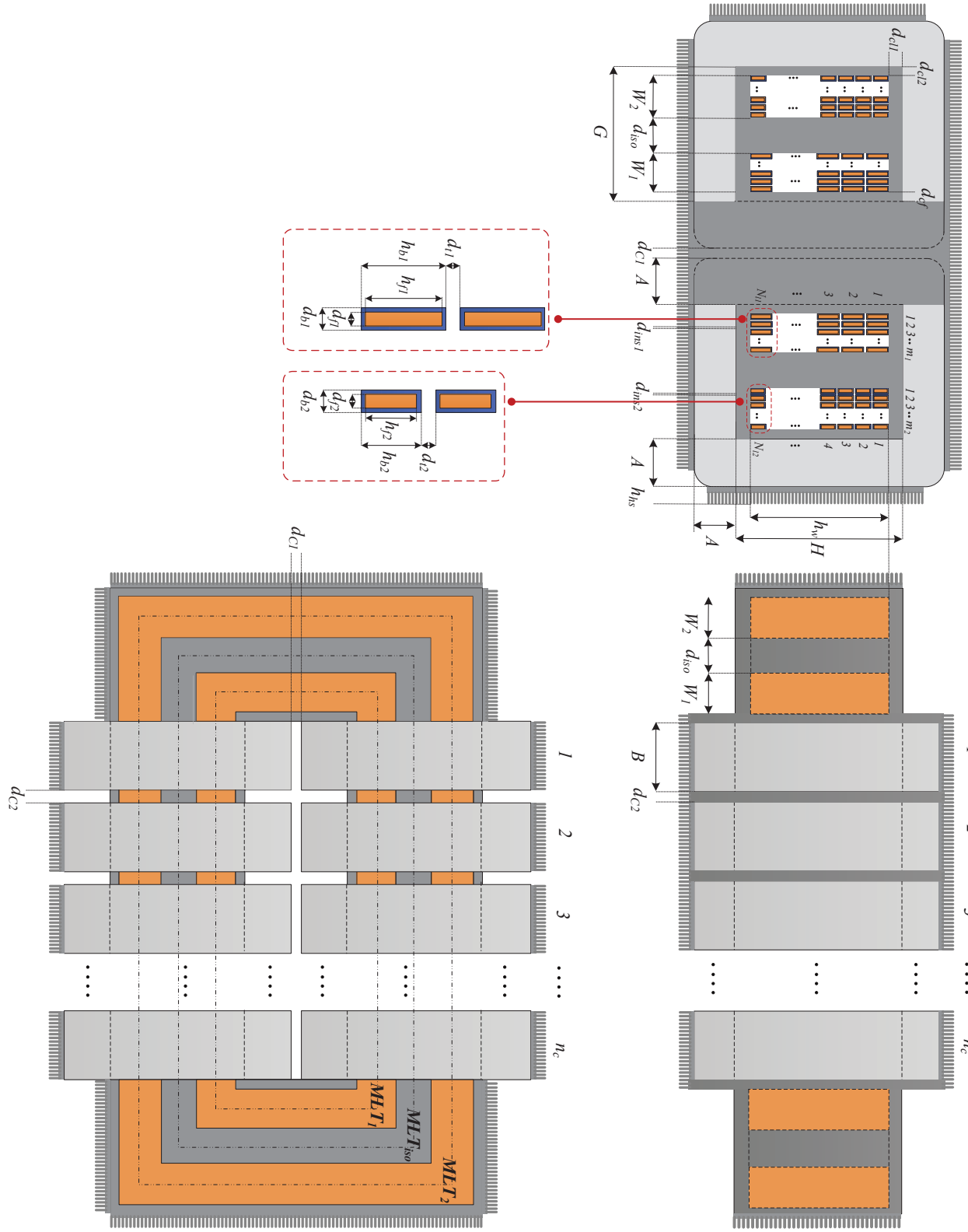

Figure 5.4: Design sketch.

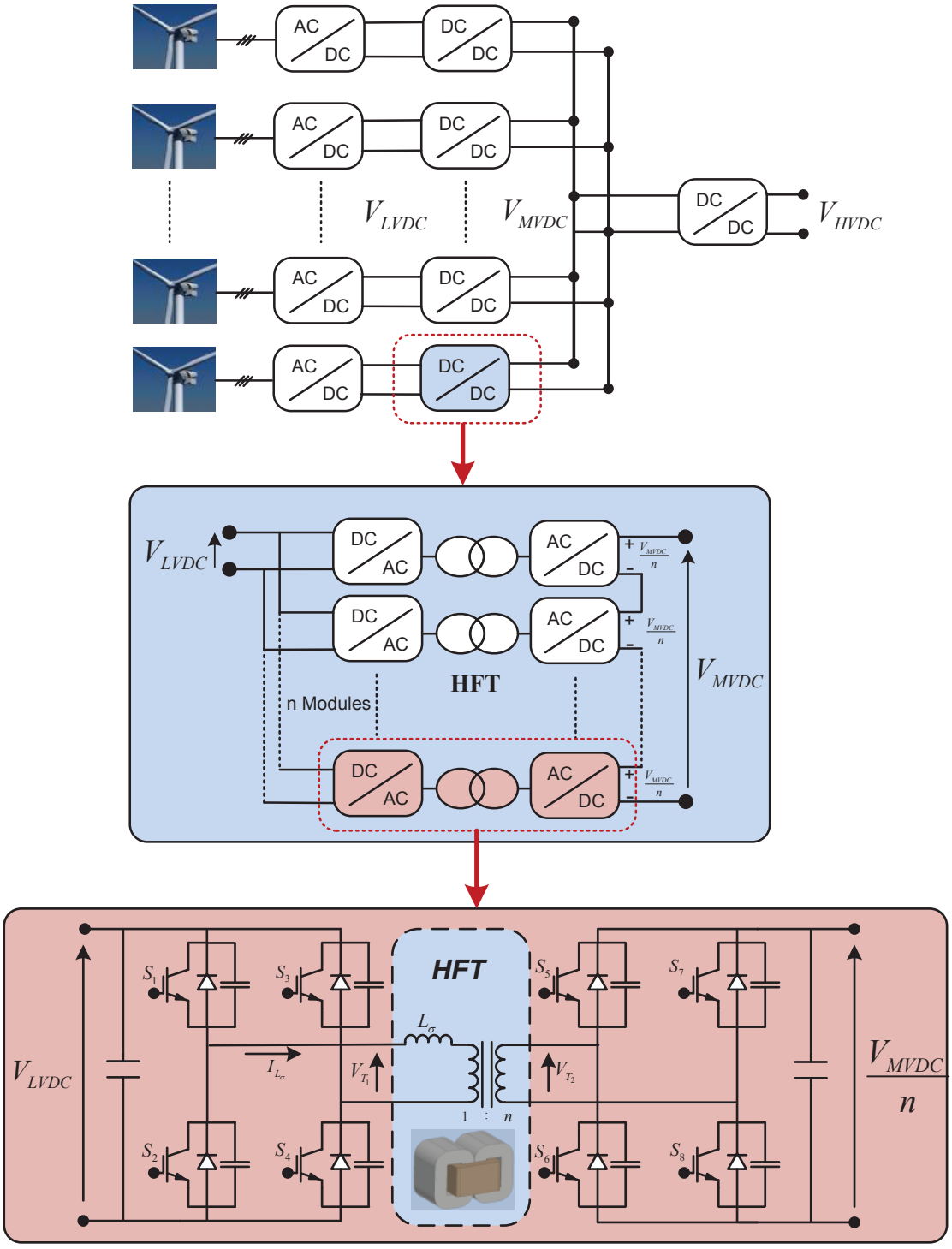

Figure 5.5: Parallel input, series output modular configuration of the isolated DAB DC-DC converter for HVDC offshore applications.

Table 5.1: Design Specification of the Converter Module

Output Power, P_{out}	1 MW
Module LV side voltage, V_{LV}	3 kV
Module HV side voltage, V_{HV}	6 kV
Leakage inductance, L_σ	22 μH
Transformer turn ratio, n	2
Isolation level, V_{iso}	60 kV
Switching frequency, f	5 kHz

this converter can be considered as 5 modules connected in parallel at low voltage side (generator side) and in series at the high voltage side (MVDC link). The specification of each module are tabulated in Table. 5.1. The isolation level, 60 kV, is considered two times of the MVDC voltage level. The designated value of the leakage inductance ensures soft switching of the converter with the maximum 5% output voltage deviation.

The transformer is exposed to the voltage and current waveforms shown in Fig. 5.2 (a) as the standard waveforms of DAB converter. However, the proposed design methodology can easily be applied on other types of modulations with duty cycles, D_1 and D_2, below 0.5.

5.3.2 Fixed Parameters

Prior to the iterative part of the optimization, the magnetic core material, insulation material and the windings interlayer distances need to be set.

As discussed in Chapter 4, Nanocrystalline, compared to other magnetic materials, presents a superior characteristics such as low specific loss at higher frequencies and relatively high magnetic induction which is particularly an important characteristics in high power density applications. Therefore, Vitroperm500F is chosen as the magnetic material used in the current case study optimization. The Steinmetz constants of different magnetic materials, extracted from manufacturer datasheets, are tabulated in table. 5.2. Later, the design outcomes using different magnetic materials are compared in order to observe the effect of different magnetic material on the efficiencies and power densities.

Insulation material determines the other set of fixed parameters used in the proposed design methodology. As can be seen in Fig. 5.4, the dry type isolating material, which provides high dielectric strength, is used within the isolation and clearance distances, d_{iso} and d_{cl}. In addition, as shown in Fig. 5.4, the coil former in distance between the inner layer of the primary windings and the core, d_{cf}, are composed of a casted thermally conductive polymeric material, CoolPoly-D5108,

Table 5.2: Steinmetz Coefficients of different magnetic materials

Magnetic Material	k	α	β	B_{sat} T	k_c	ρ_{core} $[\frac{kg}{m^3}]$
JFE10NEX900	7.25	2.23	1.91	1.6	0.95	7530
2605SA1	6.5	1.51	1.74	1.56	0.79	7180
3C85	19.86	1.3	2.55	0.45	1	4800
VITROPERM500F	0.48	1.8	2.3	1.2	0.75	7300
FINEMENT	1.19	1.53	1.52	1.23	0.73	7300

enabling a proper heat conduction to the heat sinks implemented on the core surfaces as well as providing enough isolation between the primary windings and the core [78]. The dielectric and thermal characteristics of some isolating materials, i.e, Dielectric strength, E_{ins}, dielectric constant, ε_r, loss tangent of the dielectric material, $tan\delta$, as well as thermal conductivity of the dielectric medium are presented in Table 5.3.

The third types of the fixed parameters are the inter layer and inter core distances as well as the outer insulation thickness of the wires used. The horizontal and vertical distances between the wires, d_{ins1}, d_{ins2}, d_{t1} and d_{t1} as Shown in Fig. 5.4. These distances are apart from the outer insulation thickness of the wires which assumed to be 0.5 mm for the current case study. Moreover, the frontal and lateral distances between the core stacks are considered as 1 mm.

5.3.3 Free Parameters

For the purpose of this study, 7 free parameters sweeping over a wide range are designated as the number of the magnetic core stacks, n_c, The frontal side of the core cross section, A, the number of layers and the number of turns per layer in primary portion, m_1 and N_{l1}, the effective thickness of the primary and secondary copper foils, d_{f1} and d_{f2} and finally the maximum allowed RMS value of the current density through a conductor, J_{max}. The selection of free parameters highly depends on the optimization goals and restrictions and considered core and winding topologies. For instance in case of litz conductors, one can consider the number of strands, strands diameter and the bundle dimensions as complementary free parameters.

All possible combinations of these free parameters will be applied to the optimization flowchart shown in Fig. 5.3, resulting in distinct transformer geometries corresponding to its set of free variables. Utilising the models explained in the previous chapters, the core, windings and dielectric losses are then be evaluated for each set of free parameters. The efficiency, power density and temperature rise of each transformer are then extracted and compared in order to obtain the optimum combination meeting the requirements.

Table 5.3: Electrical and Thermal Characteristics of Some Isolation Medium [35, 79, 80]

Dielectric Material	Thermal Conductivity $[\frac{W}{m.K}]$	Dielectric Strength $[\frac{kV}{mm}]$	$tan\delta$	Dielectric Constant ε_r
Air	0.03 (@70°C)	3	0	1.0005
Epoxy resin	0.25	15	0.021 (@ 100kHz)	3.6
CoolPoly-D5108 [78],	10	29	0.022 (@ 100Hz)	4.8
Mica	0.71	11-43	-	2.5-7
Transformer oil	0.12	10-15	2e-6 (@ 50MHz)	2.2-2.5
Paper	0.05	22-49	6e-5 (@ 1kHz)	2.3-5
RTV (Oxime)	1.8	8	-	-
NOMEX	-	27	5e-3(@ 60Hz)	2.5-4

5.3.4 Geometry Construction

Having the fixed and free parameters, the transformer geometry can be defined as follows. First, the required magnetic core cross section is defined, as explained in Chapter 4, as

$$A_c = \frac{V_{rms1}}{k_f k_c N_1 B_m f} \tag{5.8}$$

where V_{rms} is the rms value of the primary voltage, k_c is the filling factor of the core, N is the number of primary, $N_1 = m_1 N_{l1}$ and f is the fundamental frequency. The coefficient k_f is defined as

$$k_f = \frac{2\sqrt{2D - \frac{8}{3}R}}{D - R} \tag{5.9}$$

It should be noted that for the phase shift modulation in the DAB converter, the value of D is considered as 0.5 and R equals to zero. Moreover, in order to avoid the core saturation due to unwanted magnetic flux density fluctuation, the maximum induction level, B_m, is considered as 80 % of the saturation level of the selected magnetic core. Hence, considering the geometry structure shown in Fig. 5.4 and considering the number of core stacks, n_c, the lateral side of the magnetic core can be calculated as

$$B = \frac{A_c}{2n_c A} \tag{5.10}$$

The required clearances can be calculated by

$$d_{cf} = \lceil \frac{V_{LVDC}}{k_{saf} E_{ins}} \rceil \quad , \quad d_{cl1,2} = \lceil \frac{V_{MVDC}}{k_{saf} E_{ins}} \rceil \quad , \quad d_{iso-min} = \lceil \frac{V_{iso}}{k_{saf} E_{ins}} \rceil \tag{5.11}$$

where, a safety factor of 30 %, k_{saf}, is considered for dielectric strength of the isolating medium, resulting in $d_{cf} = 1mm$, $d_{cl1,2} = 4mm$ and $d_{iso-min} = 7mm$, which is the minimum allowed isolation distance between the primary and secondary windings in order to meet the isolation requirements of 60 kV. However, the actual value of d_{iso} will later be calculated with respect to the desired leakage inductance.

The copper foil heights of the primary and secondary windings are then be calculated as

$$h_{b1} = 2d_{ins-int1} + \frac{I_{T1}}{d_{f1} J_{max}} \quad , \quad h_{b2} = 2d_{ins-int2} + \frac{I_{T1}}{n.d_{f2} J_{max}} \tag{5.12}$$

where I_{T1} is the function of the applied phase shift, φ, considered to be the minimum allowed one ensuring the soft switching and yet having a reasonable amount of reactive power circulation. Assuming a maximum voltage deviation of 5 % and using (5.2), the minimum value of φ, ensuring ZVS turn on, is 0.075 rad or 4.3 degree.

$$I_{T1}\,(rms) = \frac{nV_{DC1} + V_{DC2}}{nL_{\sigma}} \sqrt{\frac{4t_1^2 t_{\varphi} + T_s t_1^2 - 4t_{\varphi}^2 t_1 - T_s t_1 t_{\varphi} + T_s t_{\varphi}^2}{3T_s}} \tag{5.13}$$

where t_1 and t_{φ} can be respectively calculated by

$$t_1 = \frac{\pi + 2\varphi d - \pi d}{4\pi f\,(1+d)} \tag{5.14}$$

$$t_{\varphi} = \frac{\varphi}{2\pi f} \tag{5.15}$$

As a result, the winding height, h_w, the core window height, H, and the primary windings build are respectively calculated as

$$h_w = (N_{l1} + 1)\, h_{b1} + N_{l1} d_{t1} \tag{5.16}$$

$$W_1 = m_1\,(d_{f1} + 2d_{ins-int1}) + (m_1 - 1)\, d_{ins1} \tag{5.17}$$

$$H = h_w + 2d_{cl} \tag{5.18}$$

Likewise, the number of turns and layers at the secondary windings are calculated by

$$N_{l2} = \left\lfloor \frac{h_w - h_{b2}}{h_{b2} + d_{t2}} \right\rfloor \tag{5.19}$$

$$m_2 = \left\lceil \frac{n.m_1.N_{l1}}{N_{l2}} \right\rceil \tag{5.20}$$

Accordingly, the secondary winding build is calculated from

$$W_2 = m_2 \left(d_{f2} + 2d_{ins-int2}\right) + \left(m_2 - 1\right) d_{ins2} \tag{5.21}$$

Hence, the mean length turn of the primary windings, MLT_1, which will be later used for the windings loss calculation is calculated from

$$MLT_1 = 2\left(2A + d_{c1} + 4d_{cf} + n_c B + \left(n_c - 1\right) d_{c2} + 2W_1\right) \tag{5.22}$$

5.3.4.1 Isolation Distance

In order to be able to calculate the rest of the geometrical dimensions, i.e, the core window width, the total length and width of the transformer box and consequently the total volume of the box, one firstly needs to calculate the required isolation distance, d_{iso}, fulfilling the minimum isolation requirements as well as providing the desired leakage inductance ensuring the ZVS operation of the DC-DC converter.

For this porpuse, the analytical expression in (3.15) derived in Chapter 3, accounting for the high frequency effect on leakage inductance value, is rearranged as

$$MLT_{iso}.m_1 d_{iso} = \frac{h_w}{\mu m_1 N_{l1}^2} L_{\sigma 1} - k_1 - k_2 MLT_2 - k_3 - k_4 MLT_2 \tag{5.23}$$

where k_1 to k_4 are defined as

$$k_1 = MLT_1 \frac{(m_1 - 1).(2m_1 - 1)}{6} d_{ins1} \tag{5.24}$$

$$k_2 = \frac{m_1(m_2 - 1)(2m_2 - 1)}{6m_2} d_{ins2} \tag{5.25}$$

$$\begin{aligned} k_3 = MLT_1 & \frac{sin(\frac{2\Delta_1}{\alpha\delta}) 4\alpha\delta^2(m_1^2 - 1) + 4d_{f1}(2m_1^2 + 1)}{24sin^2(\frac{2\Delta_1}{\alpha\delta}))} \\ + MLT_1 & \frac{-\alpha\delta^2 sin(\frac{4\Delta_1}{\alpha\delta})(2m_1^2 + 1) + 8d_{f1}(1 - m_1^2)cos(\frac{2\Delta_1}{\alpha\delta})}{24sin^2(\frac{2\Delta_1}{\alpha\delta}))} \end{aligned} \tag{5.26}$$

$$\begin{aligned} k_4 = & \frac{m_1}{m_2} \frac{sin(\frac{2\Delta_2}{\alpha\delta}) 4\alpha\delta^2(m_2^2-1) + 4d_{f2}(2m_2^2+1)}{24sin^2(\frac{2\Delta_2}{\alpha\delta}))} \\ & + \frac{m_1}{m_2} \frac{-\alpha\delta^2 sin(\frac{4\Delta_2}{\alpha\delta})(2m_2^2+1) + 8d_{f2}(1-m_2^2)cos(\frac{2\Delta_2}{\alpha\delta})}{24sin^2(\frac{2\Delta_2}{\alpha\delta}))} \end{aligned} \tag{5.27}$$

On the other hand, MLT_2 and MLT_{iso} in (5.23) are functions of d_{iso}. Therefore, solving (5.23) for d_{iso} gives

$$d_{iso} = \frac{-8k_8 - k_5 m_1 + \sqrt{(k_5 m_1 + 8k_8)^2 - 16m_1 (k_7 k_8 - k_6)}}{8m_1} \tag{5.28}$$

where k_5 to k_8 are defined as

$$\begin{aligned} MLT_{iso} &= 2\left(2A + d_{c1} + 4d_{cf} + 4W_1 + n_c B + (n_c - 1)\, d_{c2} + 2d_{iso}\right) \\ &= k_5 + 4d_{iso} \end{aligned} \tag{5.29}$$

$$k_6 = \frac{h_w}{\mu . m_1 . N_{l1}^2} L_{\sigma 1} - k_1 - k_3 \tag{5.30}$$

$$\begin{aligned} MLT_2 &= 2\left(2A + d_{c1} + 4d_{cf} + 4W_1 + n_c B + (n_c - 1)\, d_{c2} + 2W_2 + 4d_{iso}\right) \\ &= k_7 + 8d_{iso} \end{aligned} \tag{5.31}$$

and

$$k_8 = k_2 + k_4 \tag{5.32}$$

Thus, the expression in (5.28) gives the required isolation distance providing the desired leakage inductance as one of the design specification. The obtained value of d_{iso} must withstand the isolation voltage level, V_{iso} as well. Otherwise the design is not acceptable and the next calculation with a new set of the free parameters is initiated.

Having V_{iso} determined, one can uniquely draw the transformer sketch, shown in Fig. 5.4, with all the geometrical details. Therefore, it is possible to utilise the loss evaluation models, described and developed in the previous chapters, in order to evaluate the power losses of each individual transformer.

5.3.5 Core Loss Evaluation

In order to evaluate the core losses, the modified expression of IGSE suitable for non-sinusoidal waveforms in (4.35), derived in chapter 4, has been used as

$$P_{core} = \left(2D - \frac{4\alpha}{\alpha+1}R\right)\frac{2^{\beta}}{(D-R)^{\alpha}}k.k_i f^{\alpha} B_m^{\beta} V_c \rho \tag{5.33}$$

where D and R are equal to 0.5 and 0 respectively for the phase shift DAB converter, ρ is the core density and V_c, is the core volume corresponding to the investigated sets of free parameters as follows

$$V_c = 4n_c A.B\,(H + 2A) + 4n_c A.B.G \tag{5.34}$$

in which H is the window height previously calculated in (5.18) and G is the core window width calculated from

$$G = d_{cf} + W_1 + d_{iso} + W_2 + d_{cl} \tag{5.35}$$

5.3.6 Windings Loss Evaluation

To accurately evaluate the winding losses as an essential step in a high power density magnetic design, the pseudo-empirical method developed in Chapter 2 has been utilised. On the basis of the fact that copper has linear characteristics, the winding losses can be calculated using harmonic contents of the applied current, thus

$$P_{w1} = \sum_{h=1}^{n} R_{DC1}.RF_{1_h}.I_{1_h}^2 \quad , \quad P_{w2} = \sum_{h=1}^{n} R_{DC2}.RF_{2_h}.I_{2_h}^2 \tag{5.36}$$

where R_{DC1} and R_{DC2} are the DC resistance of the primary and secondary windings portion, RF_{1_h} and RF_{2_h} are respectively the AC resistance factor of the primary and secondary windings portion at the h^{th} harmonic, as well as I_{1_h} and I_{2_h}, which are respectively the RMS value of the primary and secondary currents through the transformer windings at h^{th} harmonic. DC resistance of the primary and secondary windings portion associated with the winding arrangement in Fig. 5.4 are calculated from

$$R_{DC1} = \frac{m_1 N_{l1} MLT_1}{\sigma d_{f1} h_{f1}} \quad , \quad R_{DC2} = \frac{m_2 N_{l2} MLT_2}{\sigma d_{f2} h_{f2}} \tag{5.37}$$

where σ is the conductivity of the conductors, here copper.

5.3.6.1 AC Resistance Factor

There is a uniquely determined transformer geometry associated with each set of free parameters, thus, in order to define the AC resistance factor, RF, five generic parameters, X_1 to X_5, are defined based on the primary and secondary windings dimensions and arrangements and are inserted in the following expressions as

$$\begin{aligned} RF_h &= f(X_1, X_2, X_3, X_4, X_5) \\ &= \sum_{i=0}^{5}\sum_{j\geq i}^{5}\sum_{m\geq j}^{5}\sum_{n\geq m}^{5}\sum_{s\geq n}^{5}\sum_{t\geq s}^{5} P_{ijmnst}.X_i.X_j.X_m.X_n.X_s.X_t \\ &+ \sum_{m=1}^{3}\sum_{i=0}^{5}\sum_{j\geq i}^{5} P_{ijm}.X_i.X_j.e^{-(X_1.X_2)^m} + \sum_{i=1}^{5} P_i \frac{X_4^2}{(X_1.X_2)^i} \end{aligned} \tag{5.38}$$

whereas for the single-layer configuration ($X_4 = 1$), the AC resistance factor can be calculated from

$$\begin{aligned} RF_h &= f(X_1, X_2, X_3, X_4) \\ &= \sum_{i=0}^{3}\sum_{j\geq i}^{3}\sum_{m\geq j}^{3}\sum_{n\geq m}^{3}\sum_{s\geq n}^{3} P_{ijmns}.X_i.X_j.X_m.X_n.X_s \end{aligned} \tag{5.39}$$

5.3.6.2 Harmonic Contents

As shown in Fig. 5.2 (a), the transformer voltages and currents are not sinusoidal. Under this scope, evaluating the harmonic contents is the key particularly for winding loss calculation. Assuming arbitrary duty cycles, the voltages applied on both sides of the transformer, referred to the primary side, can be written as

$$V_{T1} = \sum_{h=1}^{n} \frac{4V_{DC1}}{\pi h} \left|sin(\pi h D_1)\right| sin(h\omega t + \tan^{-1}(\cot(\pi h D_1)) + h\varphi) \tag{5.40}$$

$$V'_{T2} = \sum_{h=1}^{n} \frac{4dV_{DC1}}{\pi h} \left|sin(\pi h D_2)\right| sin(h\omega t + \tan^{-1}(\cot(\pi h D_2))) \tag{5.41}$$

where φ is the phase shift between two bridges. Hence, the peak value of the voltage over the leakage inductance are calculated from

$$\Delta V_{Lp_h} = \frac{4V_{DC1}}{\pi h}\sqrt{sin^2(\pi h D_1) + d^2 sin^2(\pi h D_2) - 2d\left|sin(\pi h D_1) sin(\pi h D_2)\right| \cos(\Delta\phi_h)} \tag{5.42}$$

where $\Delta\phi$ can be calculated from

$$\Delta\phi_h = \tan^{-1}(\cot(\pi h D_1)) - \tan^{-1}(\cot(\pi h D_2)) + h\varphi \tag{5.43}$$

Therefore, the RMS value of the h^{th} harmonic of the current at the primary and secondary windings to be used in (5.36) are respectively

$$I_{1_h} = \frac{\Delta V_{Lp_h}}{2\pi f.h.L_\sigma} \quad , \quad I_{2_h} = \frac{\Delta V_{Lp_h}}{2\pi f.h.n.L_\sigma} \tag{5.44}$$

5.3.7 Dielectric Loss Evaluation

In a low frequency applications, dielectric losses are often negligible, however when operating in higher frequencies, this type of loss are also important to be considered particularly in high power density applications where the design already pushed to its limits. The dielectric losses are calculated from

$$P_{ins} = \Delta V_{ins}^2 . 2\pi f . C_{ins} . tan(\delta) \tag{5.45}$$

in which $tan(\delta)$ is the dissipation factor of the dielectric material, already presented in Table. 5.3, C_{ins} and ΔV_{ins} are respectively the capacitance of the dielectric medium and the voltage over it. It should be pointed out that for simplicity, a uniform distribution of magnetic field is considered within the isolation distance d_{iso}, coil former distance d_{cf}, as well as clearing distances d_{cl}, which are considered in the current design approach.

5.3.8 Maximum Power Dissipation Capability

The thermal aspects of a magnetic design is one of the most crucial issues since in principle it is the main design limitation, specifying the geometrical boundaries in which the magnetic component can continuously operates without exceeding the critical temperature, as one of the design criteria. Under this scope, a proper thermal management scheme is a key to dissipate the power losses and consequently to achieve higher power densities.

The combination of two thermal management methods, shown in Fig. 5.6, are implemented in the current design approach. First of all, as in planar transformers, heat sinks are considered to be placed on the core surfaces in order to increase the effective surface area resulting in thermal resistance reduction and consequently higher power dissipation capability of the design. The main drawback of this method, besides increasing the total volume of the transformer box, is that due to the poor thermal contact of the core and the primary windings, the heat around the middle limbs, usually the hottest spot of the transformer, can not easily be conducted to the heat sink. For this reason, a complementary thermal management method has been incorporated placing a thermally conductive material between the primary windings

and the core in order to directly conduct the heat to the top and bottom part of the transformer where heat sinks are assembled. As a result, with a negligible increase in transformer total volume, heat can be extracted from the hot spots deep inside the transformer. Copper or aluminium straps are suitable candidates for this purpose due to their relatively high thermal conductivity. However, in the current design methodology, a thermally conductive, electrically dielectric, polymeric material, which simultaneously can be considered both as the heat removal medium and a dielectric bobbin or coil former for the transformer, is used. In addition, using the polymeric material, the possibility of eddy current losses in copper or aluminium due to an unwanted air gap in the core, is considerably reduced.

In principle, defining the convection coefficients is one of the biggest uncertain parts of any magnetic design, due to many practical factors affecting the heat transfer process. Therefore, it may be hard to justify the use of very elaborated methods for specifying this coefficients [35].

Having the outer surface of the magnetic component determined, the maximum power dissipation capability of each transformer corresponding to each sets of free parameters can be calculated from

$$\begin{aligned} P_{d-max} &= P_{conv} + P_{rad} \\ &= h_{conv} A_{conv} \left(T_s - T_a\right) + h_{rad} A_{rad} \left(T_s - T_a\right) \end{aligned} \tag{5.46}$$

where P_{conv} and P_{rad} are the heat transfer rates by convection and radiation heat transfer mechanisms, respectively. A_{conv} and A_{rad} are the convective and radiating area, respectively, and T_s and T_a are the temperature of the surface and ambient temperature, in the same order. h_{rad} is the radiation heat transfer coefficient calculated by

$$h_{rad} = \frac{\varepsilon\sigma \left(T_s^4 - T_a^4\right)}{T_s - T_a} \tag{5.47}$$

where ε is the emissivity of the radiating surface and ε is the Stefan-Boltzmann constant, $\sigma = 5.67 \times 10^{-8} \frac{W}{m^2.K^4}$.

The convection heat transfer coefficient, h_{conv}, is probably the most uncertain coefficient in any magnetic design requiring a reliable thermal evaluation since it depends on physical dimensions and orientation of the object, type of the fluid, density, velocity and several other parameters which are not often possible to be reliably determined. One of the accurate presentations of the convection coefficient is reported in [35] defining it by the Nusselt number, Nu, as follows

$$h_{conv} = Nu \frac{k}{L} \tag{5.48}$$

where k is the thermal conductivity and L is the characteristic length of the objects

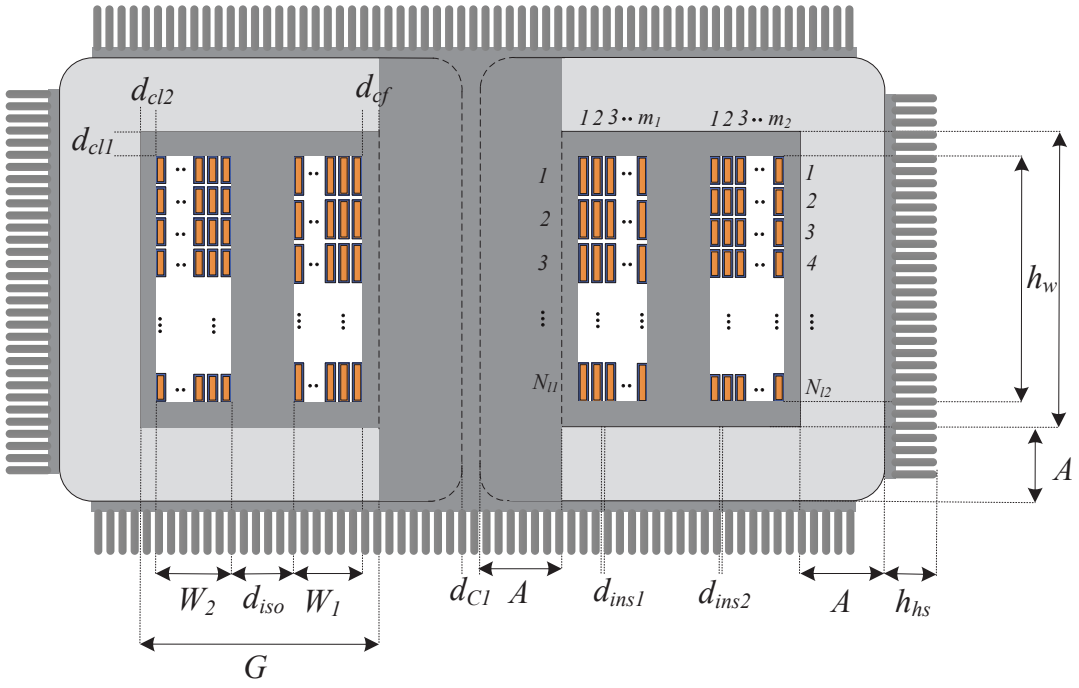

Figure 5.6: Frontal view of the proposed transformer geometry illustrating the thermally conductive polymer and heat sinks. .

defined as the total distance passed by the fluid cooling the magnetic component as follows

$$L = n_c B + (n_c - 1)d_{c2} + H + 2\sqrt{A^2 + G^2} \tag{5.49}$$

There are several presentations of Nusselt number, however the one reported in [35], in addition to its high accuracy, is valid for a wide range of Rayleigh number as folows

$$Nu = 0.68 + \frac{0.67Ra^{1/4}}{\left(1 + (0.492/Pr)^{9/16}\right)^{4/9}} \qquad for \qquad Ra < 10^9 \tag{5.50}$$

where Ra, Gr and pr are rayleigh number, Grashof number and Prandtl number, respectively calculated from

$$Ra = Gr.Pr \tag{5.51}$$

$$Gr = \frac{g\left(\frac{2}{T_s + T_a}\right)(T_s - T_a)L^3}{\nu^2} \tag{5.52}$$

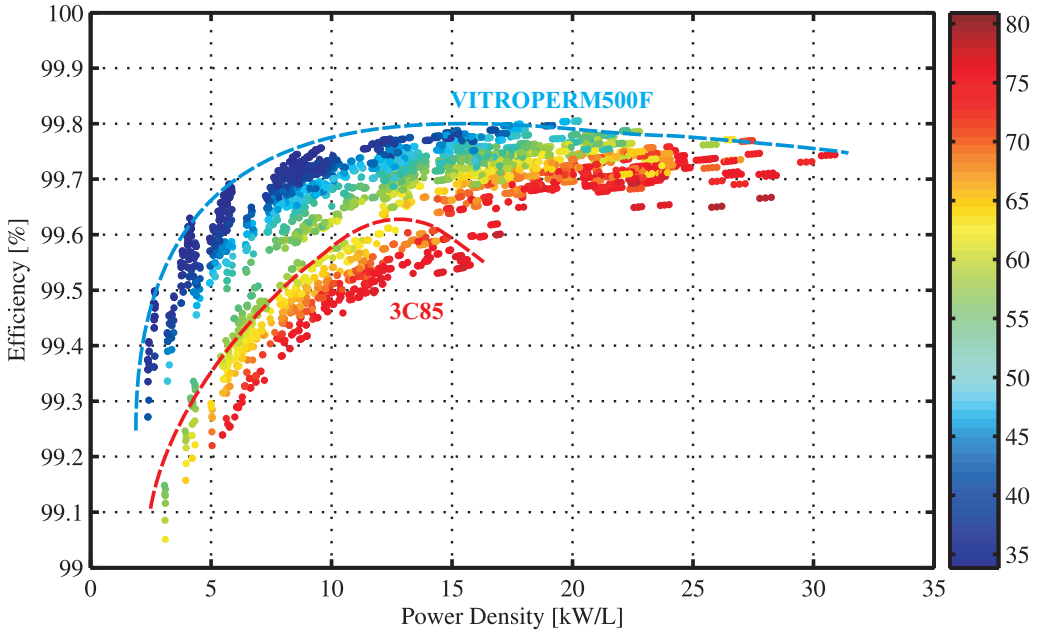

Figure 5.7: Efficiency versus Power density of feasible cases study transformers according to the proposed design methodology with two different core materials.

$$Pr = c_p \frac{\mu}{k} \tag{5.53}$$

where g is the gravity, c_p is the specific heat value, ν and μ are the kinematic and dynamic viscosities, respectively. The values of these parameters can be found in heat transfer textbooks and handbooks for different materials at different temperatures [35, 81]. As a result, the convection heat transfer coefficient can be calculated from

$$h_{conv} = \left(0.68 + \frac{0.67 \left(g \left(\frac{2}{T_s + T_a} \right) (T_s - T_a) L^3 . Pr / \nu^2 \right)^{1/4}}{\left(1 + (0.492/Pr)^{9/16} \right)^{4/9}} \right) \frac{k}{L} \tag{5.54}$$

5.3.9 Optimization Results

The proposed design methodology explained in this chapter has been applied on the transformer specification shown in table. 5.1. For this purpose, each free parameter is swept over a wide range of inputs resulting in more than 600000 combinations of free parameters. These sets of free parameters are then applied to the design flowchart shown in Fig. 5.3 to find the optimum set. The optimization outcome showing the

Table 5.4: Optimal transformer characteristics

Geometrical		Electrical/Magnetic	
Total length	288 mm	Winding losses	1639 W
Total width	335 mm	Core losses	979 W
Total height	542 mm	Dielectric losses	19.5 W
Volume	44.78 Liter	Total losses	2637.5 W
N_1	12	Efficiency	99.74%
N_2	24	Power density	22.33 kW/L
A	40 mm	B_{max}	0.96 T
Isolation distance, d_{iso}	48 mm	J_{max}	3 A/mm2
d_{f1}	1.25 mm	Temperature rise	$59.9°C$
d_{f2}	0.5 mm	h_{conv}	3.74
Number of core stacks	3	h_{rad}	6.93

efficiencies and power densities of the transformer designs corresponding to accepted sets of free parameters illustrated in Fig. 5.7. Therefore, each colored dot represents a unique design which met all the design requirements and its color indicates the corresponding temperature rise of that particular transformer.

The design procedure is performed using two different core materials, VITROPERM500F and 3C85, both suitable for high frequency applications. As can be seen in Fig. 5.7, VITROPERM500F demonstrates higher efficiencies for the same power density which can be explained by the lower specific losses of VITROPERM500F compared to 3C85 as already presented in Fig. 4.1. Furthermore, Fig. 5.7 shows that VITROPERM500F can achieve substantially higher power densities of about 25 kW/L with maximum $60°C$ temperature increase compared to the one of about 10 kW/L for 3C85. This also can be explained by the relatively higher saturation level of VITROPERM500F compared to the one of 3C85.

It is worth to mention that the high isolation requirements of the case study transformer, 60 kV isolation for a 3/6 kV transformer, together with the desired leakage inductances as the design inputs, play an important role in reducing the power density of the final optimum design. Geometrical and electrical characteristics of the optimized 1 MW transformer with the specification presented in table. 5.1 are summerized in table. 5.4.

As can be seen in table. 5.4, using the design methodology proposed in this chapter, a 1 MW, 3/6 kV transformer operating at 5 kHz can be as compact as 45 liters while the efficiency is about 99.7% and the maximum temperature rise considering natural cooling is $60°C$.

Fig. 5.8 demonstrates a comparative analysis of the optimum transformer volume

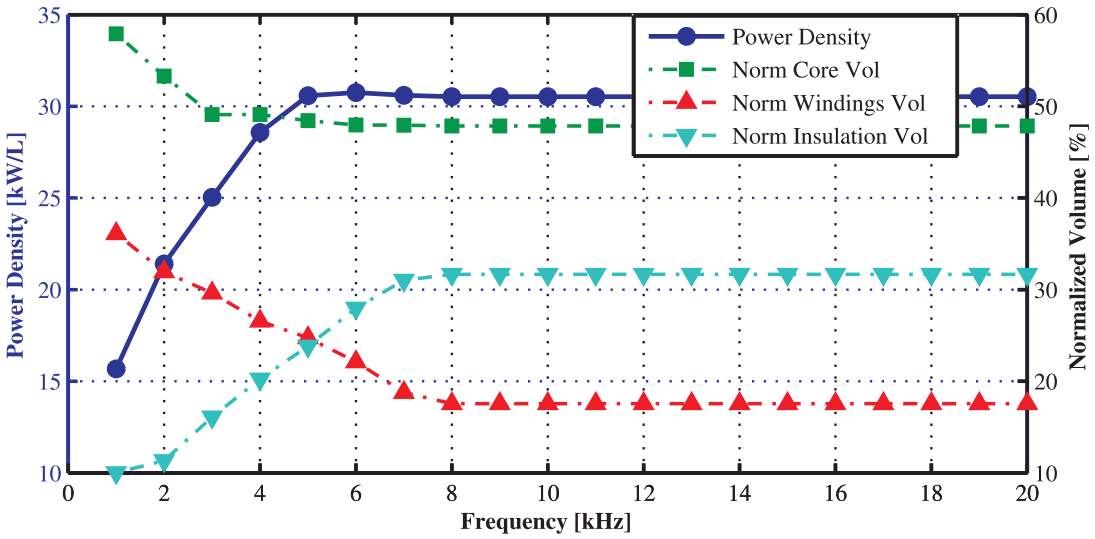

Figure 5.8: Power density, Normalized volume of the optimized transformers with different operating frequencies.

at different operating frequencies from 1 to 20 kHz. All the design requirements comprising the output power, voltage levels, isolation requirements and the maximum temperature increase are kept constant whereas the frequency and consequently the required leakage inductance change. Each operating frequency requires a complete optimization process, investigating hundred of thousands of different geometries. The optimum design at each frequency is then extracted and compared in Fig. 5.8, presenting the power density, the volume percentage of the core, windings and insulation at optimum transformers corresponding to each frequency.

The results indicate that there is an optimum frequency in which the transformer can reach to its minimum dimensions and any further increase in frequency does not have a considerable effect on transformer volume reduction, whereas the DAB converter suffers form the enhanced switching losses at those unnecessary high frequencies. This attribute is clearly demonstrated in Fig. 5.8 when the power density of the optimum design does not significantly increase after 5 kHz. It is interesting to notice that up to 8 kHz, the portion of the optimum transformers made of magnetic core and windings continuously decrease, while the share of isolating material increases until it reaches to as high as 32% of the total volume of the optimum design at frequencies above 7 kHz, indicating the fact that there is a critical frequency above which the transformer does not benefit from volume reduction any further. This critical frequency is lower at high voltage applications where relatively high isolation requirement is needed.

5.4 Conclusions

The objective of this chapter was to bring together all the models developed and adopted in the previous chapters in order to propose a design and optimization methodology of high power density transformer, particularly the ones requiring high isolation levels and tuned leakage inductances.

The proposed design methodology was applied on a 1 MW case study transformer and the pareto fronts of the power density versus efficiency considering the maximum temperature increase for two different magnetic core materials were studied. The results indicate that such a transformer can achieve a power density of about 22 kW/L and the efficiencies as high as 99.74% which is substantially smaller than the line frequency transformers with similar range of power and voltages.

With respect to the isolation requirements, the desired leakage inductance and the magnetic material used, a critical operating frequency can be found above which the transformer does not benefit from volume reduction anymore.

Chapter 6

Conclusions and Future Work

6.1 Conclusions

The main objective of the thesis was to propose a design and optimization methodology of a high power high frequency transformer accounting for the tuned leakage inductance of the transformer, as well as high isolation requirements, particularly in DC offshore applications where a converter module should withstand the MVDC or HVDC link voltage. To achieve this goal, several models were proposed and developed in order to accurately characterize such a transformer.

In order to precisely calculate the AC resistance factor of high power-density magnetic components, a so called pseudo-empirical expression has been derived from a rigourous regression algorithm based on an extensive 2D finite element simulation scenario, resulting in an accurate analytical expression with an average unsigned deviation of 0.51% and the extreme deviations of not higher than 9%. This high accuracy together with its wide range of applicability, taking into account any number of layers, a wide range of penetration ratios, porosity factors, and position of the windings in the transformer window, make the pseudo-empirical expression a useful tool to easily be implemented within optimization loops proposed in the final chapter. Moreover, using the energy method, an analytical expression to precisely calculate the leakage inductance of high power density magnetic components was proposed. Apart from the windings and leakage inductance expression, using the proposed modification of the Steinmetz equation in literatures, such as the MSE, IGSE and WcSE, some general expressions were derived and presented for a rectangular waveform with its associated duty cycle and rise time. In each of these expressions, a correction factor was introduced to correlate the Steinmetz expression to these waveforms.

Finally, the proposed design methodology, utilising the aforementioned developed expressions, was applied on a 1 MW case study transformer and the pareto fronts of the power density versus efficiency considering the maximum temperature

increase for two different magnetic core materials, were studied. The results indicate that such a transformer can achieve a power density of about 22 kW/L, substantially smaller than the line frequency transformers with similar range of power and voltages, and an efficiency as high as 99.74% . With respect to the isolation requirements, the desired leakage inductance and the magnetic material used, a critical operating frequency can be found above which the transformer does not benefit from volume reduction anymore.

6.2 Future Work

In principle, a complete evaluation of a DC-DC transformer design is a complex task in which both the switching and magnetic stage should be optimized at the same time. In this work, the converter requirements such as the frequency and the required leakage inductance are considered fixed. However, considering the current method as a basis, optimization from a higher level including switching and conduction losses of the converter will be the next step of this PhD study. However, prior to the system level study, the proposed design and optimization methodology firstly needs to be extended in order to consider different types of windings such as litz wire which seems to be promising solution for this application.

Further developments can be done in the theoretical side by implementing a more detailed thermal analysis accounting for the temperature at different locations inside the transformer as well as different thermal managements such as forced cooling, oil immersed transformer and other heat dissipation solutions.

Investigation of using different switching frequencies, different converter topologies and modulations can be performed based on the extended version of the proposed design approach. Finally, experimental validation of the proposed method is planned to be done by manufacturing prototype transformers based on VITROPERM500F and N87 magnetic cores.

Bibliography

[1] T. Kjellqvist, S. Norrga, and S. Ostlund, "Design considerations for a medium frequency transformer in a line side power conversion system," in *Power Electronics Specialists Conference, 2004. PESC 04. 2004 IEEE 35th Annual*, vol. 1, june 2004, pp. 704 – 710 Vol.1.

[2] G. Ortiz, J. Biela, D. Bortis, and J. Kolar, "1 megawatt, 20 khz, isolated, bidirectional 12kv to 1.2kv dc-dc converter for renewable energy applications," in *Power Electronics Conference (IPEC), 2010 International*, june 2010, pp. 3212 –3219.

[3] D. Dujic, F. Kieferndorf, F. Canales, and U. Drofenik, "Power electronic traction transformer technology," in *Power Electronics and Motion Control Conference (IPEMC), 2012 7th International*, vol. 1, june 2012, pp. 636 –642.

[4] A. Bahmani, T. Thiringer, and H. Jimenez, "An accurate pseudo-empirical model of winding loss calculation for hf foil and round conductors in switchmode magnetics," *Power Electronics, IEEE Transactions on*, vol. PP, no. 99, pp. 1–1, 2013.

[5] R. T. Naayagi, A. Forsyth, and R. Shuttleworth, "High-power bidirectional dc-dc converter for aerospace applications," *Power Electronics, IEEE Transactions on*, vol. 27, no. 11, pp. 4366–4379, 2012.

[6] S. Meier, T. Kjellqvist, S. Norrga, and H.-P. Nee, "Design considerations for medium-frequency power transformers in offshore wind farms," in *Power Electronics and Applications, 2009. EPE '09. 13th European Conference on*, Sept 2009, pp. 1–12.

[7] L. Heinemann, "An actively cooled high power, high frequency transformer with high insulation capability," in *Applied Power Electronics Conference and Exposition, 2002. APEC 2002. Seventeenth Annual IEEE*, vol. 1, 2002, pp. 352–357 vol.1.

[8] M. Steiner and H. Reinold, "Medium frequency topology in railway applications," in *Power Electronics and Applications, 2007 European Conference on*, Sept 2007, pp. 1–10.

[9] W. Colonel and K. T. McLyman, *Transformer and Inductor Design Handbook, Fourth Edition.* CRC Press, 2011.

[10] S. Farhangi and A. Akmal, "A simple and efficient optimization routine for design of high frequency power transformers," in *Proceeding of 9th EPE Conference*, Sep 1999.

[11] R. Petkov, "Optimum design of a high-power, high-frequency transformer," *Power Electronics, IEEE Transactions on*, vol. 11, no. 1, pp. 33–42, Jan 1996.

[12] W. Hurley, W. Wolfle, and J. Breslin, "Optimized transformer design: inclusive of high-frequency effects," *Power Electronics, IEEE Transactions on*, vol. 13, no. 4, pp. 651–659, Jul 1998.

[13] I. Villar, L. Mir, I. Etxeberria-Otadui, J. Colmenero, X. Agirre, and T. Nieva, "Optimal design and experimental validation of a medium-frequency 400kva power transformer for railway traction applications," in *Energy Conversion Congress and Exposition (ECCE), 2012 IEEE*, Sept 2012, pp. 684–690.

[14] G. Ortiz, M. Leibl, J. Kolar, and O. Apeldoorn, "Medium frequency transformers for solid-state-transformer applications ; design and experimental verification," in *Power Electronics and Drive Systems (PEDS), 2013 IEEE 10th International Conference on*, April 2013, pp. 1285–1290.

[15] E. Agheb, M. A. Bahmani, H. K. Hoidalen, and T. Thiringer, "Core loss behavior in high frequency high power transformers—ii: Arbitrary excitation," *Journal of Renewable and Sustainable Energy*, vol. 4, no. 3, p. 033113, 2012.

[16] G. Ortiz, J. Biela, and J. Kolar, "Optimized design of medium frequency transformers with high isolation requirements," in *IECON 2010 - 36th Annual Conference on IEEE Industrial Electronics Society*, nov. 2010, pp. 631 –638.

[17] E. Bennett and S. C. Larson, "Effective resistance to alternating currents of multilayer windings," *American Institute of Electrical Engineers, Transactions of the*, vol. 59, no. 12, pp. 1010 –1017, dec. 1940.

[18] P. Dowell, "Effects of eddy currents in transformer windings," *Electrical Engineers, Proceedings of the Institution of*, vol. 113, no. 8, pp. 1387 –1394, august 1966.

[19] A. Reatti and M. Kazimierczuk, "Comparison of various methods for calculating the ac resistance of inductors," *Magnetics, IEEE Transactions on*, vol. 38, no. 3, pp. 1512 –1518, may 2002.

[20] F. Robert, P. Mathys, and J.-P. Schauwers, "Ohmic losses calculation in smps transformers: numerical study of dowell's approach accuracy," *Magnetics, IEEE Transactions on*, vol. 34, no. 4, pp. 1255 –1257, jul 1998.

[21] F. Robert, P. Mathys, B. Velaerts, and J.-P. Schauwers, "Two-dimensional analysis of the edge effect field and losses in high-frequency transformer foils," *Magnetics, IEEE Transactions on*, vol. 41, no. 8, pp. 2377 – 2383, aug. 2005.

[22] A. Lotfi and F. Lee, "Two dimensional field solutions for high frequency transformer windings," in *Power Electronics Specialists Conference, 1993. PESC '93 Record., 24th Annual IEEE*, jun 1993, pp. 1098 –1104.

[23] A. Loth and F. Lee, "Two-dimensional skin effect in power foils for high-frequency applications," *Magnetics, IEEE Transactions on*, vol. 31, no. 2, pp. 1003 –1006, march 1995.

[24] G. Dimitrakakis and E. Tatakis, "High-frequency copper losses in magnetic components with layered windings," *Magnetics, IEEE Transactions on*, vol. 45, no. 8, pp. 3187 –3199, aug. 2009.

[25] U. Kirchenberger, M. Marx, and D. Schroder, "A contribution to the design optimization of resonant inductors for high power resonant dc-dc converters," in *Industry Applications Society Annual Meeting, 1992., Conference Record of the 1992 IEEE*, oct 1992, pp. 994 –1001 vol.1.

[26] J. Ferreira, "Appropriate modelling of conductive losses in the design of magnetic components," in *Power Electronics Specialists Conference, 1990. PESC '90 Record., 21st Annual IEEE*, 0-0 1990, pp. 780 –785.

[27] ——, "Aring;nalytical computation of ac resistance of round and rectangular litz wire windings," *Electric Power Applications, IEE Proceedings B*, vol. 139, no. 1, pp. 21 –25, jan 1992.

[28] C. Sullivan, "Computationally efficient winding loss calculation with multiple windings, arbitrary waveforms, and two-dimensional or three-dimensional field geometry," *Power Electronics, IEEE Transactions on*, vol. 16, no. 1, pp. 142 –150, jan 2001.

[29] W. Hurley, E. Gath, and J. Breslin, "Optimizing the ac resistance of multilayer transformer windings with arbitrary current waveforms," *Power Electronics, IEEE Transactions on*, vol. 15, no. 2, pp. 369 –376, mar 2000.

[30] R. Wojda and M. Kazimierczuk, "Analytical optimization of solid-round-wire windings," *Industrial Electronics, IEEE Transactions on*, vol. 60, no. 3, pp. 1033 –1041, march 2013.

[31] F. Robert, P. Mathys, and J.-P. Schauwers, "A closed-form formula for 2d ohmic losses calculation in smps transformer foils," in *Applied Power Electronics Conference and Exposition, 1999. APEC '99. Fourteenth Annual*, vol. 1, mar 1999, pp. 199 –205 vol.1.

[32] *Maxwell 3D user's manual*, Ansoft Corporation, February 2009, REV4.0, Pittsburgh, USA, 2009.

[33] R. Prieto, J. Oliver, and J. Cobos, "Study of non-axisymmetric magnetic components by means of 2d fea solvers," in *Power Electronics Specialists Conference, 2005. PESC '05. IEEE 36th*, june 2005, pp. 1074 –1079.

[34] A. Hoke and C. Sullivan, "An improved two-dimensional numerical modeling method for e-core transformers," in *Applied Power Electronics Conference and Exposition, 2002. APEC 2002. Seventeenth Annual IEEE*, vol. 1, 2002, pp. 151 –157 vol.1.

[35] A. Bossche and V. Valchev, *Inductors and Transformers for Power Electronics, Taylor and Francis Group.* CRC Press, 2005.

[36] J.-P. Vandelac and P. Ziogas, "A novel approach for minimizing high-frequency transformer copper losses," *Power Electronics, IEEE Transactions on*, vol. 3, no. 3, pp. 266 –277, july 1988.

[37] C. Hawkes, T. Wilson, and R. Wong, "Magnetic-field-intensity and current-density distributions in transformer windings," in *Power Electronics Specialists Conference, 1989. PESC '89 Record., 20th Annual IEEE*, jun 1989, pp. 1021 –1030 vol.2.

[38] M. Bahmani and T. Thiringer, "A high accuracy regressive-derived winding loss calculation model for high frequency applications," in *Power Electronics and Drive Systems (PEDS), 2013 IEEE 10th International Conference on*, April 2013, pp. 358–363.

[39] P. Evans and K. Al-Shara, "Losses in foil-wound secondaries in high-frequency transformers," *Magnetics, IEEE Transactions on*, vol. 25, no. 4, pp. 3125 –3132, jul 1989.

[40] M. Heldwein, H. Ertl, J. Biela, and J. Kolar, "Implementation of a transformerless common mode active filter for off-line converter systems," in *Applied Power*

Electronics Conference and Exposition, 2006. APEC '06. Twenty-First Annual IEEE, march 2006, p. 7 pp.

[41] W. F. Flanagan, *Handbook of Transformer Design and Applications, Second Edition.* McGraw-Hill, 1992.

[42] M. Bartoli, N. Noferi, A. Reatti, and M. K. Kazimerczuk, "Modelling winding losses in high-frequency power inductors," *Journal of Circuits, Systems and Computers*, vol. 05, no. 04, pp. 607–626, 1995.

[43] M. Albach, "Two-dimensional calculation of winding losses in transformers," in *Power Electronics Specialists Conference, 2000. PESC 00. 2000 IEEE 31st Annual*, vol. 3, 2000, pp. 1639 –1644 vol.3.

[44] R. De Doncker, D. Divan, and M. Kheraluwala, "A three-phase soft-switched high-power-density dc/dc converter for high-power applications," *Industry Applications, IEEE Transactions on*, vol. 27, no. 1, pp. 63–73, 1991.

[45] W. Roshen, "A practical, accurate and very general core loss model for nonsinusoidal waveforms," *Power Electronics, IEEE Transactions on*, vol. 22, no. 1, pp. 30–40, Jan 2007.

[46] R. Liu, C. Mi, and D. Gao, "Modeling of eddy-current loss of electrical machines and transformers operated by pulsewidth-modulated inverters," *Magnetics, IEEE Transactions on*, vol. 44, no. 8, pp. 2021–2028, Aug 2008.

[47] I. Villar, U. Viscarret, I. Etxeberria-Otadui, and A. Rufer, "Global loss evaluation methods for nonsinusoidally fed medium-frequency power transformers," *Industrial Electronics, IEEE Transactions on*, vol. 56, no. 10, pp. 4132–4140, Oct 2009.

[48] Y. Nie, Q. Hu, and Y. Huang, "The measurement and prediction of iron loss under nonsinusoidal voltage waveform with arbitrary frequency," in *Electrical Machines and Systems, 2008. ICEMS 2008. International Conference on*, Oct 2008, pp. 232–236.

[49] G. Dimitrakakis and E. Tatakis, "High-frequency copper losses in magnetic components with layered windings," *Magnetics, IEEE Transactions on*, vol. 45, no. 8, pp. 3187–3199, Aug 2009.

[50] W. Shen, F. Wang, D. Boroyevich, and C. Tipton, "Loss characterization and calculation of nanocrystalline cores for high-frequency magnetics applications," *Power Electronics, IEEE Transactions on*, vol. 23, no. 1, pp. 475–484, Jan 2008.

[51] M. Rylko, K. Hartnett, J. Hayes, and M. Egan, "Magnetic material selection for high power high frequency inductors in dc-dc converters," in *Applied Power Electronics Conference and Exposition, 2009. APEC 2009. Twenty-Fourth Annual IEEE*, Feb 2009, pp. 2043–2049.

[52] B. Lyons, J. Hayes, and M. Egan, "Magnetic material comparisons for high-current inductors in low-medium frequency dc-dc converters," in *Applied Power Electronics Conference, APEC 2007 - Twenty Second Annual IEEE*, Feb 2007, pp. 71–77.

[53] Y. Han, G. Cheung, A. Li, C. Sullivan, and D. Perreault, "Evaluation of magnetic materials for very high frequency power applications," in *Power Electronics Specialists Conference, 2008. PESC 2008. IEEE*, June 2008, pp. 4270–4276.

[54] M. A. Bahmani, E. Agheb, T. Thiringer, H. K. Hidalen, and Y. Serdyuk, "Core loss behavior in high frequency high power transformers—i: Effect of core topology," *Journal of Renewable and Sustainable Energy*, vol. 4, no. 3, p. 033112, 2012.

[55] M. Wasekura, C.-M. Wang, Y. Maeda, and R. Lorenz, "A transient core loss calculation algorithm for soft magnetic composite material," in *Energy Conversion Congress and Exposition (ECCE), 2013 IEEE*, 2013, pp. 3719–3725.

[56] [Online]. Available: http://www.jfe-steel.co.jp/

[57] [Online]. Available: http://www.metglas.com/

[58] [Online]. Available: http://www.ferroxcube.com/

[59] [Online]. Available: http://www.mag-inc.com/

[60] [Online]. Available: http://www.vacuumschmelze.com/

[61] [Online]. Available: http://www.hitachimetals.com/

[62] J. Pedro, B. A., and S. N., *Electromagnetic modeling by finite element methods*. Markel Dekker, 2003.

[63] D. Jiles and D. Atherton, "Theory of ferromagnetic hysteresis," *Journal of Magnetism and Magnetic Materials*, vol. 61, no. 12, pp. 48 – 60, 1986. [Online]. Available: http://www.sciencedirect.com/science/article/pii/0304885386900661

[64] B. Lederer, H. Igarashi, A. Kost, and T. Honma, "On the parameter identification and application of the jiles-atherton hysteresis model for numerical modelling of measured characteristics," *Magnetics, IEEE Transactions on*, vol. 35, no. 3, pp. 1211–1214, May 1999.

[65] G. Bertotti, *Hysteresis in magnetism.* Academic press, San diego, 1998.

[66] ——, "General properties of power losses in soft ferromagnetic materials," *Magnetics, IEEE Transactions on*, vol. 24, no. 1, pp. 621–630, Jan 1988.

[67] D. Ribbenfjard, *Electromagnetic transformer modelling including the ferromagnetic core*, 2010, Stockholm.

[68] D. Lin, P. Zhou, W. N. Fu, Z. Badics, and Z. Cendes, "A dynamic core loss model for soft ferromagnetic and power ferrite materials in transient finite element analysis," *Magnetics, IEEE Transactions on*, vol. 40, no. 2, pp. 1318–1321, March 2004.

[69] M. Mobarrez, M. Fazlali, M. A. Bahmani, and T. Thiringer, "Performance and loss evaluation of a hard and soft switched 2.4 mw, 4 kv to 6 kv isolated dc-dc converter for a wind energy application," in *IECON 2012 - 38th Annual Conference on IEEE Industrial Electronics Society*, Oct 2012, pp. 5086–5091.

[70] C. Steinmetz, "On the law of hysteresis," *American Institue of Electrical Engineers Transactions*, vol. 9, pp. 3–64, 1982.

[71] R. Severns, "Hf-core lossesfor non-sinusoidal waveforms," in *Proceedings of HFPC*, 1991, pp. 140–148.

[72] J. Reinert, A. Brockmeyer, and R. W. De Doncker, "Calculation of losses in ferro- and ferrimagnetic materials based on the modified steinmetz equation," in *Industry Applications Conference, 1999. Thirty-Fourth IAS Annual Meeting. Conference Record of the 1999 IEEE*, vol. 3, 1999, pp. 2087–2092 vol.3.

[73] J. Li, T. Abdallah, and C. Sullivan, "Improved calculation of core loss with nonsinusoidal waveforms," in *Industry Applications Conference, 2001. Thirty-Sixth IAS Annual Meeting. Conference Record of the 2001 IEEE*, vol. 4, Sept 2001, pp. 2203–2210 vol.4.

[74] K. Venkatachalam, C. Sullivan, T. Abdallah, and H. Tacca, "Accurate prediction of ferrite core loss with nonsinusoidal waveforms using only steinmetz parameters," in *Computers in Power Electronics, 2002. Proceedings. 2002 IEEE Workshop on*, June 2002, pp. 36–41.

[75] A. Van den Bossche, V. Valchev, and G. Georgiev, "Measurement and loss model of ferrites with non-sinusoidal waveforms," in *Power Electronics Specialists Conference, 2004. PESC 04. 2004 IEEE 35th Annual*, vol. 6, June 2004, pp. 4814–4818 Vol.6.

[76] W. Shen, "Design of high-density transformerfor high frequency high power converters," Ph.D. dissertation, Virginia Polytechnic Institute.

[77] N. Mohan, T. Undeland, and W. Robbins, *Power electronics Converter, Applications and Design, Second Edition*. John Wiley and Sons Inc, 1995.

[78] [Online]. Available: http://www.coolpolymers.com/

[79] [Online]. Available: http://www.kayelaby.npl.co.uk/general_physics/2_6/2_6_5.html

[80] [Online]. Available: http://www.rfcafe.com/references/electrical/dielectric-constants-strengths.htm

[81] J. Holman, *Heat Transfer, 8th Edition*. McGraw-Hill, New York, 1997.